NTNU
Norwegian University of
Science and Technology

Computation of Nonlinear Wave Loads on Floating Structures

Irene Rivera Arreba

Computation of Nonlinear Wave Loads on Floating Structures
Master Thesis

I. Rivera-Arreba

Cover photo - Haliade© - GE Renewable.
Credit: GE Renewable

COMPUTATION OF NONLINEAR WAVE LOADS ON FLOATING STRUCTURES

MASTER THESIS

For obtaining the degree of Master of Science in 'Offshore and Dredging Engineering' at the Delft University of Technology and in 'Technology-Wind Energy' at the Norwegian University of Science and Technology.

I. Rivera-Arreba

at the Delft University of Technology,

7th of August, 2017

University supervisors: Prof. dr. ir. A. Metrikine
                          Dr. ir. E. E. Bachynski
                          Dr. ir. A. C. Viré
Company supervisors: Dr. ir. B. T. Paulsen
                          Ir. N. Bruinsma

EWEM

TU Delft
Delft University of Technology

Deltares
Enabling Delta Life

NTNU – Trondheim
Norwegian University of Science and Technology

PREFACE

This master thesis is submitted as part of the requirement for obtaining the master in Offshore Engineering and Dredging at the Technical University of Delft and in Technology-Wind Energy at the Norwegian University of Science and Technology. The work has been conducted in collaboration between Deltares, within the department of Harbour, Coastal and Offshore Engineering, the Technical University of Delft and the Department of Marine Technology at the Norwegian University of Science and Technology (NTNU) in Trondheim, Norway. The supervision from Deltares has been provided by Dr. ir. Bo T. Paulsen and Ir. N. Bruinsma. Dr. ir. Erin Bachynski and Dr. ir. Axelle Viré have been the daily supervisors from NTNU and TU Delft, respectively.

I consider myself enormously lucky for having been under the supervision of such committed and knowledgeable researchers. This work has only been possible with the guidance and support I could count on. I would like to express my gratitude to Axelle Viré, for, from the very first moment, supporting the idea of doing a thesis with CFD and floating wind platforms more than one year ago, and for all your guidance ever since then. To Erin Bachynski, for your valuable feedback and for sharing your passion and vast knowledge about floating wind turbines with me, during both the master thesis and the pre-thesis research work at NTNU. Thank you to Bo Paulsen, for your support and constant and insightful contributions. Thank you to Niek Bruisma, for your full availability, valuable ideas and for sharing your master thesis work resources. Thank you to Andrei Metrikine, for chairing the committee, and for pushing towards a critical thinking. Thank you to Dr. ir. Niels G. Jacobsen, for sharing your knowledge, and to Ir. Tim Raaijmakers, for giving me the opportunity of carrying out this work at the Harbour, Coastal and Offshore Engineering department at Deltares.

I would also like to express my gratitude towards Deltares for hosting me during these last seven months, and for the computational resources. Finally, thank you to Ermano de Almeida, for your continuous support.

I. Rivera-Arreba
Delft, August 2017

ABSTRACT

Floating wind turbines (FWTs) are proposed as a method to harness the significant wind energy resource in deep water. International research efforts have led to the development of coupled numerical global analysis tools for FWTs in order to understand their behavior under wind and wave actions. The hydrodynamic models in such tools are typically based on first-(and second-)order potential flow theory, sometimes also including Morison's equation. In order to accurately model highly nonlinear waves, their interaction with a floating platform, and obtain estimates of the resulting loads on the structure, a numerical wave tank approach is generally needed.

In this thesis, the response of floating structures to nonlinear wave loading is investigated by means of two different numerical approaches: a fully nonlinear Navier-Stokes/VOF solver and a second-order potential flow theory solver. Firstly, the fully nonlinear Navier-Stokes/VOF numerical wave tank, developed within the open-source CFD toolbox OpenFOAM®framework (version 1606+), is validated against experimental data for two cases. These comprise the response of a 2D floating box and a 3D floating vertical cylinder. In order to model the motions of the floating structures, together with the generation and absorption of the waves, the interDyMFoam solver, provided by the OpenFOAM®library, is extended with the waves2Foam package, developed by Jacobsen et al. (2012). Furthermore, a simple catenary mooring line is implemented for the moored cases. Secondly, a potential flow theory based model of the OC5-semisubmersible floating platform is generated. The frequency-domain analysis is done with the Wadam software and the time-domain simulations with SIMO. This model is validated against measurement data from a 1:50 scale test campaign performed at the MARIN offshore wave basin and the fully nonlinear validated CFD model. Lastly, both numerical models of the OC5-semisubmersible are compared in order to assess the suitability of the diffraction model in two different conditions where nonlinearities are of relevance. The first one involves very long waves, with periods close to 20 s, which are likely to take place under swell wave conditions. These may excite the OC5-semisubmersible platform in heave at its natural frequency. The second situation deals with regular waves with increasing steepness.

In principle, the fully nonlinear CFD model, if no experimental data is available, is needed to calibrate the diffraction model. However, once the latter is adjusted and validated, results are given at a much lower computational cost. According to the computations throughout this work, when dealing with waves with high steepness and high excitation frequencies, the motions, as well as the peak forces, are properly captured by the diffraction model. However, other local effects of importance for offshore structures, such as wave run-up, or the different components in frequency of the loading, require the use of a fully nonlinear CFD solver. Therefore for preliminary design stages a diffraction model is able to give suitable results regarding the motions and peak inline and vertical forces at a much lower computational cost; however, for detailed design, or optimisation phase stages, where local effects are of relevance, a fully nonlinear CFD model is required.

CONTENTS

1

INTRODUCTION

The 12ᵗʰ December of 2015, an agreement was reached at the COP21, the Climate Change Conference, held in Paris. The 195 nations involved in this agreement are bound to a common framework of progressive reductions in greenhouse gas (GHG) emissions. Before this international agreement, the 2020 Objectives were defined by the European Union leaders (EU (2010)). These set of targets were upgraded in 2015, within a new 2030 Framework for climate and energy. These comprise a 40% cut in GHG emissions, at least a 27% share of renewable energy consumption and at least 27% increase in energy efficiency (EU (2014)). Wind energy is playing a significant role as a primary source of emission-free and self-sufficient energy production. Statistics presented in GWEC (2016) state that the global cumulative installed capacity in 2016 was of almost 500 GW, from which more than 14 GW were installed offshore. Although more recently developed, the latter presents various advantages compared to the land based counterpart: wind climates are stronger and more stable, larger turbines are possible due to fewer restrictions, and they do not represent a nuisance to nearby neighbourhoods due to noise.

1.1. OFFSHORE WIND ENERGY

Offshore wind energy in Europe saw a net 1.6 GW of additional installed grid-connected capacity in 2016. By 2020, offshore wind is projected to grow to a total installed capacity of 24.6 GW, as reported by Ho & Mbistrova (2017). The average water depth of wind farms completed, or partially built in 2016 was 29 m, 30% more than in 2014, and the average distance to shore was 44 km, 34% further with respect to 2014; the tendency is to move further from the coast to larger water depths. This has a direct consequence on the technology, since the feasibility of current installed offshore wind turbine bottom-fixed foundations, mainly monopiles and jacket foundations, is likely to be limited to a certain depth. Most of the current commercial scale offshore wind developments take place in the North Sea, where the limited water depth and the geotechnical conditions allow for fixed foundations. However, as stated in the Floating Offshore Wind Vision Statement (WindEurope (2017)) 80% of all the offshore wind resource in Europe is located in waters 60 m and deeper, where traditional bottom-fixed foundations are no longer as feasible. An example of this is certain places of the Mediterranean Sea or off the Norwegian coast. This equally applies to numerous areas worldwide, such as Japan, which counts with more than 500 GW wind resource potential located at larger water depths than 60 m. Therefore, floating offshore wind (FOW) holds the key to access an inexhaustible energy source, not only in Europe but worldwide.

1.1.1. FLOATING WIND ENERGY

An increase in offshore wind installations is needed to meet renewable electricity generation targets set by the European Commission, among others. The potential for floating wind capacity in Europe is of 4000 GW, found in areas with larger water depth than 60 m. Therefore, improving conditions for floating offshore wind will enhance the deployment of overall offshore wind capacity and subsequently support the EU in reaching the 2030 targets.

There are currently three main substructure designs for floating offshore wind with different stability criteria: spar buoy, semisubmersible and tension leg platform, which are presented in Figure 1.1. The first two are loosely moored to the seabed, allowing for easier installation, while the tension leg platform is more firmly connected to the seabed, which allows for a more stable structure.
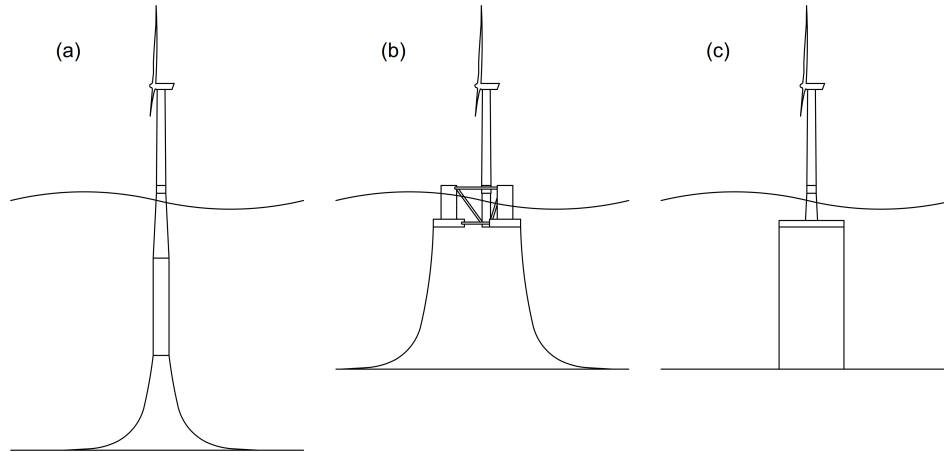

Figure 1.1: Floating offshore wind turbine concepts.

Spar buoy: its basic characteristic is the large vertical draft. Its stability is gravity-based, with the centre of gravity as low as possible, and the distance from the keel to the buoyancy as large as possible. It is self-stabilised using ballast, and moored by catenary lines. It is the simplest concept, but due to the large weight and the draft it presents, water depths of at least 100 m are needed. It corresponds to subfigure (a) in Figure 1.1.
The spar-buoy concept Hywind (Jonkman (2010)) was tested in 2009 by the Norwegian company Statoil off the coast of Norway, where large depths can be found. The same company has recently started the assembly of the world's first floating wind farm off the coast of Peterhead in Scotland. It consists of five wind turbines of 6 MW each.

Semisubmersible: this concept is water-plane inertia based, meaning that it presents large geometrical inertia. It is usually made of three or four vertical cylinders connected by pontoons or braces. The restoring force in the horizontal motions is gained using catenary moorings. Heave plates are attached to the bottom of the columns, to increase the added mass, damping and drag. It can be placed at a wide range of water depths, and it can be installed at the quayside and then towed to site. However, it is a complex and heavy steel structure, and due to the large wave loads to which it is subjected, tilt has to be limited, either by ballast, or by increasing its dimensions, and therefore its weight. It corresponds to subfigure (b) in Figure 1.1.
Two examples of this type of concept are the WindFloat (Roddier et al. (2011)), from Principle Power, and the Tri-Floater (Huijs et al. (2014)), from GustoMSC. The prototype of the former was installed off the coast of Portugal until summer 2016, and is expected to be commissioned by 2018-2019.

Tension Leg Platform (TLP): this concept is kept upright by means of external forces, provided by stiff vertical tethers, known as tendons, which counteract the excess of buoyancy that the structure presents. The excessive buoyancy creates pretension and limits heave and pitch motions; these reduced motions are expected to decrease the structural loading on the tower and blades Bachynski (2014) compared to the other floating concepts, without requiring the large draft of a spar or the spread mooring system and complex construction of a semisubmersible. However, the anchoring system may comprise a challenge. It corresponds to subfigure (c) in Figure 1.1.
Up until now no multi-MW prototypes of the TLP have been built, although some companies have established different concepts. An example of these is the company Glosten, where the TLP concept PelaStar, has been developed.

1.2. RESEARCH MOTIVATION

Within the objective of increasing the share of renewable energy sources in the market, the offshore wind energy industry is moving towards deeper waters, which requires the development of economically and technically feasible structures. To understand the behaviour of these structures under wind and wave actions, international research efforts have led to the implementation of coupled numerical global analysis tools. The current research is therefore driven by the need of lowering the costs of floating wind energy by understanding the physical processes involved with more efficient numerical models.

1.3. SCOPE AND RESEARCH OBJECTIVES

The aim of this research is to assess less computationally expensive potential flow diffraction solver performance when dealing with complex fluid-structure interaction problems, compared to a fully nonlinear numerical model. This way, insight on when a diffraction model can be used for certain situations, or when a nonlinear numerical model is required, can be provided. To achieve the main goal, an analysis of the response of the DeepCWind OC5-semisubmersible offshore floating wind platform, depicted in Figure 1.2, with both numerical models for different conditions, is completed, in order to answer the main research question:

> **How does a (second-order) potential flow theory based diffraction model compare to a fully nonlinear Navier-Stokes numerical wave tank when solving complex fluid-structure interaction problems for offshore floating wind platforms?**

Three sub-questions are addressed to solve the main question:

1. *Is the nonlinear numerical wave tank capable of predicting the motions and capturing the nonlinearities of floating bodies subjected to steep regular waves?*

   Prior to comparing the performance of both models, an extended validation of the nonlinear numerical wave tank for two floating structures is needed.

2. *How does the motion of a semisubmersible floating platform under heave resonance conditions computed by both numerical models compare?*

   Long period ocean swell following a storm can excite semisubmersibles at resonance in heave, and strong nonlinear effects in the response may arise. This question aims at comparing both numerical models structural response under these conditions.

3. *What is the limit of a potential flow based solver regarding wave steepness?*

   Special attention is paid to extreme waves and their consequences for structures, for which a better understanding is needed. In this work the aim is to compare the fully nonlinear model response to waves increasing in steepness against the diffraction model.

1.3.1. RESEARCH APPROACH

Five main research objectives have been set to answer the main research question and sub-questions.

1. To understand the assumptions and limitations of the two numerical models by:

   - carrying out a literature review of the most used numerical tools used to model fluid-structure interaction and

   - completing an in-depth research of the two numerical models to be assessed.

2. To perform an extensive validation of the nonlinear numerical wave tank by analysing the behaviour of a 2D box and a 3D vertical floating cylinder by means of free decay tests, wave propagation and the response of the body to steep regular waves.

3. To develop a diffraction model for the OC5-semisubmersible concept considering first- and second-order potential flow effects including the computation of:

   • its hydrodynamic properties in the frequency-domain and

   • its response amplitude operator.

4. To validate the diffraction model against the fully nonlinear Navier-Stokes model and the experimental data by means of:

   • comparing the natural response and

   • its response when subjected to regular waves.

5. To assess the performance of both numerical models:

   • in regular waves with periods close to resonance conditions and

   • in regular waves with increasing steepness, close to their breaking limit.
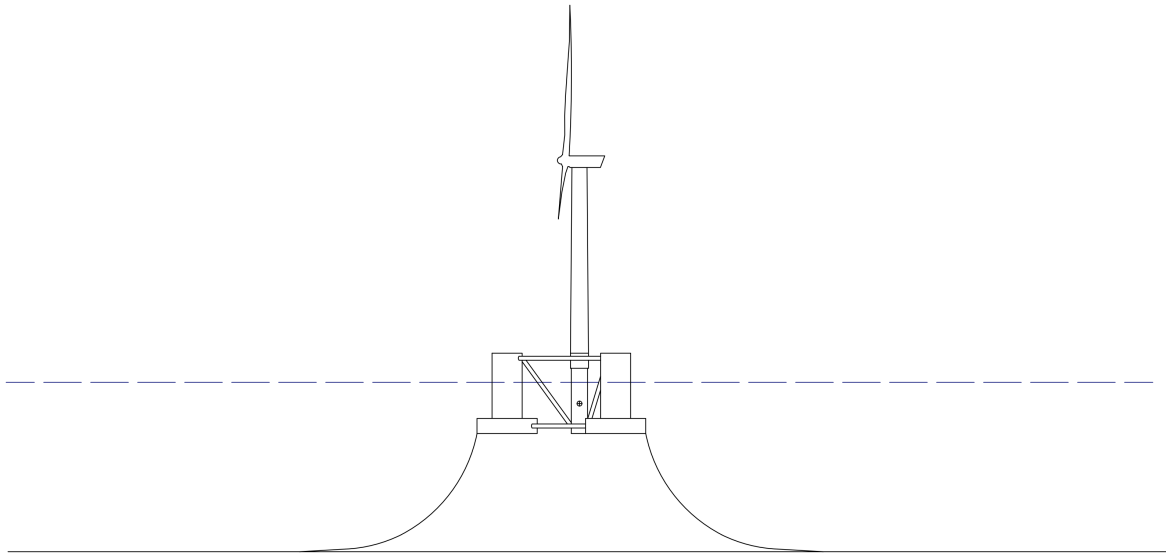
Figure 1.2: Schematic overview of the OC5 floating offshore wind turbine system. It consists of the 5MW NREL turbine on top and the tower mounted on the semisubmersible try-floater, which is moored to the seabed by three catenary mooring lines.

1.4. THESIS OUTLINE

Chapter 2 provides a summary of the concepts and background information relevant to analyse the behaviour of floating structures and the different waves characteristics. Chapter 3 reviews the two numerical models used to asses the response of a floating structure. Chapter 4 presents the further validation of the nonlinear numerical wave tank for two floating bodies. Further information on the cases is provided in Appendix A. Chapter 5 analyses the OC5-semisubmersible floating wind platform and is extended by Appendix B, where the main structural properties and dimensions of the structure are provided. Chapter 6 summarises the key findings and gives recommendations for future studies.

<div align="right">

2

</div>

BACKGROUND AND THEORY

2.1. INTRODUCTION

This chapter gives an overview of the background information and theory on which the current research is based. It is divided into two parts: the first one, Sections 2.2 and 2.3, describes the general hydrodynamics of floating bodies, including their stability, their hydrodynamic properties, their unforced response and their behaviour to incoming waves. The OC5-semisubmersible concept, to be evaluated at a further stage, is considered in particular. The second part, Sections 2.4 and 2.5, addresses the different types of free surface waves, including the measure of nonlinearity degree and the main wave theories used to describe them. A brief background about the numerical simulation state-of-the-art of wave-structure interaction is presented in Section 2.6. A schematic overview of the structure of this chapter is depicted in Figure 2.1.
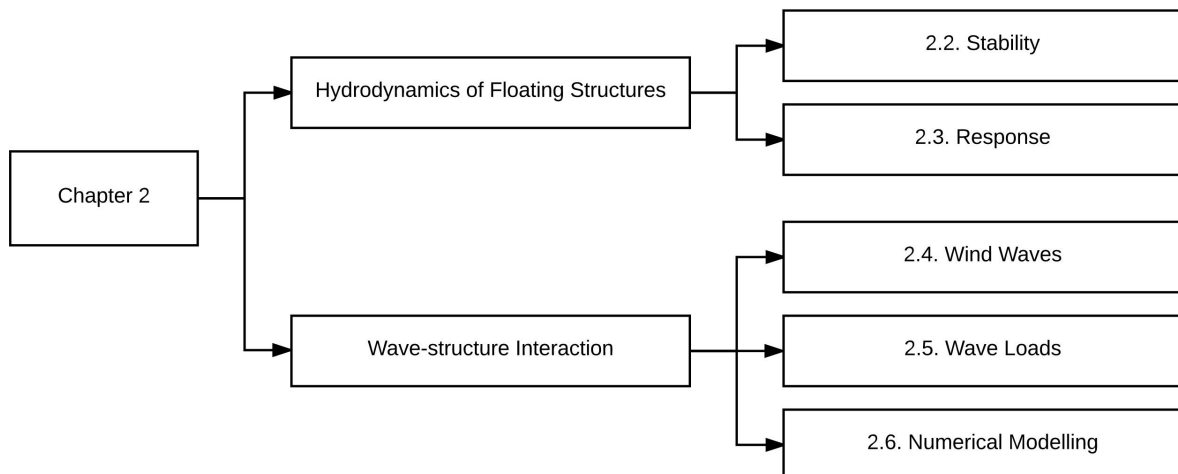
Figure 2.1: Scheme of Chapter 2 structure.

2.2. STABILITY OF FLOATING BODIES

The static equilibrium of a floating wind support structure is achieved when the total weight M_g of the system is equal to the buoyancy force F_B. The weight is calculated as the sum of the weight of every component. The buoyancy force F_B is defined by Journée & Massie (2001) as *the vertical upthrust that the structure experiences due to the displacement of the fluid.* In other words, it is equal to the weight of the volume of displaced water due to the presence of the floating system, as:

$$F_B = \rho g V, \tag{2.1}$$

where ρ is the density of water, equal to $1025\,\text{kg/m}^3$ and V the displaced volume. The centre of the displaced volume is the centre of buoyancy (B), and its position in an inertial reference frame is denoted as z_B. The centre of gravity (COG) of the structure is the point through which the whole weight of the structure acts, for static considerations, and its position in an inertial reference frame is denoted as z_G. To be in equilibrium, the COG and B have to be aligned. If the structure is brought out of equilibrium or balance by a disturbance, such as a force or a moment, they are not aligned anymore, and the system translates and/or rotates about its centre of gravity. The rotation about the structure longitudinal horizontal axis is known as the heel and its rotation about the transverse horizontal axis as trim. This is influenced by both dynamic and static properties, as explained in Journée & Massie (2001). The consequence of heeling with an angle ϕ is that the shape of the submerged part of the structure changes, and the centre of buoyancy goes from B to B_ϕ on a line parallel to the line through the centres of the emerged and immersed wedges $\overline{z_e z_i}$.

(a) Rotational equilibrium at an angle of heel.   (b) Righting and heeling moment at an angle of inclination.
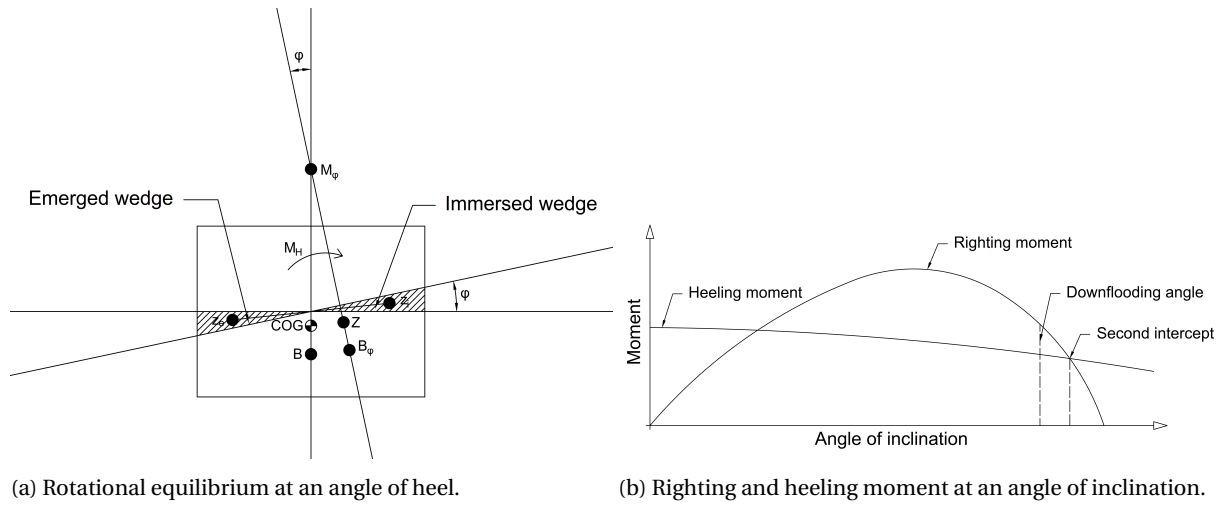
Figure 2.2: Equilibrium of a floating body (a), modified from Journée & Massie (2001) and design standards regulation for heeling moment and angle of inclination for floating wind turbines (b), modified from DNV (2013).

An equilibrium is achieved when the righting stability moment M_S becomes equal to the external heeling moment M_H, as:

$$M_S = \rho g V \overline{GZ}, \tag{2.2}$$

where $\overline{GZ}$ is the stability (or righting) lever arm, equal to $\overline{GM_\phi}\sin\phi$; M_ϕ is the metacentre and G denotes the COG. It is defined as the point of intersection of the lines through the buoyant vertical forces at a zero angle of heel and an angle of heel ϕ. Its position depends on the new position of the centre of buoyancy, B_ϕ. The metacentric height $\overline{GM}$ is the difference between the vertical level of the metacentre and the COG. If the latter is below the metacentre, the floating body is at equilibrium, whereas if it is above, it is unstable. The metacentre can be found analytically or experimentally, although it can be assumed to be fixed in the case that tilt angles are small. Otherwise, it requires more extensive calculations. The B and COG positions, z_B and z_G, respectively, are given by:

$$z_B = \frac{\sum_i z_{B,i} V_i}{V} \qquad \text{and} \qquad z_G = \frac{\sum_i z_{G,i} M_i}{M}, \tag{2.3}$$

where $z_{B,i}$ ($z_{G,i}$) and V_i (M_i) are the center of buoyancy (gravity) and volume (mass) of each element i in which the structure can be decomposed, respectively. The metacentric height $\overline{GM}$ can be expressed in terms of the keel K of the body as $\overline{GM} = \overline{KB} + \overline{BM}$.

Figure 2.3: Degrees of freedom of a floating rigid body: three translations along and around the x, y and z axes.

According to the standard code *Design of Floating Wind Turbine Structures*, DNV (2013), for column-stabilised structures, such as semisubmersibles, *a positive righting moment from upright position to the s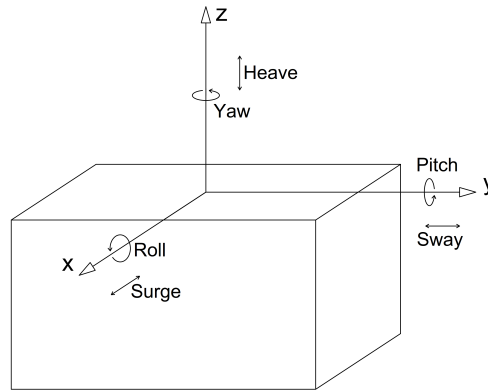econd intercept of righting and wind heeling moment curves.* Furthermore, *the area between the righting moment curve and the wind heeling moment to the angle of downflooding shall be equal to or greater than 130% of the area under the wind heeling moment curve to the same limiting angle*: this is known as the area-ratio-based criterion. Alternatively, dynamic-response-based intact stability criteria have recently been adopted for floating offshore wind turbines, initially developed for column-stabilised drilling units and later extended to the design of floating production installations, as reported in Masciola et al. (2008).

2.3. Motions and Response of a Semisubmersible

This thesis deals with three different floating structural configurations, namely a 2D rectangular box, a vertical cylinder and the OC5 Floating Offshore Wind Turbine (FOWT). The latter was developed within the Offshore Code Comparison, Collaboration, Continued, with Correlation (OC5) project, as a continuation of the Offshore Code Comparison Collaboration (OC3) and the two-phased Offshore Code Comparison Collaboration and Comparison (OC4), as reported by Robertson et al. (2014). It is a semisubmersible try-floater moored to the seabed by three catenaries, as depicted in Figure 2.3. The pitch-controlled 5MW horizontal-axis wind turbine, developed by Jonkman (2009) at the National Renewable Energy Laboratory (NREL), is mounted on it. Throughout this work the floating structure is assumed to be a rigid body, meaning that it has six degrees of freedom along, or around, it can translate, or rotate, as indicated in Figure 2.3. The behaviour of a floating structure in its six degrees of freedom is described by the Equation of Motion:

$$[\mathbf{M} + \mathbf{A}]\ddot{\mathbf{x}} + \mathbf{B}\dot{\mathbf{x}} + [\mathbf{C} + \mathbf{K}]\mathbf{x} = \mathbf{F}_{exc}, \tag{2.4}$$

where $\mathbf{A}$ is the added mass matrix, $\mathbf{B}$ the damping matrix and $\mathbf{C}$ and $\mathbf{K}$ the restoring matrices. The former is given by the hydrostatic stiffness, whereas the latter comes from, if existent, the mooring system, and $\mathbf{x}$ (t) is the motion vector. $\mathbf{F}_{exc}$ denotes the wave excitation loads, corresponding to the Froude-Krilov and the diffraction loads. From this equation the undamped natural frequencies of the system can be found by solving the homogeneous system and solving for ω. If the coupling between the degrees of freedom is neglected, the undamped natural frequency $\omega_{n,i}$ (or natural period $T_{n,i}$) for each degree of freedom i yields:

$$\omega_{n,i} = \sqrt{\frac{C_{ii} + K_{ii}}{M_{ii} + A_{ii}(\omega)}} \longrightarrow T_{n,i} = 2\pi\sqrt{\frac{M_{ii} + A_{ii}(\omega)}{C_{ii} + K_{ii}}}; \qquad i = 1, 2, ...6, \tag{2.5}$$

where C_{ii} and K_{ii} are the restoring coefficients and A_{ii} the added mass coefficients, dependent on the frequency. The hydrostatic restoring coefficient is non-zero for the vertical motions, namely heave, roll and pitch. The restoring coefficients K_{ii} are given by the mooring system stiffness. If the damping of the system is taken into

account, the damped natural frequency, expressed with respect to the undamped natural frequency and the critical damping ratio ξ_i, yields:

$$\omega_{n,i,damp} = \omega_{n,i}\sqrt{1 - \xi_i^2}, \tag{2.6}$$

where the critical damping ratio is given by:

$$\xi_i = \frac{B_{ii}(\omega)}{2\omega_n(M_{ii} + A_{ii}(\omega))}. \tag{2.7}$$

In linear wave theory, the wave force is proportional to the wave amplitude, and is given by the response amplitude operator (RAO), defined as the response amplitude $|x_i|$ per unit wave amplitude A. Following from the equation of motion in the frequency domain, the transfer function yields:

$$\frac{|x_i|}{A} = RAO(\omega) = [-\omega^2(\mathbf{M} + \mathbf{A}(\omega)) + i\omega\mathbf{B}(\omega) + \mathbf{C}]^{-1}\tilde{\mathbf{F}}_{\mathbf{exc}}(\omega). \tag{2.8}$$

From the computation of the RAO, the most relevant frequencies of the structure are likely to show up; for instance, the natural frequencies or the cancellation frequencies, where the response amplitude operator presents the largest value and the smallest values, respectively. The degrees of freedom of main interest in the current research are the heave and the pitch motion, for which their natural response derivation is presented in the following.

NATURAL RESPONSE IN HEAVE

The undamped natural frequency in heave, neglecting any couplings, is derived from Equation 2.5, and yields:

$$\omega_{n,3} = \sqrt{\frac{C_{33} + K_{33}}{M_{33} + A_{33}(\omega)}}, \qquad \text{with} \qquad C_{33} = \rho_w g A_{wp}. \tag{2.9}$$

The terms that play a role are the added mass and the hydrostatic stiffness, which depend on the waterplane area A_{wp}. In the case of the OC5-semisubmersible, it is given by the three main columns (MC) and the central column (CC) section contribution. Three elliptical sections of the braces also contribute to this term, but their diameter is negligible with respect to the columns one. Furthermore, the OC5 has three heave plates (HP) on the base of the three main columns, which increase the added mass, and consequently, the natural period; this way the structure first natural frequency in heave does not lie in a region where waves are likely to present a large amount of energy. The inertia term in heave is formed by the total mass of the system and by the added mass in heave. The latter depends on the frequency; for hand-calculations, the low-frequency limit is taken into account. According to Sarpkaya & Isaacson (1981), the added mass of a disk oscillating along its axis can be approximated as the mass of a sphere of water enclosing the disk, or $1/3\rho D^3$. For the heave plates attached to the main columns base, there is only a part that contributes to the added mass. A good approximation for the current structure, formed by three main columns, a central one, three heave plates, and neglecting the slender elements, is given by Tao & Cai (2004) as:

$$A_{33} = \rho\frac{D_{CC}^3}{6} + 3\rho\left[\frac{D_{HP}^3}{3} - \left[\frac{D_{MC}^2\pi}{8}\left(D_{HP} - \sqrt{D_{HP}^2 - D_{MC}^2}\right) + \frac{\pi}{24}\left(D_{MC} - \sqrt{D_{HP}^2 - D_{MC}^2}\right)^2\left(2D_{HP} + \sqrt{D_{HP}^2 - D_{MC}^2}\right)\right]\right] \tag{2.10}$$

The only term remaining is the mooring system stiffness contribution. In principle, this one is negligible with respect to the hydrostatic one, and therefore has a relatively small effect on the natural response of the system in heave.

From Equation 2.5, the undamped natural frequency in pitch, if any couplings are neglected, is given as:

$$\omega_{n,5} = \sqrt{\frac{C_{55} + K_{55}}{I_{55} + A_{55}(\omega)}}, \qquad \text{with} \qquad C_{55} = M_g(z_B - z_G) + \rho g I_y, \tag{2.11}$$

where I_y is local the moment of inertia of the waterplane area of the different elements. It is transferred to the global axis of moments using Steiner's theorem. For the main columns and the central column, the local moment of inertia is equal to the moment of inertia of a circular cross-section area, $\pi D^4/64$. For the hand calculations, the slender elements contributions are neglected. The mass moment of inertia I_{55} is given by the mass moment of inertia about the y-axis of the entire system, based on every element's contribution.

The low-frequency limit added mass component in pitch A_{55} is computed based on strip theory and neglecting the slender elements contribution. Based on Ghadimi et al. (2012), and assuming an added mass coefficient in surge equal to one, it yields:

$$
\begin{aligned}
A_{55} = 3\rho\pi \frac{D_{HP}^2}{4} &\left(\frac{|z_{k,HP}|^3}{3} + (z_{G,HP} - z_{k,HP})^2 |z_{k,HP}| + (z_{G,HP} - z_{k,HP})|z_{k,HP}|^2 \right) + \\
&+ \rho\pi \frac{D_{CC}^2}{4} \left(\frac{|z_{k,CC}|^3}{3} + (z_{G,CC} - z_{k,CC})^2 |z_{k,CC}| + (z_{G,CC} - z_{k,CC})|z_{k,CC}|^2 \right) + \\
&3\rho\pi \frac{D_{MC}^2}{4} \left(\frac{|z_{k,MC}|^3}{3} + (z_{G,MC} - z_{k,MC})^2 |z_{k,MC}| + (z_{G,MC} - z_{k,MC})|z_{k,MC}|^2 \right),
\end{aligned}
\tag{2.12}
$$

where $z_{k,i}$ denotes the vertical position of the bottom of the respective element. The stiffness contribution from the mooring system has a more important effect, relative to the one it has in the heave motion, although not as relevant as the effect it has in the horizontal motions.

2.3.1. LINEAR AND QUADRATIC DAMPING COEFFICIENTS CALCULATION

In this research, the natural periods of the floating structures are computed using decay tests. The structure is displaced to a given offset and then released. From the response, the natural period, linear and quadratic damping coefficients are obtained. As described in Hoff (2001), the numerical recreation of a sinusoidal free-decay test of a system can estimate the natural period of the motion and outputs the linear and quadratic damping coefficients necessary to model the free-decay test. Assuming that the motions $\mathbf{x}$ are uncoupled and approximating the restoring forces to be linear the decay for any degree of freedom is given by:

$$\ddot{\mathbf{x}} + b_1 \dot{\mathbf{x}} + b_2 |\dot{\mathbf{x}}|\dot{\mathbf{x}} + \omega_n^2 \mathbf{x} = 0 \tag{2.13}$$

where b_1 and b_2 are the linear and quadratic damping coefficients. The energy per mass V is given by:

$$V(t) = \frac{1}{2}\dot{\mathbf{x}}^2 + \frac{1}{2}\omega_n^2 \mathbf{x}^2 \tag{2.14}$$

The loss of energy $L(V)$ over each cycle can be found as:

$$L(V) = -\frac{d}{dt}V = b_1 V + b_2 \frac{8}{3} 2\sqrt{2} V^{1.5} \tag{2.15}$$

At the troughs and peaks at t_n, $\dot{\mathbf{x}} = 0$, so V is calculated from the amplitude $\mathbf{x}_n$ with Equation 2.16. b_1 and b_2 are obtained by a least-squares fit. ω_0 can be initially approximated to the undamped natural frequency.

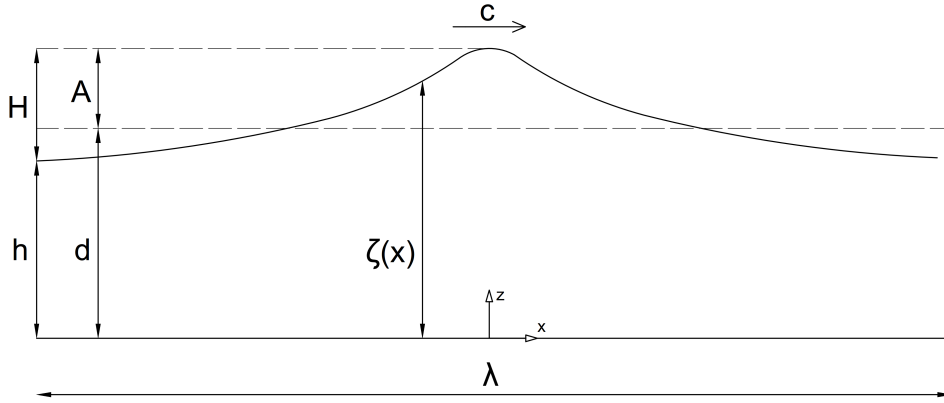$$V(t_n) = \frac{1}{2}\omega_n \mathbf{x}_n^2 \tag{2.16}$$

Figure 2.4: Main parameters that describe a regular wave propagating in the x-direction. Modified from Rienecker & Fenton (1981).

2.4. WIND WAVES

Wind-waves take place at the free surface of bodies of water. The main parameters used to characterise them are the water depth d, the wave height H, defined as the crest-to-trough distance, and the wave length λ, the distance between two consecutive crests. Alternatively to the wave length, the period T or the frequency ω can be used. They are related by the so-called dispersion relation, applicable to linear waves, and defined as:

$$\left(\frac{2\pi}{T}\right)^2 = \omega^2 = gk\tanh(kh),$$

(2.17)

where $k = \dfrac{2\pi}{\lambda}$ is the wave number. The asymptotic value of the dispersion relation in deep-water waves is $\omega^2 = gk$. From this relation the wave celerity, or relative wave velocity, can be found as $c = \dfrac{\lambda}{T}$. The presented parameters are depicted in Figure 2.4.

There are several theories used to describe regular waves; the use of one or the other is mainly driven by the water depth and by the wave height to wave length ratios. The former defines how the seabed may influence the wave propagation, or, in other words, how large the depth with respect to the wave is. If the wave length is larger than twenty times the water depth, the wave is said to be a shallow-water wave, whereas if it is smaller than seven, it is a deep-water wave. If it lies between seven and twenty, then the wave is an intermediate-water wave. The second ratio, which relates the wave height with the wave length, describes the steepness of the wave. It measures the nonlinearity of the wave: the larger the ratio, the steeper the wave. A similar parameter to measure the steepness of the wave is the nondimensionalized wave amplitude kA. A third parameter is the ratio between the wave height and the breaking wave height H_{max}, which depends on the wave length and the water depth ratio, and is defined, according to Fenton (1988), as:

$$\frac{H_{max}}{d} = \frac{0.141063\dfrac{\lambda}{d} + 0.0095721\left(\dfrac{\lambda}{d}\right)^2 + 0.0077829\left(\dfrac{\lambda}{d}\right)^3}{1 + 0.0788340\dfrac{\lambda}{d} + 0.0317567\left(\dfrac{\lambda}{d}\right)^2 + 0.0093407\left(\dfrac{\lambda}{d}\right)^3}.$$

(2.18)

The applicability of the different regular wave theories depending on the water depth and the wave height is depicted in Figure 2.5. Note that the named analytical theories are only valid up to the theoretical breaking wave limit.
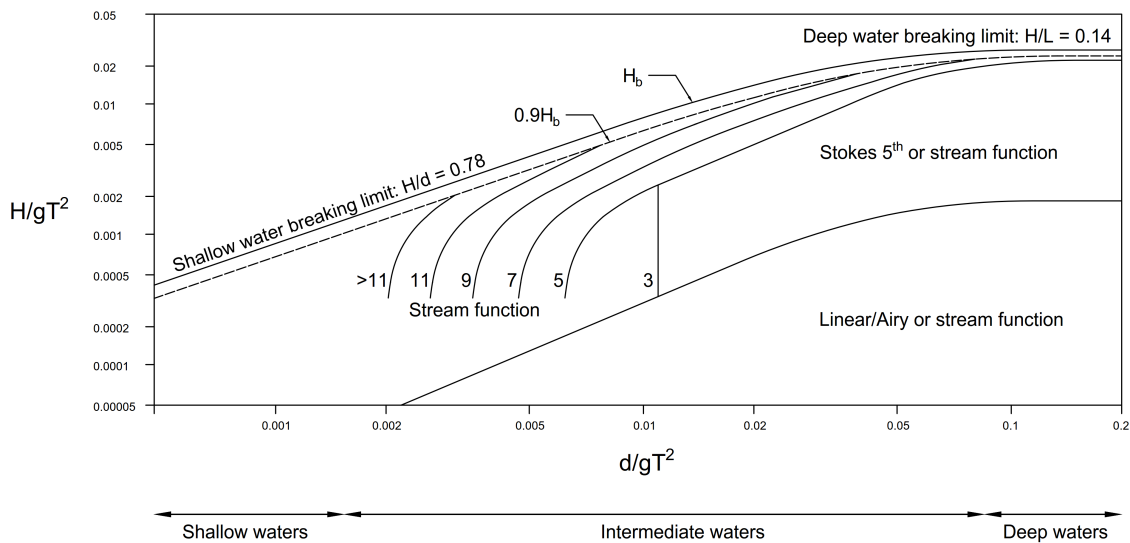
Figure 2.5: Wave theories limit of application depending on the wave height to wave length and on the depth to wave length ratio DNV (2013).

Small non-steep waves

Non-steep waves are in general characterised by $kA = O(\epsilon)$, where the nonlinearity $\epsilon \ll 1$. The first-order solution is linear in ϵ and applies to those waves sufficiently small that propagate in intermediate to deep waters and can be described as a sine function. The principle superposition applies for these cases. The theory assumes that the fluid layer has a uniform mean depth and that the fluid flow is inviscid, incompressible and irrotational. They are not relevant for extreme load cases. However, given the high frequency of occurrence, they become important when dealing with fatigue loads on offshore structures. The shape of these waves is depicted in Figure 2.6, (a).

Steep nonbreaking waves

This type of waves is characterized by $kA \approx O(10^{-1})$. As the degree of nonlinearity ϵ increases, either by a decrease in water depth or by an increase in wave height, the higher-order nonlinear effects, proportional to ϵ^n, where $n = 2, 3...$, become larger. The wave can no longer be described by linear wave theory: the trough gets flattered and the crest shorter, as depicted in Figure 2.6, (b). Two of the most well-known theories used to describe higher-order waves are the Cnoidal theory or higher order Stokes solutions, based on perturbation methods. However, they cannot be applied to every type of waves. The former wave theory is limited to shallow water applications, whereas the latter is mainly applicable for deep water waves. Neither can describe waves with higher wave heights. On the effort to develop a have a theory that could describe every type of waves, the fully nonlinear stream function was presented by Rienecker & Fenton (1981), based on the numerical determination of the Fourier coefficients. Note that this theory is not applicable to realistic irregular seas.

2.5. Wave Loads on Surface Piercing Cylinders

The interaction of the sea (waves and current) and wind with offshore structures induces loads and motions, which depend on the relative dimensions and features of the factors involved. Since circular cylinders are a fundamental part of many offshore structures, special attention is paid to loads on these. The dimensions are usually defined by the diameter D, relative to the wave length λ and to the wave height H. Figure 2.7 provides a qualitative hydrodynamic classification of the dominant loads on a circular piercing cylinder, depending on λ/D and H/D. Below the wave breaking limit, if a cylinder is relatively wide with respect to the wave length, $\frac{\lambda}{D} < 5$, diffraction loads are important, i.e. those induced by the incident waves and their modification (diffraction) due to the structure. If $\frac{\lambda}{D} > 5$, the incident waves tend to be unaffected by the structure, and long-wave approximation can
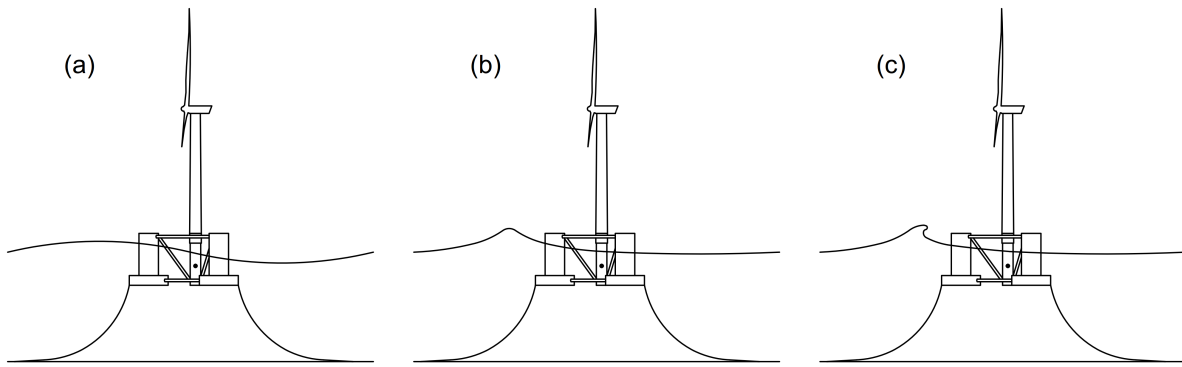
Figure 2.6: Types of waves on a floating structure. a) Linear waves, with a weak nonlinear wave forcing. b) Weakly nonlinear waves, with a nonlinear wave forcing component. c) Breaking waves.

be used. In this case the induced loads are related to the kinematics of the incident waves at the centre of the body. Mass loads, proportional to acceleration, are in general dominant if the wave steepness is small, $\frac{H}{D} < 10$. As λ/D becomes larger, the wave behaves similarly to a slow-varying current. For H/D closer to the wave-breaking limit, nonlinear effects become important. Above this limit, waves can easily break during the interaction with the structure. Below this limit, if $\frac{H}{D} > 10$, for sufficiently large $\frac{\lambda}{D}$, viscous loads become dominant.

One of the most widespread approaches to compute the hydrodynamic loads on cylinders is the Morison's equation (Morison et al. (1950)), a semi-empirical superposition of first-order inertial loads and second-order viscous drag. Its formulation is given in Chapter 3, Section 3.3.5. The first assumption of this formulation is that the diffraction potential is constant across the body. This does not apply to the main components of the floating structure, in general, since λ/D for the most representative sea states is smaller than 5. The second assumption is that the viscous drag dominates the drag loading, and therefore the radiation damping is ignored. In the case of floating wind structures, this is not usually the case, since radiation damping is usually relevant. The third simplification Morison's equation implies, relevant to offshore wind floating structures, is the discard of the added-mass induced coupling between the hydrodynamic force and the support structure acceleration. Another short-come is the fact that it does not compute any end effects, which for floating cylinders may be relevant. Furthermore, Morison's equation is based on linear wave theory, so it is not able to describe nonlinear free-surface effects, such as slamming, springing or ringing.
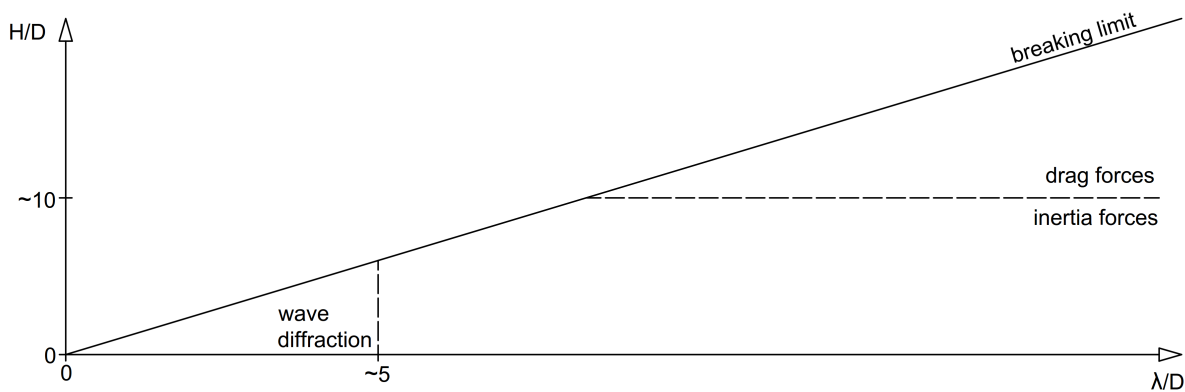

Figure 2.7: Wave theories limit of application depending on the wave height to wave length and the depth to wave length ratio.

2.5.1. LOADS FROM STEEP REGULAR WAVES

These loads are caused by impacts from steep nonlinear waves. Weakly nonlinear solutions, based on perturbation methods and accurate up to the third order in kA, have been derived by Faltinsen et al. (1995), known as the FNV model, and Malenica & Molin (1995). The FNV analysis was extended for the case of unidirectional irregular waves, as published by Newman (1996). Recently, Paulsen et al. (2014b) showed that Morison's equation predicted the time history of the inline force accurately on a circular cylinder from steep non-breaking waves, although the detailed loading in the free surface region and the higher nonlinear forcing was not captured. This type of wave forces can give rise to the third-order strong nonlinear phenomenon known as ringing, which is a high-frequency transient response caused by very steep waves in extreme sea states, as studied by Rainey (2007). Slamming is another strong nonlinear phenomenon that may arise, caused by a very steep or breaking wave. Slamming forces may lead to large local damage, affecting not only the local structural integrity but also the global elastic behaviour. Its occurrence depends on the local structure-fluid relative motion, and its features depend on the local geometry in the impact region, as well as on the kinematic and dynamic conditions at the impact. A thorough description of this phenomenon can be found in Faltinsen (2005).

2.6. NUMERICAL MODELLING OF WAVE-STRUCTURE INTERACTION

The numerical simulation of free surface flow problems has a high degree of importance in the development of offshore structures. Several types of models exist, from which three main groups are well-known: Boussinesq-type, potential flow and Navier-Stokes solvers.

Boussinesq-type solvers present low computational costs and a reasonable accuracy for linear and weakly nonlinear waves, as long as the wave length is large compared to the water depth. A thorough review and analysis of these type of models is found in Madsen & Fuhrman (2012).

Potential flow theory is widely used to compute the wave loading on offshore structures. It assumes the fluid to be incompressible, irrotational and inviscid. It can predict global wave pattern, and the grid is fully automated. However, it cannot model breaking-waves or problems in which extreme nonlinearities take place. One of the most well-known tools is the WAMIT® software, developed by Lee & Newman (1989). The diffraction model used throughout this research is based on this one, as described in Chapter 3, Section 3.3.

Strongly nonlinear problems require the use of fully nonlinear viscous numerical models. These are computationally more expensive, but in the last years, the development of computational power has decreased the costs. They solve the fully nonlinear Navier-Stokes equations together with the continuity equations. The methods are under continuous research and development. Today there are three different main approaches to this problem: Direct Numerical Simulation (DNS), Large Eddy Simulation (LES) and Reynolds Average Navier Stokes (RANS). The first one solves the equations without the implementation of any turbulence model. Thus, to solve the smallest eddies that may take place, the cell length scale has to be of the order of the smallest eddy in the turbulent boundary layer. This method yields a more detailed solution of the flow field but requires a high demand of both computational and time resources. The second method ignores the smallest length scales, which are the most computationally expensive to resolve, using a low-pass filtering of the Navier–Stokes equations. However, the effect of this small-scale information from the numerical solution must be modelled for the problems that require it. These two methods are more used in academia. The third, and most widespread approach in the industry uses turbulence models, from which the most popular today is the standard $\kappa - \epsilon$ model. However, turbulence is still not fully understood, and there are no convincing turbulence models available yet. In the current research an unresolved DNS approach is used, or, in other words, no turbulence models are implemented, although the mesh length scale is not as high as it should be for the eddies to be captured.

The discretisation of the fluid domain, to solve the equations, can be meshless or grid-based. An example of the first type is the smoothed-particle hydrodynamics (SPH), which uses a Lagrangian approach, i.e. the coordinate moves with the fluid. The main advantage is that they are better at dealing with large local distortions than grid-based methods. Grid-based methods cannot intercept the free surface by themselves. Instead, an additional equation is needed. There are two types of methods to describe the free-surface: the surface tracking methods and the surface capturing methods. The first one uses a Lagrangian-type surface method. It is based on a representation of the free surface by special marker points. Between marker points, interpolation is used. With this method, the position of the interface is known, and it is advected across the domain. However, it does not assure continuity, for instance, if the interface is significantly deformed or the vorticity is large. The second method is an Eulerian-type volume method, which supports an implicit tracking of the surface of a two-phase flow. The

fluid is marked on either side of the interface. To reconstruct the interface, specific techniques are needed, since the exact position of the free surface is not known. One of the most widely used is the Volume of Fluid (VOF), by Hirt & Nichols (1981). The indicator to mark the fluid is the volume fraction, a scalar between zero and one. The main advantage is the assurance of the properties conservation. Many commercial software are based on the coupling of this method with the Navier-Stokes solver, such as StarCCM+ and Fluent (Ansys).

The approach used throughout this research is OpenFOAM® (Open Field Operation And Manipulation), an open-source model widely supported by a large user community. This library comes with a large number of solvers for many different types of problems. Here, the interFoam solver provided by OpenFOAM® is extended by the wave generation and absorption toolbox waves2Foam, developed by Jacobsen et al. (2012). The finite volume method is used for the fluid domain discretisation, whereas for the free-surface tracking the Volume of Fluid method is used. This same approach, including the waves2Foam toolbox, was used in Paulsen et al. (2014*a*) to analyse the wave forcing from steep and fully nonlinear wave on bottom-founded wind turbines.

Other approaches have been applied in order to compute nonlinear waves. One of them is the fluid-impulse theory (FIT), published by Chan et al. (2015), used to calculate the nonlinear surge diffraction force on the MIT/N-REL TLP turbine. It allows the evaluation of second-order and higher-order nonlinear effects by means of using compact force expressions, applied as time derivatives of impulses. The quadratic wave loads are implemented as integrals of the velocity potentials and the source strength distribution over a body wetted surface and the internal waterplane area. This method avoids the meshing of the infinite exterior free surface.

Another approach to simulate wave-structure interaction, used in Viré et al. (2016), is the immersed-body method (IBM). It uses two distinct meshes: one covers the entire computational domain and the other just the solid, which is defined by means of a nonzero solid-concentration field. The boundary condition at the fluid-structure interface is applied through a penalty force. One of the advantages is that each mesh can be used by a different finite element.

2.7. Summary

In this chapter, an overview of the background information and theory on which the current research is based was given. In the first part, the general hydrodynamics of floating bodies, including their stability, their hydrodynamic properties, their unforced response and their behaviour to incoming waves were presented. In the second, the different types of free surface regular waves, their measure of nonlinearity, their effects on the loading, and the main wave theories used to describe them were addressed. During the third part, a brief background regarding the state-of-the-art of the wave-structure interaction numerical simulation was given.

<div style="text-align: right; font-size: 3em; font-weight: bold;">3</div>

NUMERICAL TOOLS

3.1. INTRODUCTION

This chapter presents the numerical tools used throughout this thesis to model the free surface flows and fluid-structure interaction. The first numerical framework is the open-source CFD-software OpenFOAM® v1606+ version, based on the fully nonlinear Navier-Stokes/VOF solver and coupled with the toolbox waves2Foam. This is described in Section 3.2, including its coupling to a 6DOF dynamic motion solver. The second numerical tool used is based on potential flow theory and is introduced in Section 3.3. This one is applied within the frequency-domain diffraction solver Wadam framework. A schematic overview of the structure of this chapter is depicted in Figure 3.1.
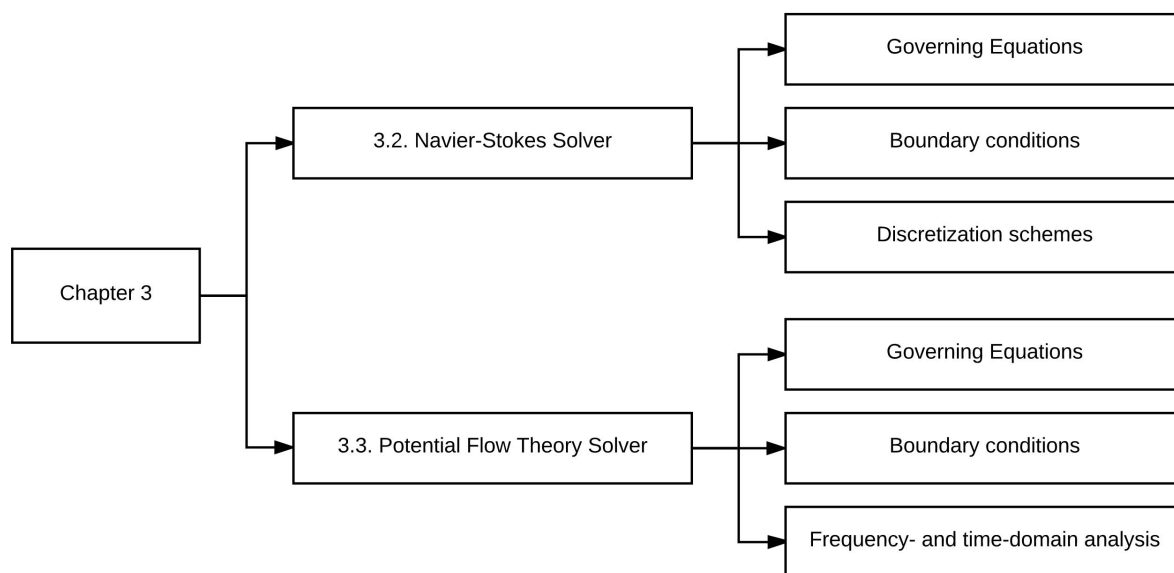
Figure 3.1: Scheme of Chapter 3 structure.

3.2. NAVIER-STOKES SOLVER

Fluid-structure interaction can be accurately described by the Navier-Stokes equations combined with the conservation of mass equation. The numerical solution has to be found using a Computational Fluid Dynamics

(CFD) model, because an analytical solution for this flow problem does not exist. A very well-known open-source library for engineering applications is OpenFOAM®. Firstly, because of the discretisation method it applies, which ensures the conservation properties, and, secondly, because of the available schemes that direct the solution towards stability, even for cases where convergence is not that trivial to be achieved, as it is the case with coarse and unstructured meshes. Throughout this work the interFoam solver, coupled to the waves2Foam toolbox, is used. This solver applies finite volume discretisation on collocated grids to solve the two-phase equations of the flow. When the problem involves the motion of the structure, the waveDyMFoam solver, based on the interDyMFoam solver, is applied. In this section, the governing equations for the interFoam solver, the needed boundary conditions, and the choice of the different discretisation schemes, are presented.

3.2.1. GOVERNING EQUATIONS

The governing equations for an incompressible Newtonian fluid are based on the continuity and the momentum conservation equation, which expressed in their differential form, yield:

$$\nabla \cdot \mathbf{u} = 0; \tag{3.1}$$

$$\rho \frac{Du}{Dt} = \frac{\partial \rho \mathbf{u}}{\partial t} + \rho \mathbf{u} \cdot \nabla \mathbf{u} = -\nabla p^* - \mathbf{gx} \nabla \rho + \rho \mu \nabla^2 \mathbf{u}, \tag{3.2}$$

where $\nabla = (\partial_x, \partial_y, \partial_z)$ is the three-dimensional gradient operator, $\mathbf{u}$ the velocity field in Cartesian coordinates, $\mathbf{g}$ the gravitational constant, and p^* the excess pressure, equal to $p^* = p + \rho g z$. The local density ρ and the viscosity μ, defined in terms of the water and air volume fraction α (subscripts a and w, respectively), are formulated as:

$$\rho = \alpha \rho_w + \rho_a (1 - \alpha) \tag{3.3}$$

$$\mu = \alpha \mu_w + \mu_a (1 - \alpha). \tag{3.4}$$

To solve these equations, OpenFOAM® uses the volume of fluid (VOF) method, developed by Hirt & Nichols (1981), in which the scalar function $\alpha \in [0, 1]$, represents the phase of the fluid in each cell (0 is air, and 1 is water). This field is advanced in time once the velocity is known, following the modified transport equation, formulated by Rusche (2002):

$$\frac{\partial \alpha}{\partial t} + \nabla \cdot \mathbf{u} \alpha + \nabla \cdot \mathbf{u}_r \alpha (1 - \alpha) = 0. \tag{3.5}$$

The additional convective term keeps the interface sharp, even with the step-like nature of α. It is governed by $\mathbf{u}_r$, an artificial velocity field normal to and pointing towards the free surface. Its magnitude is proportional to the instantaneous velocity. This term exists if $0 < \alpha < 1$, i.e. at the vicinity of the interface, and if it were not used, the air-water interface would be highly smeared. To ensure boundedness of the solution, a multidimensional flux limited scheme, namely the Multidimensional Universal Limited for Explicit Solution (MULES), is used. It should be noted that despite the existence of the artificial compression term, the free surface can be smeared over a number of cells. This implies that there is not a specific location where the interface exists. For the cases in which the air-water interface is needed, mainly for visualisation purposes, the iso-contour with $\alpha = 0.5$ is chosen, so that the level set between air and water is defined as:

$$L_{air-water}(\alpha) = \{\mathbf{x} | \alpha(\mathbf{x}) = 0.5\}. \tag{3.6}$$

For the free-surface location, the wave gauge functionality, included in the waves2Foam package, is applied. One or more wave gauges are placed at certain positions in the numerical domain, so that the free surface elevation ζ, relative to the still water level, is found as:

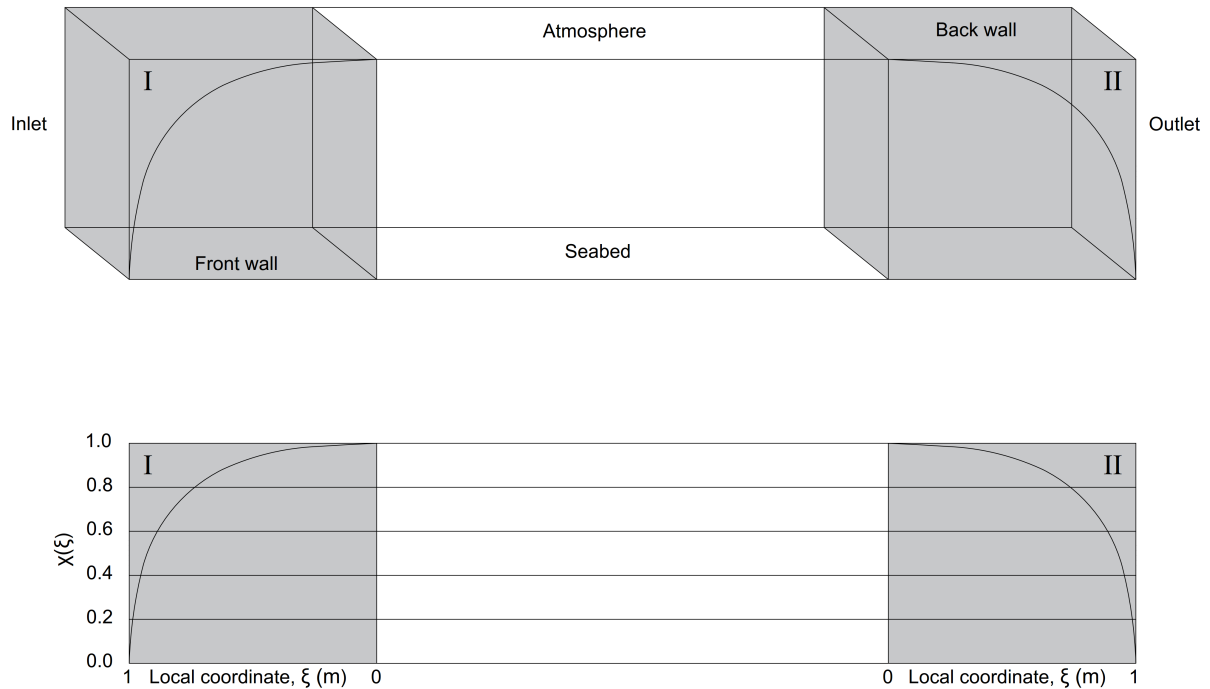$$\zeta = \int_{x_0}^{x_1} \alpha \, dz - d, \tag{3.7}$$

Figure 3.2: Top: schematic overview of the boundary conditions implemented at the computational domain in the Navier-Stokes/VOF solver, where I and II correspond to the relaxation zones. Bottom: representation of the spatial weighting factor $\xi(\epsilon)$, as a function of the local coordinate ϵ, at the relaxation zones.

where x_0 and x_1 are the user defined start and end points in the vertical line over which the α field is integrated, d is the initial position of the still water level. This procedure is the one used in the current work.

3.2.2. BOUNDARY CONDITIONS

The integral form of the incompressible Navier-Stokes equations, combined with the continuity equation, is solved for every point of the numerical domain. Boundary conditions are imposed to all the surfaces in the numerical domain, including the ones from the structure if present. These conditions inherently depend on the type of problem to be solved.

The velocity and the α field boundary conditions at the inlet and outlet surfaces are imposed by the wave theory to be applied. In the current work, this is either a stream function or a potential current with zero velocity. At the seabed, a *slip* condition is imposed, what directly implies that the viscous boundary layer effects, such as the shear stresses, are neglected. At the front and back walls a *slip* condition is equally applied in the case of dealing with a three-dimensional case. If a two-dimensional case is treated, the boundary condition at these walls is set as *empty*. This implies that for the planes that are normal to the third dimension, no solution is required. At the upper wall boundary, the total pressure is set equal to zero, and an *atmospheric* boundary condition is applied for α and the velocity. This implies that air and water are allowed to leave the numerical domain, while only air is allowed to flow back in. A schematic view of the domain, including the relaxation zones and the boundary conditions, is depicted in Figure 3.2.

RELAXATION ZONES

The open-source wave generation and absorption toolbox waves2Foam, recently developed by Jacobsen et al. (2012), allows for the implementation of relaxation zones, to avoid wave reflection from the outlet boundary and also to prevent internally reflected waves. These can have an arbitrary shape, although for the cases treated here

the shape is always rectangular. At these relaxation zones, the velocity $\mathbf{u}$ and the α fields are updated at every time step according to:

$$\phi = \xi\phi_{target} + (1-\xi)\phi_{com},$$ (3.8)

where ϕ_{target} is the target solution in time and space given by one of the available wave theories in waves2Foam, or by the fully nonlinear potential flow solver, OceanWave3D, developed by Paulsen et al. (2014b). The numerically computed quantity ϕ_{com} is obtained by solving the governing equations. $\xi(\epsilon)$ is the weighting factor for each of the two solutions. It depends on the local coordinate $\epsilon \in [0;1]$, being zero at the outer part of the relaxation zone and one at the inner edge. It is given by:

$$\xi(\epsilon) = 1 - \frac{\exp(\xi^\beta) - 1}{\exp(1) - 1},$$ (3.9)

where β is the shape factor. In the present work the default value, $\beta = 3.5$, is used.

3.2.3. DISCRETISATION

To solve the hydrodynamic problem, the partial differential equations have to be replaced by difference equations in the flow domain, so a process of discretisation has to be applied. Firstly, a domain discretisation method is needed, followed by the partial differential equation terms, both spatial and temporal, discretisation.

DOMAIN DISCRETISATION

There are four grid-based discretisation techniques widely used within the CFD community: the finite difference method, the finite element method, the finite volume method and the spectral element method. OpenFOAM® uses the finite volume method, based on the application of the conservation principles applied to a finite region in space known as control-volume. Here the discretisation is applied to an integral formulation of the equation and is based on balancing fluxes between control-volumes. Hence, the flow characteristics are directly used. The advantages of this method over the others are, firstly, the local and global mass conservation satisfaction and, second, the treatment of boundary conditions for complex geometry in a less cumbersome way.

TEMPORAL AND SPATIAL DISCRETISATION SCHEMES

Differential schemes are used for the numerical approximation of the terms in the governing equations 3.1, 3.2 and 3.5. One of the major challenges in the field is the treatment of the advective term of the Navier-Stokes equation (Eq. 3.2). Several options exist: the central difference scheme, which is not usually used in CFD applications, the upwind schemes and the Total Diminishing Variation (TVD) schemes. Based on the conclusions presented in Bruinsma (2016), after comparing a first-order upwind and a second-order MUSCL scheme (TVD), the former is used throughout the current numerical analysis.
An overview of the discretisation schemes used in this work is given in Table 3.1.

3.2.4. COUPLING OF NAVIER-STOKES-6DOF SOLVER. INTERDYMFOAM/WAVEDYMFOAM

If the fluid-structure interaction problem implies the motion in any of the six degrees of freedom of the structure within the numerical domain, the 6DOF solver interDyMFoam is used. Moreover, if the body is subjected to waves, interDyMFoam is coupled to the waveDyMFoam solver, provided by the wave2Foam toolbox. The total force and moments exerted at the *COG* of the body may come from the action of the fluid, or by other external forces, such as the gravity force, or the forces and moments coming from restraints, such as the mooring lines. The fluid forces $\mathbf{F}_k$ and moments $\mathbf{M}_k$ for each degree of freedom k of the body are calculated by means of integrating the pressures on the body surface S_{oB} as:

$$\begin{bmatrix} \mathbf{F}_k \\ \mathbf{M}_k \end{bmatrix} = \int_{S_{oB}} p \begin{bmatrix} \mathbf{n} \\ \mathbf{r} \times \mathbf{n} \end{bmatrix} dS_{oB}.$$ (3.10)

Table 3.1: Numerical schemes used throughout this work.

	Term	Discretisation
Spatial domain		Finite Volume (FV) Method
Temporal derivative	$\dfrac{d}{dt}$	Euler. Second-order
Gradient	$(\nabla \mathbf{u}, \nabla \alpha)$	Gauss linear. First-order
Divergence	$\nabla \cdot (\rho \phi \mathbf{u})$	Gauss upwind. First-order
	$\nabla \cdot (\phi \alpha)$	Gauss upwind. First-order
	$\nabla \cdot (\rho \phi_{rb} \alpha)$	Gauss interface compression. First-order
Laplacian	∇^2	Gauss linear corrected. First-order

The pressure is derived from Equation 3.2, from where four unknowns remain, namely the pressure itself and the three components of velocity $\mathbf{u}$. However, just three equations are available: the momentum equation for the three velocity components and the continuity equation. The latter, for an incompressible fluid, does not present the pressure term. So, to be able to use the mass conservation equation, a semi-discretisation of the momentum equation is made, or in other words, only the derivatives in time are discretised, while the spatial derivatives are kept in their partial differential form. By taking the divergence of the momentum equation and using the continuity equation, the Poisson equation for pressure ($\Delta p = f(U, \nabla p)$), can be used. The equations are solved based on the so-called pressure-momentum coupling algorithms. The most widespread ones are the SIMPLE, PISO and PIMPLE algorithms. As a rule of thumb, the first one is used for steady-state analyses, the second one for transient calculations, and is limited by the time step, and the third one (SIMPLE+PISO) is a combination of the former and allows for bigger time-steps. A thorough explanation of these algorithms can be found in Ferziger & Perić (2012) and Moukalled et al. (2015). In the current work, the PIMPLE algorithm is used, comprised by the following steps:

- *Momentum predictor*: the momentum equation is solved, based on a non-exact pressure gradient.

- *Pressure solution*: based on the found velocities the solution of the discretised Poisson equation gives an estimation of the new pressure field.

- *Velocity correction*: the velocity is corrected explicitly with the new pressure field.

To ensure numerical stability the maximum the Courant-Friedrichs-Lewy (CFL) condition has to be fulfilled, as:

$$Co = \frac{|u_i| \cdot \Delta t}{\Delta x_i} \leq 1, \tag{3.11}$$

where $|u_i|$ is the magnitude of the velocity in i-direction, Δt the time step, and Δx_i the cell size in the i-direction. Throughout this work, the maximum Courant number Co_{max} is set to 0.25, unless otherwise specified. The time step is chosen to be adjustable. The algorithm, within one time step, looks for the equilibrium. Once the velocities are obtained, the acceleration is calculated. Stability can be ensured using two different approaches: the *under-relaxation* method and the *predictor-corrector* method. The choice to use one or the other for the different cases studied throughout this work is based on the thorough analysis of both methods performance completed in Bruinsma (2016).

The *under-relaxation method* applies a relaxation factor f_a to the computed acceleration from the forces and moments, as follows:

$$a_i^* = f_a a_i + (1 - f_a) a_{i-1}^*, \tag{3.12}$$

where a_i^* is the under-relaxed acceleration of the *COG* at the instantaneous time step. In this case, the acceleration is treated as a total variation diminishing (TVD) property. It increases the stability, although a diffusive term is introduced, which may affect the convergence rate of the solution. Unless otherwise specified, an acceleration-relaxation factor of 0.5 is used for the validation cases presented in Chapter 4.
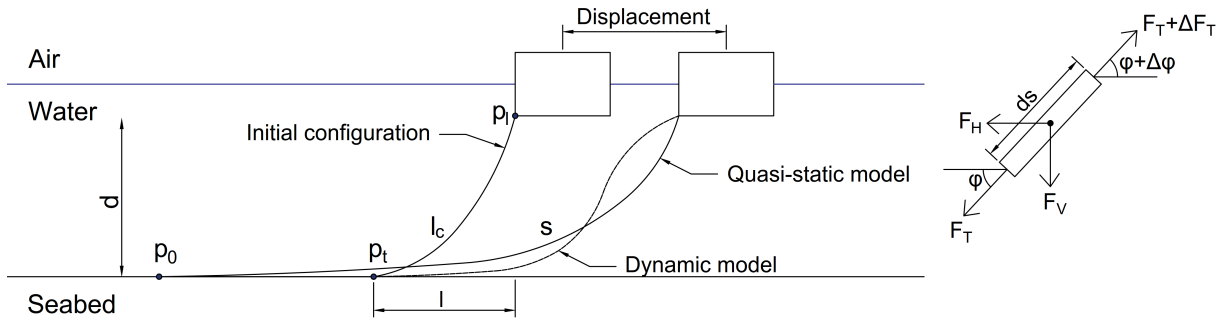
Figure 3.3: Left: representation of the quasi-static approach of modelling the mooring lines behaviour with respect to the dynamic model behaviour. Right: decomposition of the forces acting on the mooring line.

The *predictor-corrector method* implies an initial step of predicting the displacement of the body, based on the forces acting on it, and, consequently, the correcting steps, during which the pressure field is updated, and the corrected displacement of the body is applied. In order to achieve a smooth convergence, the pressure is relaxed with the relaxation factor f_p, as:

$$p_i^* = f_p p_i + (1 - f_p) p_{i-1}^*, \tag{3.13}$$

where p_i^* is the under-relaxed pressure at the instantaneous time step. A constant under-relaxation factor f_p, equal to 0.5, is applied during all the iteration loops, except for the last one, in which f_p is set to one, to ensure time consistency.

DYNAMIC MESHING

Once the motion of the rigid body is determined, it is necessary to move the boundary as well as the mesh surrounding it to maintain the high quality of the mesh. This can be done using the *dynamicFvMesh* solver. Two different approaches for the mesh adjustment may be used. The first one involves a solver that allows for topological changes, which implies that the number of points, faces, and cells in the mesh can vary to comply with the motion of the body. The second one entails the dynamic mesh to be based just on pure deformation, so that the number of faces, points and cells, does not change, and therefore no topological changes are allowed. In the current case the *sixDoFRigidBodyMotion* solver, within the *dynamicMotionSolverFvMesh*, which corresponds to the second case of dynamic mesh solvers, is applied. The area in which the cells are allowed to deform is known as the outer area and is defined by an outer radius. Another smaller area, in which the initial mesh orthogonality is preserved, is defined by an inner radius. There the cells translate and rotate with the moving wall boundary of the body.
Besides the area where the mesh is allowed to deform, the version of OpenFOAM® used through this research work supports run-time selectable integrators for the mesh motion: the explicit symplectic solver, the implicit Crank-Nicolson and implicit Newmark methods, all of which are 2$^{\text{nd}}$-order in time. The one applied here is the standard Newmark implicit solver for the time integration of the mesh motion. Regarding the mesh deformation, the spherical linear interpolation (Slerp) function is used, as opposed to other methods applied in earlier versions of OpenFOAM®, which were based on conventional elliptic equation solvers. Within the Slerp interpolation, the translations and rotations are expressed by septentrions and quaternions. Good insight on this topic is given in the works by Samareh (2002), who performed a mesh deformation method using quaternions to preserve mesh orthogonality around boundaries in two-dimensional cases, and by Maruyama et al. (2012).

RESTRAINTS

The implementation of restraints for moving boundary surfaces was done by Niels G. Jacobsen (Researcher/ advisor at Deltares) for the OpenFOAM®-v1606+ version, and is publicly available. The two restraints implemented are a linear spring and a simple catenary type mooring line. The method to obtain the forces for both of them are described in the following.
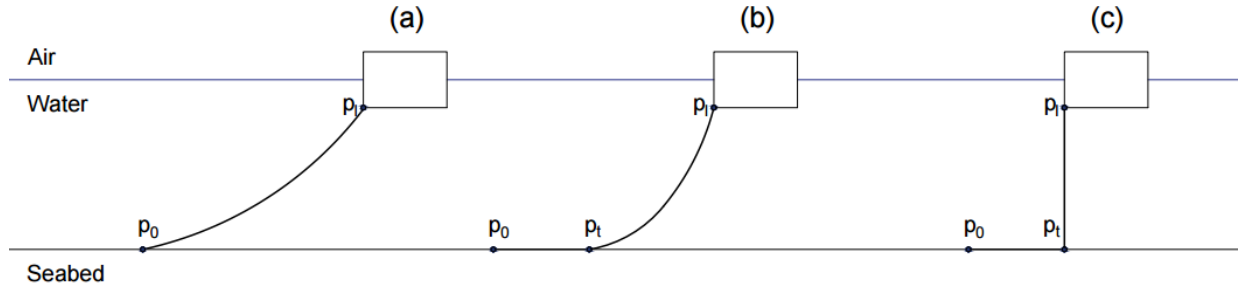
Figure 3.4: Different configurations of the mooring system based on its implementation in OpenFOAM®.

Linear Spring. The linear spring implementation is straightforward, based on a stiffness k and a rest length l_r, i.e. the length for which the spring force is zero. No damping is taken into account. The force exerted by the linear spring is given by:

$$\mathbf{F_0} = -k \frac{\mathbf{r}}{\|\mathbf{r}\|_2} (\|\mathbf{r}\|_2 - l_r) = -\mathbf{F_1}, \tag{3.14}$$

where $\mathbf{F_0}$ and $\mathbf{F_1}$ are the forces at $\mathbf{p}_0$ and $\mathbf{p}_1$, respectively, and $r = \mathbf{p}_0 - \mathbf{p}_1$.

Mooring Line. The behaviour of the mooring lines can be modelled statically, quasi-statically or dynamically. Static models consider constant loads only, such as gravity, buoyancy or non-time varying current and wind. Equilibrium is therefore determined between the constant environmental loads and the restoring force of the mooring lines. The quasi-static approach assumes that the motion of the system is uniform and linear between two static positions during a given time step, or in other words, at every time step, the system reaches a new static equilibrium. Any dynamic effects on the mooring system, such as hydrodynamic and inertial forces on the line, are ignored. In the dynamic models, the dynamics of the mooring lines are based on Newton's second law, where the resulting motions are due to forces acting on the body. A thorough review of the different modelling approaches can be found in Penalba et al. (2017). The general equations of motion for the mooring system are solved using the explicit integration method described in Tedesco et al. (1999), based on a central difference approximation. The three possible configurations of the mooring system are: simple state, resting state and hanging state.

In the *simple state*, represented in Figure 3.4, (a), the mooring line is completely suspended, implying that the anchor point $\mathbf{p}_0$ is the same as the touchdown point $\mathbf{p}_t$. The state of the line can be ordinary, or length exceeded. The first one is based on the catenary equations between two attachment points, as explained in Krenk (2001). In this case, the distance between the attachment points is less than the unstretched length of the line l_c. The horizontal component F_H and the vertical component F_V of the restoring force are given, respectively, as:

$$F_H = \frac{s^2 - d^2}{2d} m_{sub} g \quad \text{and} \tag{3.15}$$

$$F_V = m_{sub} g s, \tag{3.16}$$

where s is the instantaneous length of the mooring line, equal to l_c in this case, d the vertical distance and m_{sub} the submerged mass per length of the mooring line. The total force can be straightforwardly obtained.

The second possible state is the *resting state*, represented in Figure 3.4, (b). In this case, the distance in the x-direction between the structure and the anchor point is sufficiently small to have part of the line resting on the

seabed. The suspended part behaves as a catenary line. To compute the restoring force acting on the body, the touchdown point is needed, so that the instantaneous length of the suspended part of the line is known. Once this length is known, the forces can be straightforwardly obtained using Equations 3.15 and 3.16.

The third possibility is defined as the *hanging state*, represented in Figure 3.4, (c). In this case, the floating object is so close to the anchor point that the piecewise linear configuration of the mooring line is shorter than the length of the mooring line itself. This case takes place if the angle between the attachment point and the horizontal is higher than 88°, and consequently, just a vertical force is acting.

3.3. Potential Flow Theory Solver

Potential flow solvers, also known as diffraction solvers, are numerical tools that predict wave-induced motions and loads on large volume structures at zero velocity. In the next sections the governing equations, based on the main assumptions of first-and second-order potential flow theory, are presented. Furthermore, the main parameters concerning the frequency- and time-domain analyses are addressed.

3.3.1. Governing equations. Boundary value problem

The first assumption of potential flow theory is that the fluid is inviscid. Kelvin's circulation theorem states that a flow that is irrotational in an inviscid flow remains irrotational. This implies that vorticity ω is zero everywhere in the fluid, and by definition:

$$\omega \overset{\text{def}}{=} \nabla \times \mathbf{u}(\mathbf{x}, t) = 0, \tag{3.17}$$

where $\nabla \times$ is the three-dimensional rotational operator and $\mathbf{u}(\mathbf{x}, t) = \mathbf{u}(x, y, z, t)$ the velocity field in Cartesian coordinates, also dependent on time. The velocity field $\mathbf{u}$ can thus be defined by means of the so-called velocity potential $\phi(\mathbf{x}, t)$ as:

$$\nabla \phi = \mathbf{u} = \left(\frac{\partial \phi}{\partial x}, \frac{\partial \phi}{\partial y}, \frac{\partial \phi}{\partial z} \right). \tag{3.18}$$

The third characteristic of potential flow is the incompressibility. If the continuity equation for incompressible flows is invoked, the velocity potential has to satisfy Laplace's Equation 3.19 in the fluid domain Ω. This is the governing equation for potential flow theory, and is expressed as:

$$\nabla^2 \phi(\mathbf{x}, t) = 0. \tag{3.19}$$

This reduces the number of unknowns from four, namely the three velocity components and the pressure, to just two: the velocity potential ϕ and the pressure p. The potential can be solved using several methods; one of the most widespread is the boundary element method (BEM) called panel method. If the irrotational and inviscid Navier-Stokes equations are combined with the continuity equation, the well-known Euler equation is obtained. If it is expressed with respect to the velocity potential ϕ, and the vertical component is taken, Bernoulli's equation, depending on p yields:

$$p - p_a = -\rho \frac{\partial \phi}{\partial t} - \rho \frac{1}{2} |\Delta \phi^2| - \rho g z. \tag{3.20}$$

The forces derive from the integration of p around the body surface, as defined in Equation 3.10.

3.3.2. Boundary conditions

To solve these equations, the boundary conditions have to be set, analogous to the boundary conditions imposed when solving the Navier-Stokes equations. These are enumerated hereafter and are based on the fluid domain presented in Figure 3.5.
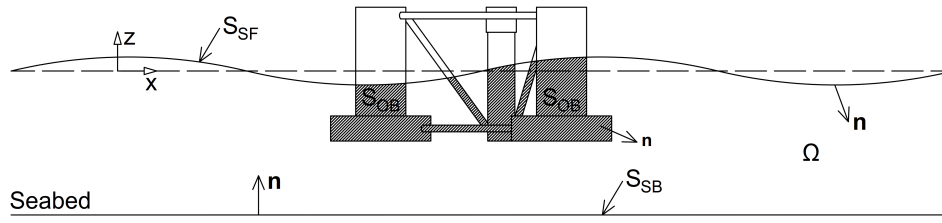
Figure 3.5: Overview of the fluid domain of the Boundary Value Problem (BVP).

- Sea-bottom kinematic condition, which denotes the condition of impermeability at the bottom S_B.

$$\frac{\partial \phi}{\partial n} = 0 \qquad \text{on} \quad S_B \tag{3.21}$$

- Body kinematic condition, which implies the impermeability on the body surface S_{oB}.

$$\frac{\partial \phi}{\partial n} = \mathbf{V}_B \cdot \mathbf{n} \qquad \text{on} \quad S_{oB}, \tag{3.22}$$

where $\mathbf{V_B}$ is the body velocity and $\mathbf{n} = (n_1, n_2, n_3)$ and $\mathbf{x} \times \mathbf{n} = (n_4, n_5, n_6)$.

- Free surface kinematic condition, which indicates that the particles at the free surface ζ remain there.

$$\frac{D(z - \zeta)}{Dt} = 0 \longrightarrow \frac{\partial \phi}{\partial z} = \frac{\partial \zeta}{\partial t} + \frac{\partial \phi}{\partial x}\frac{\partial \zeta}{\partial x} + \frac{\partial \phi}{\partial y}\frac{\partial \zeta}{\partial y} \qquad \text{at } z = \zeta(x, y, t) \tag{3.23}$$

- Free surface dynamic condition, which denotes that the pressure at the free surface S_{FS} is equal to the atmospheric pressure.

$$g\zeta + \frac{\partial \phi}{\partial t} + \frac{1}{2}|\nabla \phi|^2 = 0 \qquad \text{at } z = \zeta(x, y, t) \tag{3.24}$$

- Far-field (or radiation) condition, which implies the outgoing nature of waves.

The governing equation and the boundary conditions define the boundary value problem (BVP) to be solved. It can be inferred that the problem is nonlinear due to the two conditions at the free surface. Fully nonlinear potential flow solvers are usually used to solve the problem without getting rid of these nonlinearities. However, the first- and second-order potential flow solver presented here get rid of the second and third order nonlinearities, respectively, by means of a perturbation method.

3.3.3. FIRST-ORDER POTENTIAL FLOW THEORY

The first-order potential flow solution is found by solving the first-order velocity potential $\Phi^{(1)}$. The fluid pressure and the velocity of fluid particles on the free surface are linearised using a perturbation approach, the full nonlinear velocity potential ϕ and the free surface elevation ζ can be expressed as:

$$\phi = \Phi^{(1)}\epsilon + \Phi^{(2)}\epsilon^2 + \Phi^{(3)}\epsilon^3 + ... \tag{3.25}$$

$$\zeta = \zeta_1\epsilon + \zeta_2\epsilon^2 + \zeta_3\epsilon^3 + ... \tag{3.26}$$

where $\epsilon = kA$ is the nonlinearity of the wave, as presented in Chapter 2, Section 2.4. If ϵ is small, the higher order terms (ϵ^2, ϵ^3...) can be eliminated. If just the terms $O(1)$ from Equation 3.25 are retained and plugged into the governing Equation 3.19, and the boundary conditions are Taylor expanded around the mean boundary configuration, the linearised kinematic free surface condition at $z = 0$ yields:

$$-\frac{\partial \zeta}{\partial t} + \frac{\partial \phi}{\partial z} = 0. \tag{3.27}$$

The first-order linear solution implies that the motions have zero mean value and that they oscillate with the frequency of the incident waves. If Equation 3.25 is invoked, and the terms of higher order than one are neglected, the harmonic time dependence of the total first-order potential, $\Phi^{(1)}$, allows the definition of a complex velocity potential ϕ_1, related to $\Phi^{(1)}$ by:

$$\Phi^{(1)}(\mathbf{x}, t) = \text{Re}(\phi_1(x, y, z) \exp(i\omega t)), \tag{3.28}$$

where Re denotes the real part and ω is the frequency of the incident wave. Here the time and spatial dependencies are separated. Furthermore, the linearity of the problem allows solving the problem independently as two subproblems, since the principle of superposition applies. The first one deals with the forces and moments on the body when the structure is subjected to incident waves, but restrained from moving. This subproblem, known as the diffraction problem, is related to the wave excitation loads, namely the Froude-Krylov and the diffraction forces and moments. The potentials attached to this problem are the incident waves potential ϕ_I and the diffraction potential ϕ_S, respectively. The second subproblem, known as the radiation problem, is related to the forces and moments on the body when the structure is forced to oscillate at a certain frequency in any of its rigid-body modes, with no incident waves. The potential of this subproblem is known as the radiation potential ϕ_R. From the latter, the added mass, damping and restoring terms can be obtained. A detailed derivation of this problem can be found in Faltinsen (1990). The total potential yields:

$$\phi = \phi_I + \phi_S + \phi_R = \phi_D + \phi_R, \tag{3.29}$$

where ϕ_D is known as the diffraction potential. The spatial potential for the diffraction problem satisfies the impermeability condition, with **n** as the generalised normal vector, according to:

$$\frac{\partial \phi_S}{\partial \mathbf{n}} = -\frac{\partial \phi_I}{\partial \mathbf{n}} \longrightarrow \frac{\partial(\phi_I + \phi_S)}{\partial \mathbf{n}} = 0. \tag{3.30}$$

The radiation potential ϕ_R can be obtained as the linear combination of the components corresponding to the six degrees of freedom k as:

$$\phi_R = \text{Re}\left(\sum_{k=1}^{6} \dot{\eta}_k \phi_k\right), \tag{3.31}$$

where $\dot{\eta}_k$ is the velocity in mode k and ϕ_k the complex spatial velocity potential for the body oscillating with unit amplitude of motion in mode k. Since the three potentials related to the diffraction and radiation problems are known, the total excitation forces on the body can be found by means of integrating the dynamic pressure along the mean wetted surface of the body, which expressed in terms of the potentials, yields:

$$F_{exc,k} = -\int_{SoB} \rho \frac{\partial \phi_0}{\partial t} n_k \, dS - \int_{SoB} \rho \frac{\partial \phi_D}{\partial t} n_k \, dS - \int_{SoB} \rho \frac{\partial \phi_R}{\partial t} n_k \, dS \qquad k = 1...6, \tag{3.32}$$

where the first two terms of the right-hand side correspond to the waves excitation loads, Froude-Krylov and diffraction loads, respectively. The added mass and damping components derived from the radiation problem can be directly found from the radiation term in Equation 3.32, since the added mass loads are proportional to the acceleration, whereas the damping ones are proportional to the velocity. The hydrostatic restoring terms are connected with the variation of the buoyancy due to the body motions. Note that in the linear solution presented here, both the free-surface condition and the body boundary condition are satisfied at the mean position of the free-surface and the submerged hull surface, respectively.

3.3.4. SECOND-ORDER POTENTIAL FLOW THEORY

As the incident waves become steeper and therefore kA increases, also higher order terms must be retained for a suitable estimate of the loads and motions. Therefore, the second-order terms from the perturbation approach, Equation 3.25, are included to examine these effects. This way the boundary conditions are solved with a smaller error. In particular, the impermeability of the body at its instantaneous positions of the body is applied. Furthermore, the pressure is enforced to be the atmospheric one at the instantaneous free surface, and the normal fluid velocity at the free surface is closer to the free-surface normal velocity. Hence, by applying the second-order potential theory, all the terms in the velocity potential, fluid pressure and wave loads are assumed to be either linear with the wave amplitude or proportional to the square of the wave amplitude. The second-order potential flow theory solution results in mean forces and forces oscillating with difference- and sum-frequency oscillations, besides the linear solution. The mean forces yield a mean drift. The difference- and sum-frequency effects derive from the interaction between different frequencies components. Their interaction results in an excitation outside the waves excitation ranges. The full second-order potential can thus be expressed as:

$$\Phi^{(2)}(\mathbf{x}, t) = Re \sum_i \sum_j \phi_{i,j}^+(\mathbf{x}) \exp^{i(\omega_i + \omega_j)t} + \phi_{i,j}^-(\mathbf{x}) \exp^{i(\omega_i - \omega_j)t}. \tag{3.33}$$

The problem is still approximated, but with a smaller error ($O(\epsilon^3)$). It presents sum-frequency components, denoted as $\phi_{i,j}^+$, and difference-frequency, or slow-varying, components denoted as $\phi_{i,j}^-$, which can be solved separately. The latter are obtained by integrating the pressure from the difference-frequency potential. For a given sea state with N wave components of frequency ω_i, amplitude A_i and phase ϵ_i, the slowly-varying forces and moments F_i^{SV} are defined by:

$$F_i^{SV} = \sum_{i=1}^N \sum_{j=1}^N A_i A_j \left[T_{ij}^{ic} \cos(\omega_i - \omega_j)t + (\epsilon_i - \epsilon_j) + T_{ij}^{is} \sin(\omega_i - \omega_j)t + (\epsilon_i - \epsilon_j) \right], \tag{3.34}$$

where $i, j = 1 : 6$ and T_{ij}^{ic} and T_{ij}^{is} are the transfer functions for the difference-frequency forces. These can be conveniently simplified by means of Newman's approximation, as:

$$T_{i,j}^{ic} = T_{j,i}^{ic} = 0.5(T_{i,i}^{ic} + T_{j,j}^{ic}); \tag{3.35}$$

$$T_{i,j}^{is} = -T_{j,i}^{is} = 0. \tag{3.36}$$

Both of them can be computed from the first-order solution and therefore there is no need to calculate $\Phi^{(2)}$. This approximation is applicable in the following two cases: if the natural frequency of the body is very low, so that the interest lies in regions where $\omega_j - \omega_i$ is small, or if $T_{i,j}^{ic}$ and $T_{j,i}^{ic}$ do not change significantly with frequency. Slowly-varying drift loads are important for semisubmersible structures and the mooring lines. A detailed analysis may be found in Faltinsen (1990).

The sum-frequency terms come from the square velocity component in Bernoulli's Equation 3.20. An effect deriving from these is the springing, which is a steady-state resonant elastic motion of the platform in the vertical plane. This phenomenon is relevant to be considered on TLP structures mainly, due to their typical lower natural heave period.

3.3.5. VISCOUS FORCES AND DAMPING

For cylindrical structures with small diameters, viscous forces and flow separation have to be taken into account when severe sea states with long waves and high wave heights take place. Then, the potential flow solution for large volume bodies might be combined with Morison's equation.

MORISON'S EQUATION

As already presented in Section 2.5, Chapter 2, Morison's equation is used to calculate wave loads on circular cylindrical structural members when viscous forces matter and wave scattering (diffraction) is secondary. This is the case for slender structures ($D < \lambda/5$), since in that case the diffraction effect and radiation damping become negligible. The inline force per unit length f_N acting on a moving cylinder can be expressed as:

$$f_N(t) = \rho \pi \frac{D^2}{4} \dot{u} + \rho C_a \pi \frac{D^2}{4} (\dot{u} - \dot{v}) + \frac{1}{2} \rho C_D D (u - v)|(u - v)|, \tag{3.37}$$

where u is the transverse wave particle velocity, v the local transverse body velocity, C_D the drag coefficient and C_a the added mass coefficient, equal to $(C_M - 1)$, where C_M is the inertia coefficient. The first term in Morison's equation represents the Froude-Krylov force, the second one the added mass force and the third one the viscous drag forces.

In general, C_M and C_D have to be estimated empirically, since they depend on the Keulegan-Carpenter number KC and Reynold's number Re, as presented in Sumer & Fredsøe (2006). These non-dimensional numbers are defined as:

$$Re = \frac{uD}{\nu} \quad \text{and} \tag{3.38}$$

$$KC = \frac{U_M T}{D}, \tag{3.39}$$

where D is the characteristic length, which in this case it is the cylinder diameter, U_M the maximum fluid velocity and ν the kinematic viscosity, equal to 10^{-6} m^2/s. The drag and inertia coefficients dependence on Re and C_M is depicted in Figure 3.6, respectively, for a smooth cylinder.
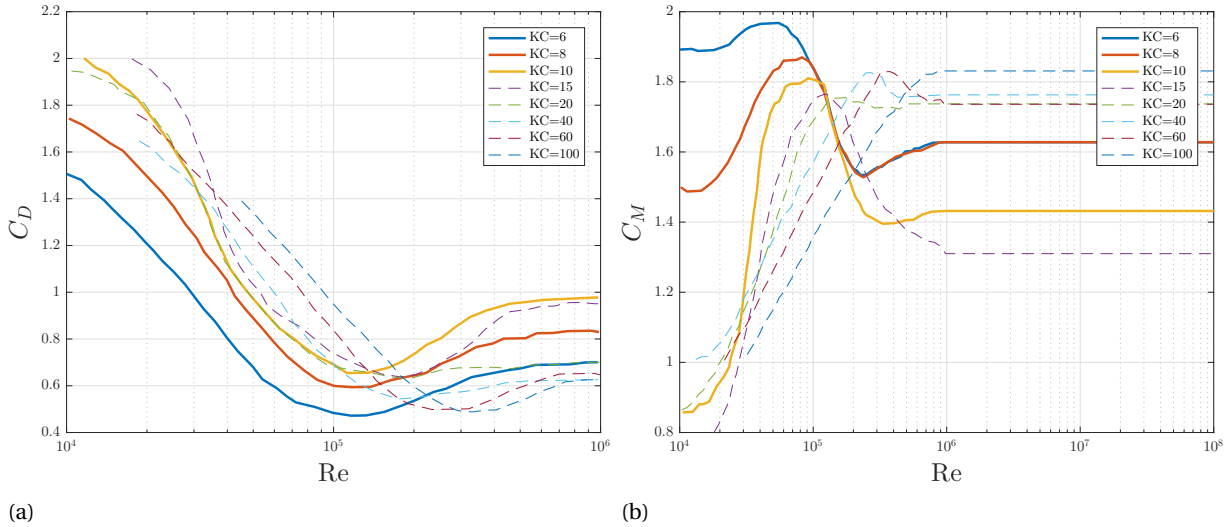

Figure 3.6: Drag (a) and inertia (b) coefficients dependence on Re and KC for a smooth cylinder. Modified from Sumer & Fredsøe (2006).

3.3.6. FREQUENCY-DOMAIN ANALYSIS

The motions of a floating rigid structure in the time-domain are described by Equation 2.4, presented in Chapter 2. In the case of considering a linear analysis, the problem can be stated in the frequency domain, which implies a lower computational time. The equations of motion of a rigid floating body with 6DOF in a regular wave can be written in the frequency domain as:

$$-\omega^2 \left[\mathbf{M} + \mathbf{A}_\infty(\omega)\right] \tilde{\mathbf{x}} + (i\omega \mathbf{A}(\omega) + \mathbf{B}(\omega)) i\omega \tilde{\mathbf{x}} + [\mathbf{C} + \mathbf{K}] \tilde{\mathbf{x}} = \tilde{\mathbf{F}}_{exc}(\omega), \tag{3.40}$$

where the superscript *tilde* denotes the variable in the frequency domain and A_∞ is the infinite-frequency limit added mass constant value. The added mass matrix and the damping matrix coefficients, and the excitation forces depend on the frequency. Note that no second-order forces are included. In order to obtain the frequency-dependent terms, the tool Wadam (HydroD), based on the WAMIT software, developed by Lee (1995), is used. It evaluates the unsteady hydrodynamic pressure, loads and motions of the body, as well as the induced pressure and velocity in the fluid domain. The free-surface and body-boundary conditions are linearised as already presented, using a perturbation method. Since the flow is assumed to be potential, it is free of separation or lifting effects. A harmonic time dependence is adopted.

Within this tool, the radiation-diffraction problem is solved using a 3D panel method, with the so-called source-sink technique. The main idea behind is that the wetted body surface is divided into quadrilateral panels. The unknowns are assumed to be constant over each panel. To derive integral equations for the radiation and diffraction velocity potentials on the body boundary, Green's theorem is used (Lee & Newman (1989)). The integral equation for each of the potentials is enforced at the centroid of each panel. It solves up to second-order potential flow theory, so for obtaining the second-order potential, based on the perturbation method, the first-order motions need to be computed. It should also be noted that the integral equations for each of the potentials have nonunique solutions at the so-called irregular frequencies, leading to numerical solutions of these equations that are erroneous near these. The full derivation is thoroughly presented in Lee & Newman (1989). For this work, the tool used for the conceptual panel modelling to be exported to Wadam is GeniE.

3.3.7. TIME-DOMAIN ANALYSIS

The frequency-domain analysis outputs the hydrodynamic properties of the system straightforwardly. In order to carry out time-domain simulations, the software tool used is the RIFLEX-SIMO (SIMA), developed by MARIN-TEK. Here, the frequency-dependent hydrodynamic properties are transformed by means of a retardation function, based on the convolution theory. By applying the Fourier transformation, Equation 3.40 can be converted to the time-domain as:

$$(M_{ij} + A_\infty)\ddot{x}_j(t) + \int_0^t K_{ij}(t - \tau)\dot{x}_j(\tau)d\tau + C_{ij}x_j(t) = F_{i,exc}(t); \qquad i, j = 1, 2, ...6. \tag{3.41}$$

where $K_{ij}(t)$ is known as the retardation function. The time convolution of the radiation impulse-response functions with the platform velocities allows accounting for the linear memory effects within the time domain hydrodynamic models. This memory effect captures the load on the platform that persists from the outgoing free-surface waves radiated away by the platform motion. A detailed analysis of the time convolution of the radiation impulse-response functions can be found in Lee (1995).

The frequency-dependent added mass, damping and excitation forces can be expressed in terms of the retardation function as follows:

$$A_{ij}(\omega) = -\frac{1}{\omega}\int_0^\infty K_{ij}(\tau)\sin(\omega\tau)d\tau; \tag{3.42}$$

$$B_{ij}(\omega) = \int_0^\infty K_{ij}(\tau)\cos(\omega\tau)d\tau. \tag{3.43}$$

From these expressions the retardation function is computed, and if the forcing $\tilde{F}_{i,exc}(\omega)$ is inverted to $F_{i,exc}(t)$, all the terms involved in Equation 3.41 are known. The time-domain integration is done using the third order Runge-Kutta numerical method, as explained in SIMO (2012).

3.4. SUMMARY

In this chapter the background of the numerical tools to be used throughout the research, namely Navier-Stokes/VOF and potential flow theory, was given. A schematic summary is depicted in Figure 3.7.
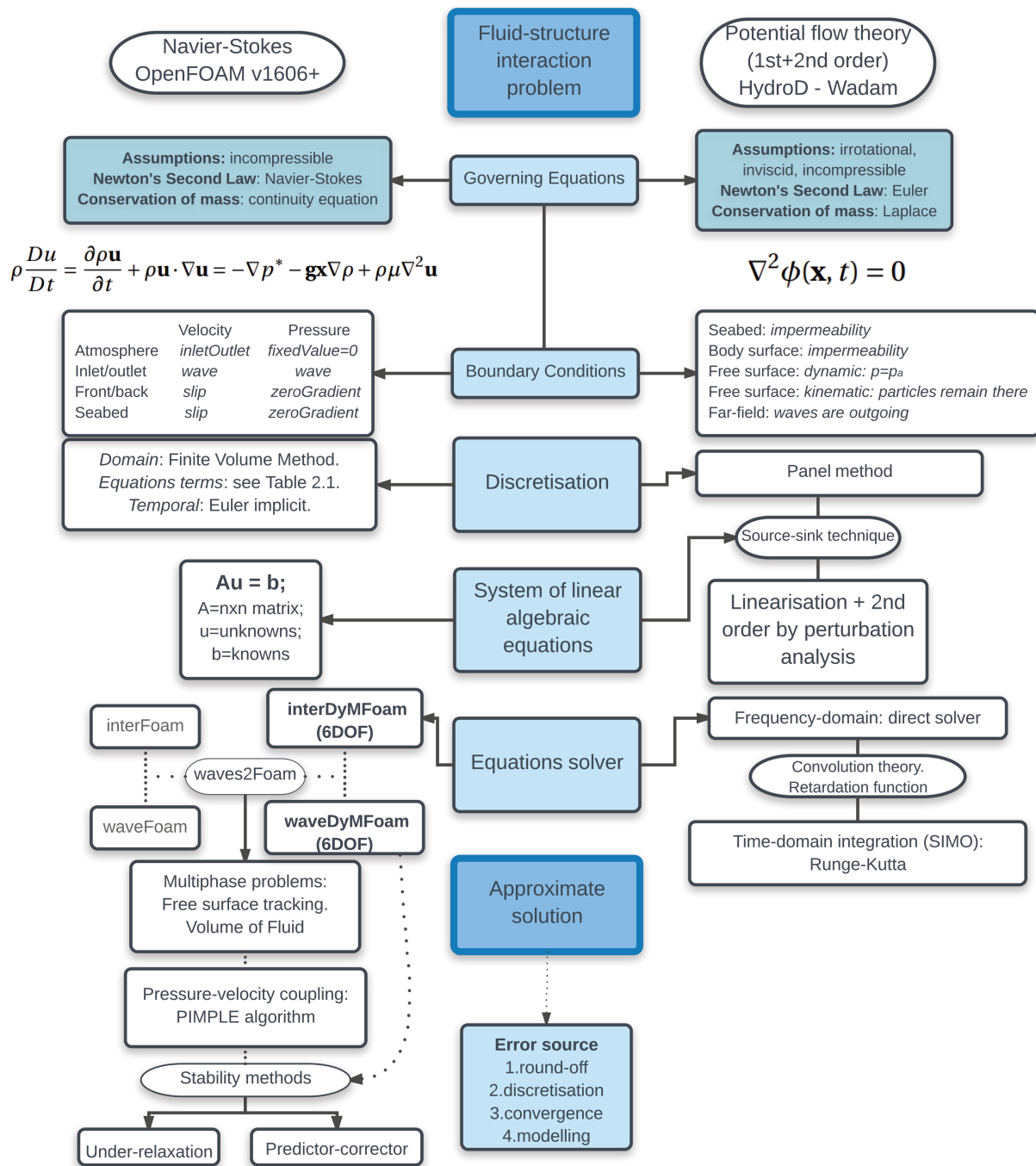
Navier-Stokes
OpenFOAM v1606+

Fluid-structure
interaction
problem

Potential flow theory
(1st+2nd order)
HydroD - Wadam

Assumptions: incompressible
Newton's Second Law: Navier-Stokes
Conservation of mass: continuity equation

Governing Equations

Assumptions: irrotational,
inviscid, incompressible
Newton's Second Law: Euler
Conservation of mass: Laplace

$$\rho \frac{Du}{Dt} = \frac{\partial \rho \mathbf{u}}{\partial t} + \rho \mathbf{u} \cdot \nabla \mathbf{u} = -\nabla p^* - \mathbf{gx}\nabla \rho + \rho \mu \nabla^2 \mathbf{u}$$

$$\nabla^2 \phi(\mathbf{x}, t) = 0$$

	Velocity	Pressure
Atmosphere	*inletOutlet*	*fixedValue=0*
Inlet/outlet	*wave*	*wave*
Front/back	*slip*	*zeroGradient*
Seabed	*slip*	*zeroGradient*

Boundary Conditions

Seabed: *impermeability*
Body surface: *impermeability*
Free surface: *dynamic: p=pₐ*
Free surface: *kinematic: particles remain there*
Far-field: *waves are outgoing*

Domain: Finite Volume Method.
Equations terms: see Table 2.1.
Temporal: Euler implicit.

Discretisation

Panel method

Source-sink technique

Au = b;
A=nxn matrix;
u=unknowns;
b=knowns

System of linear
algebraic
equations

Linearisation + 2nd
order by perturbation
analysis

interFoam

**interDyMFoam
(6DOF)**

Equations solver

Frequency-domain: direct solver

waves2Foam

Convolution theory.
Retardation function

waveFoam

**waveDyMFoam
(6DOF)**

Time-domain integration (SIMO):
Runge-Kutta

Multiphase problems:
Free surface tracking.
Volume of Fluid

Approximate
solution

Pressure-velocity coupling:
PIMPLE algorithm

Stability methods

Error source
1.round-off
2.discretisation
3.convergence
4.modelling

Under-relaxation

Predictor-corrector

Figure 3.7: Overview of the two numerical models used throughout this research.

4

FURTHER VALIDATION OF THE NONLINEAR NUMERICAL WAVE TANK

4.1. INTRODUCTION

In this chapter, the fully nonlinear numerical wave tank performance is further validated for two floating structures subjected to steep regular waves. The first case, presented in Section 4.2, comprises a two-dimensional floating box. The second one, presented in Section 4.3, is a vertical floating cylinder. The numerical results are analysed and compared to the experiments carried out by Ming et al. (2014) and Palm et al. (2016) respectively. For the two-dimensional case, the unforced response of the structure in roll is analysed using a free decay test. To study the response of the body in its three degrees of freedom, namely heave, roll and sway, it is subjected to incoming waves. The three-dimensional case is validated by performing free and moored heave and pitch decay, and by comparing the results to the experimental data. The structure of this chapter is depicted in Figure 4.1.
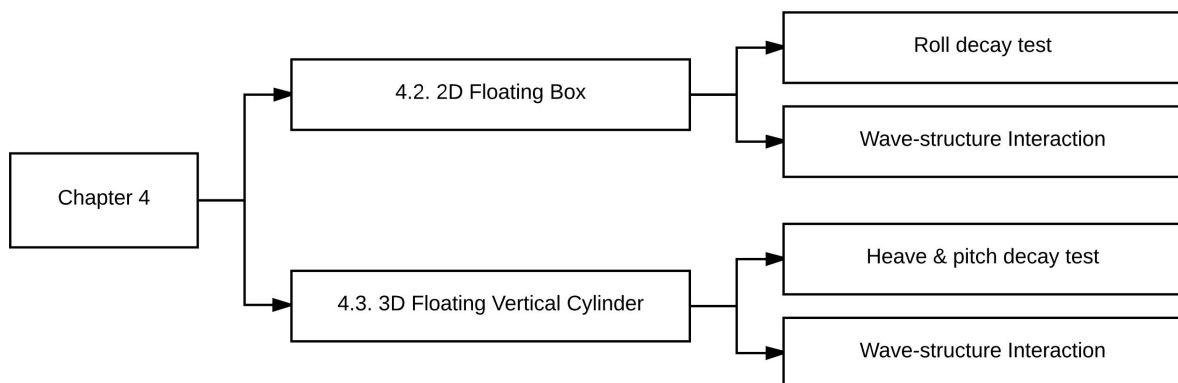
Figure 4.1: Scheme of Chapter 4 structure.

4.2. RESPONSE OF A TWO-DIMENSIONAL FLOATING BOX

This section presents the analysis of the response of a floating rectangular box in a two-dimensional domain. Firstly, the numerical set-up in which the numerical simulations are completed is presented. Secondly, the unforced response of the box is evaluated. Lastly, the wave-interaction problem is studied.

29

4.2.1. NUMERICAL SET-UP

The two-dimensional numerical wave tank is depicted in Figure 4.2, which emulates the experimental conditions described in Ming et al. (2014). The floating structure is placed at $x = 0$ m, 6 m away from the wave generation zone, and 12 m away from the absorption zone. The reason for such a relatively long domain is to limit any wave reflections from the outlet boundary. It should be noted that the experimental domain is longer; however, the position of the body with respect to the wave-maker is not specified. Therefore this distance cannot be exactly reproduced. Nevertheless, as long as a wave convergence study is completed to verify that there are no reflections from the boundaries (see Section 4.2.3), this difference does not affect the response. In the experiments the body is free to heave, roll and sway. It is not restricted from surging, pitching or yawing itself. To set the experiments as close as possible to a 2D domain, 1 mm distance is left from the walls to the body boundaries, as depicted in Figure 4.3. In the numerical domain, the body is free to move in the three degrees of freedom. The characteristics of the structure are presented in Table 4.1.
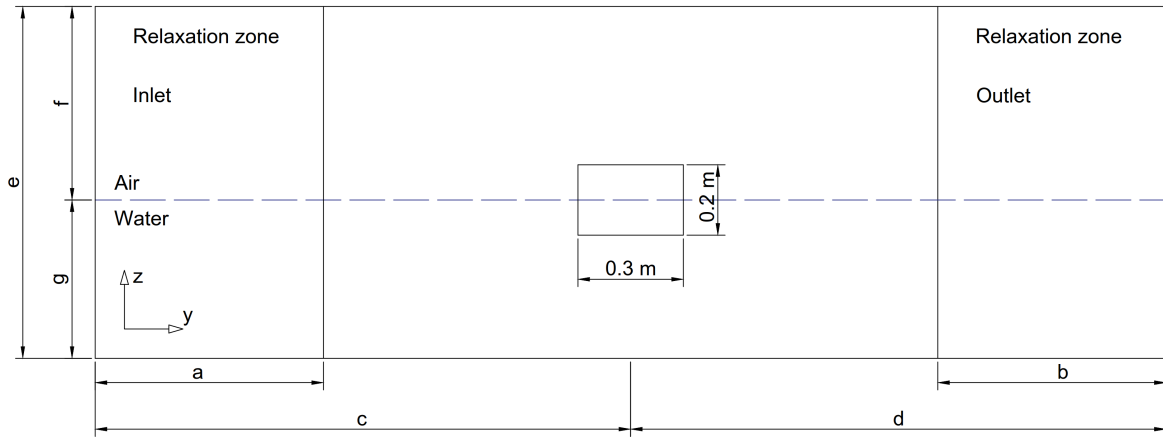
Figure 4.2: Numerical domain set-up dimensions. The dimensions, in meters, wavelength (w.l.) and length of the box (L), are: a = b = 2.3 m = 7.7 L = 1 w.l.; c = 6 m = 20 L = 2.7 w.l.; d = 12 m = 40 L = 5.2 w.l.; e = 1.5 m; f = 1.1 m; g = 0.4 m. The dimensions are given in number of wave lengths based on the wave-structure interaction in Section 4.2.3.

Table 4.1: Floating box structural characteristics.

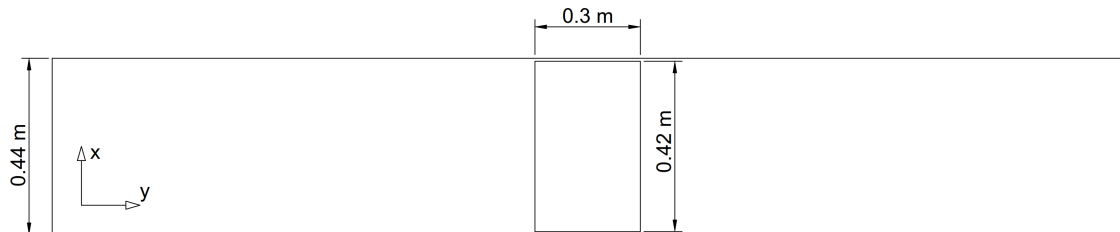| L [m]	B [m]	D [m]	Draft [m]	Mass [kg]	z_G [m]	I_{zz} [kg· m^2]
0.30	0.42	0.20	0.10	16.20	0.00	0.47

Figure 4.3: Overview of the experimental set-up (top-view).

The background mesh of the spatial domain is discretised by $n x m$ cells with a unit aspect ratio. It is generated in OpenFOAM® by the *blockMesh* utility. The refinement of the background mesh is based on the convergence of the solution, which is said to be convergent when an increase in the grid resolution does not lead to significant changes in the results.

Prior to solving the governing equations, the boundary conditions are specified. The inlet and outlet boundaries are given by the implemented wave theory. The decay test is carried out in still water, and therefore the imposed boundary condition at both the inlet and the outlet is a potential current with zero velocity. When the body is subjected to incoming regular waves, the inlet boundary condition is set as a stream function, as presented in Section 4.2.3. A slip condition is applied at the bottom boundary. The boundary condition at the front and back walls is set as *empty*, since these planes are normal to the third dimension, and therefore no solution is required. Physically, it means that there is no *x*-component in the equations.

The body is set in the numerical domain using an STL (stereolithography) file. Different levels of refinement around the structure can be applied, which may be achieved by various means. In this case, it is done with the *snappyHexMesh* utility, which generates two- and three-dimensional meshes containing hexahedra, and split-hexahedra, from triangulated surface geometries in Stereolithography (STL) format. It requires an already existing base mesh, where the body is sculpted, by iteratively refining the base mesh and morphing the resulting split-hex mesh to the surface geometry. The aspect ratio of the cells at this area should be as close as possible to unity. Since the body is floating and free to move in its 3 *DOF*, the mesh has to be able to deform, so that the body is allowed to move, without losing mesh quality. For this purpose, the dynamic mesh solver previously presented in Chapter 2 is applied. To relax the acceleration that results from the forces on the structure, the *acceleration-relaxation* approach, with $a = 0.5$ is used, based on the findings in Bruinsma (2016).

4.2.2. Free roll decay test

To analyse and compare the unforced response of the body in roll, a free decay test is executed. The initial rotation of the body is already applied on the STL, before importing it to the CFD domain.

The first uncoupled natural frequency in roll can be determined using a Fast Fourier Transform (*fft*), or by counting the number of oscillations and dividing by the time. The former method is influenced by the time interval in the simulation and by its length, which may compromise the accuracy. Therefore, in this case, the latter is applied. Besides the natural frequency, the linear and quadratic damping coefficients are estimated using the method presented in Hoff (2001) briefly described in Section 2.3.

Results and analysis of the free roll decay test

The time series of the roll displacement, for different levels of mesh refinement, is presented in Figure 4.4. The cell size is defined by the number of points per structure length (p.p.s.l.), where the characteristic length, in this case, is $L = 0.3\,\text{m}$. The response in roll is normalised with respect to the maximum roll angle ϕ_{max}, which coincides with the initial rotation of the centre of mass, equal to 9.43°.
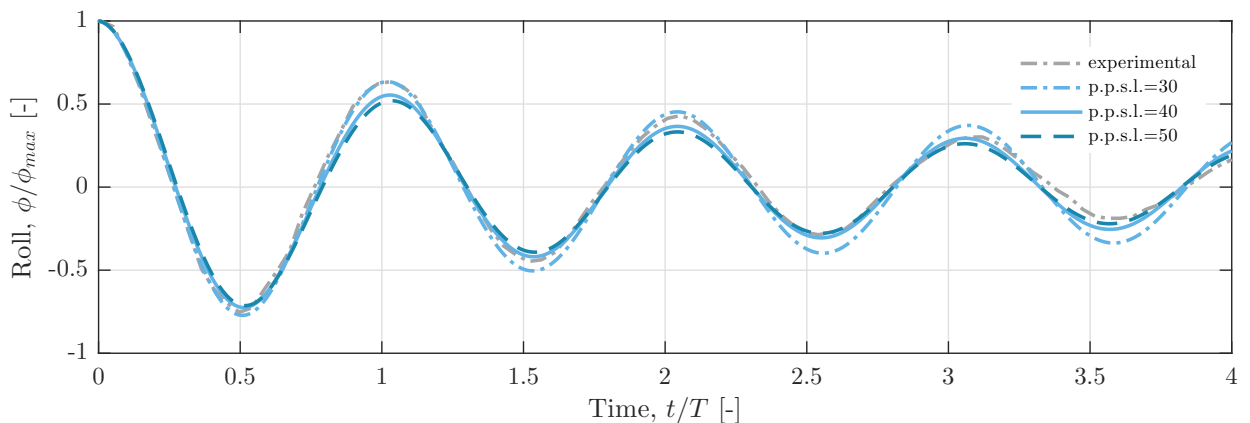

Figure 4.4: Roll free decay test time series, experimentally and numerically obtained for different grid refinements. It is normalised by the initial, and maximum, angular amplitude.

From Figure 4.4, it is firstly seen that the numerical solution converges. Secondly, although in general a good agreement with respect to the experimental solution is observed, the numerical result that corresponds to the highest discretisation shows an overestimation of the damping for the first and second periods of oscillation. However, for the last two periods, the damping seems to be better captured. Another observation is that the

period of oscillation for the experimental case is not constant. The reason behind can be found in the nonlinearities, or vortices, that are developed, and shed, as the body moves. Table 4.2 compares the natural period of the body in roll, and presents the linear and quadratic damping coefficients, b_1 and b_2, respectively, for three decay periods. Note that the way of obtaining the damping parameters is simplified, and that research in this field is ongoing. If just the first three oscillation periods are analysed, the mean period of the experimental model is 1.53 s, equal to the numerical model natural period. However, if two more cycles are taken into account, the mean period is increased to 1.57 s, whereas for the numerical model it stays approximately the same. The linear and quadratic experimental damping coefficients calculated based on the first three periods are 0.181 rad/s and 0.017 rad^{-1}, respectively.

Table 4.2: Comparison of the roll natural period an damping coefficients for the different spatial discretisations, based on the first three periods.

Spatial discretisation [p.p.s.l.]	$T_{n4,num}$	b_1 [rad/s]	b_2 [1/rad]
30	1.54	0.014	0.031
40	1.53	0.077	0.042
50	1.53	0.170	0.045

Although the method to obtain these should be more sophisticated, a comparison can still be carried out between the two models regarding the obtained results. The linear damping for the highest resolution case is better captured, as can already be expected from the analysis of Figure 4.4. However, it is especially remarkable the lower quadratic (nonlinear) damping from the experimental data, which could be explained by different facts. The first one is related to the non-trivial difficulties to overcome when measuring roll in physical experiments, which may lead to not so accurate results. Another possible reason to explain the mismatch in damping is the approach used to estimate it. Although the procedure applied throughout this work is widely used in industry, it should be born in mind that roll damping implies a highly nonlinear mechanism, as described in Chakrabarti (2001), which may also involve higher-order components. The third one is related to the fact that no turbulence model is implemented in this simulation. This implies that, unless the mesh is fine enough to be able to solve the turbulent boundary layer, the characteristic shear stresses resulting from the small eddies, are not captured. Since, due to computational resources restriction, the mesh is too coarse to capture these effects, it is reasonable to state that the numerical solution is likely to present a lower damping. A fourth reason for this lower damping can derive from the 3D-effects. In the numerical domain, these 3D effects are completely neglected, whereas in the experiments, although it is a channel with a much smaller third dimension, it is not a pure two-dimensional set-up, and consequently the presence of 3D effects cannot be entirely ruled out. A fifth reason can be found in the fact that the numerical model is not able to capture all the effects of the nonlinearities, as can be proven by the fact that the period remains approximately constant, as opposed to the variation in the experimental model. Despite these discrepancies between the numerical and experimental solution, it can be concluded that the experimental results presented in Ming et al. (2014) for the roll decay test are generally well reproduced.

4.2.3. WAVE-STRUCTURE INTERACTION

In this section, the motion response of the floating box to steep regular waves is presented and analysed. Prior to subjecting the structure to these waves, which propagate along the y-axis, a convergence study of the wave propagation is completed.

WAVE PROPAGATION

In Ming et al. (2014) it is stated that the waves are linearly generated by a piston-type wave-maker. However, it should be noted that it is, in general, very difficult to send perfect linear waves, since the nonlinear terms are likely to show up. For this reason, in the numerical simulation, the wave is generated based on the stream function wave theory (or Fourier approximation wave theory) presented in Fenton (1988). The target solution of the outlet boundary can be defined by applying the same wave conditions as it is done for the inlet boundary or by setting a constant current with zero velocity. The former is advisable if the target solution is known beforehand. In this case, the latter is used. The characteristics of the generated stream function wave in the numerical simulation are presented in Table 4.3.

Table 4.3: Wave parameters of the fully nonlinear steep regular wave, generated as a stream function.

f [Hz]	T [s]	H [m]	λ [m]	$\dfrac{d}{gT^2}$	$\dfrac{H}{gT^2}$	Fourier modes
0.83	1.2	0.06	1.95	0.028	0.00425	32

There are two ways to implement the wave. The first one implies a ramping-up stage, whereas the second one consists of applying the fully developed wave from the beginning of the simulation. In this case, the second approach is implemented, due to the meshing restrictions described in the following section. To determine the free surface elevation, the wave gauges are set between the generation zone and 0.25 m downstream the body, which corresponds to the maximum distance that the body is expected to move in the y-direction.

In Figure 4.5a the numerical surface elevation time series measured 0.25 m away from the body centre of mass, is compared to the analytical solution of the stream function. Figure 4.5b compares the amplitude of the first wave harmonic along the domain to the analytical solution. The highest level of refinement here presented is of 40 p.p.s.l., which corresponds to a number of points per wavelength of 300 and 8 points per wave height. The 20 p.p.s.l. refinement corresponds to 4 points per wave height and 150 points per wave length. Note that just the first fifteen wave periods are taken into account for the computations. From the time series it can be appreciated how after approximately two and a half wave periods, the wave amplitude decreases with respect to the analytical solution. The cause for this is found on the surface smearing, even though this effect is already reduced by including an interface compression term in the α field transport equation, as explained in Chapter 2. By comparing the analytical and the numerical solutions, it can be stated that a mesh resolution of 20 points per structure length yields an error in surface elevation, due to numerical diffusion, of no more than 4.5% for the first harmonic amplitude.

Given the small error if the lowest grid resolution (20 p.p.s.l.) is used, the background mesh presents this refinement, to decrease the computational costs. It should nevertheless be born in mind that even though the background mesh resolution is of 20 p.p.s.l., a refinement around the structure surface is carefully applied since relevant physical phenomena are likely to happen at the region immediately next to the structure surface. Hence the refinement is applied according to the results of the roll decay test study (see Figure 4.4), i.e. with a spatial discretisation around the structure of 40 p.p.s.l. It should be noted that throughout the current case, a difficulty concerning the dynamic mesh motion utility was encountered, based on the fact that the current set-up restricts the mesh deformation by an outer radial distance, as already defined in Chapter 2. This radial distance cannot be larger than the water depth, unless the boundary condition for the mesh displacement at the bottom is modified. Thus, the first solution to get around this problem is to initialise the wave at the *COG* of the body at the corresponding phase, as an attempt to make it coincide with the experiments. This way, an initial motion in sway of the body while the ramping-up is taking place is avoided, allowing for a higher computational time before the grid squeezeness surpasses the limits. The second strategy to overcome this problem is to change the boundary condition at the bottom concerning the point displacement. Therefore, the fixed value boundary condition is changed to a zero gradient condition. For the same reason, a convergence study of the background mesh cannot be completed since a finer mesh implies that the cells are more squeezed. Nevertheless, this is not relevant, since, as already stated when the background mesh convergence study was presented, a refinement of 20 p.p.s.l. was already proven to yield a sufficiently low diffusive error in the wave propagation.

RESULTS AND ANALYSIS OF THE WAVE-STRUCTURE INTERACTION

Figures 4.6a, 4.6b and 4.6c present the motions of the floating structure as a result of the incoming regular waves, for five wave periods, from the second wave period on. The previous wave period is discarded to avoid the initial impact on the body.

The response in heave, normalised by the wave height, shows a good agreement with the experimental results, both in phase and in amplitude. The response in roll shows a larger error in amplitude, although the phase is in accordance with the experiments. A non-zero mean roll angle, caused by a mean roll moment, is observed in both the experiments and numerical results. Its magnitude is seen to be well captured. After 4.5 periods, a small decrease in the roll amplitude is observed in the numerical solution. This can be explained if the response
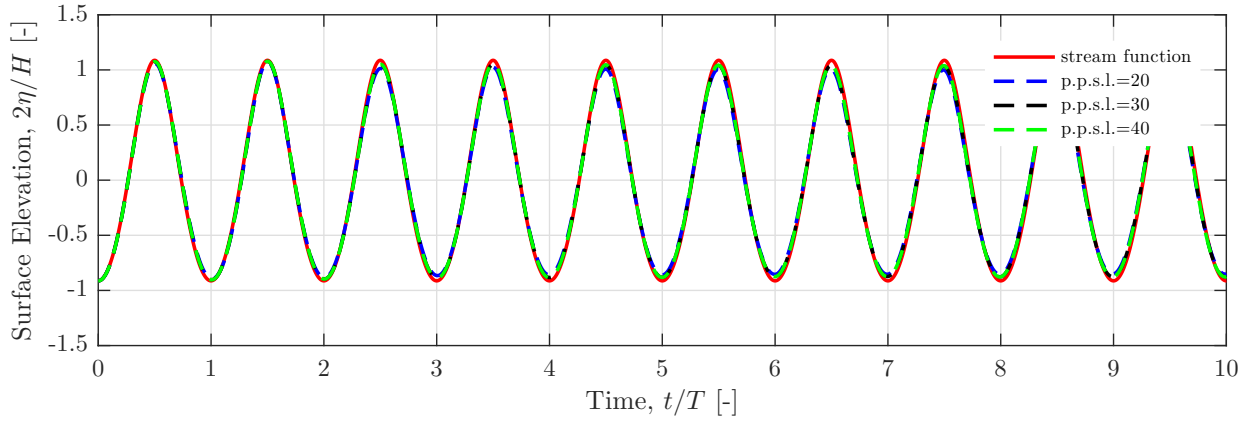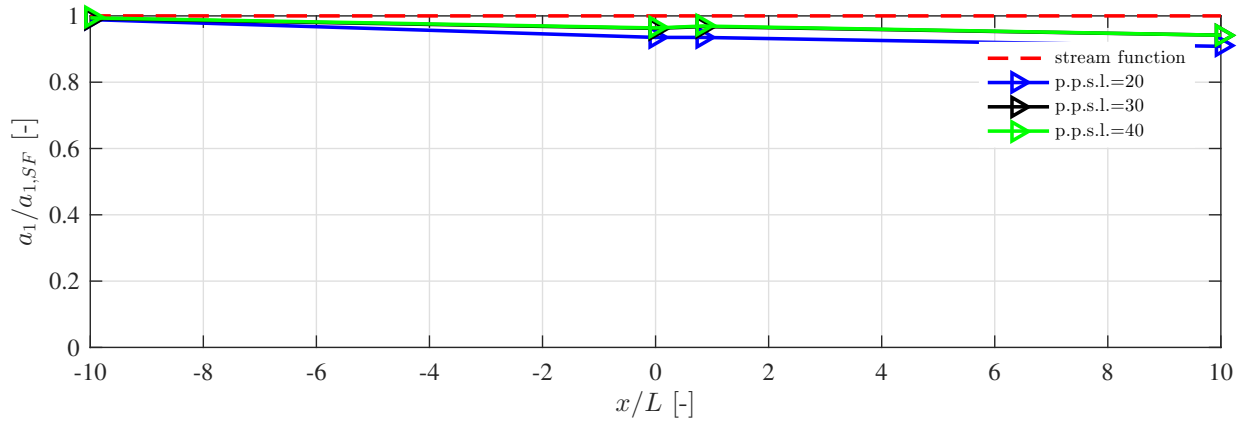
(a) Time series of the surface elevation at $x/L = 0$.

(b) First harmonic amplitude a_1, normalised by the first harmonic amplitude of the analytical solution $a_{1,SF}$.

Figure 4.5: Comparison between the numerical results for different grid refinements and the analytical solution of the stream function. a_1 is the amplitude of the first harmonic component of the incoming wave, and $x/L = 0$ corresponds to the point where the *COG* of the cylinder is to be placed.

in sway is analysed at this same time-step, when the drift starts to differ. The reason lies on an artificial stiffness coming from the mesh being squeezed as the body drifts further. This has a consequence in both the sway and, as seen, roll responses amplitude. The response in sway shows a mean drift motion of the floating body, caused by the mean drift force. As a consequence of the first-order loading, the body sways periodically. The three components oscillate with the same period, which is slightly larger than the wave period. This is explained by the effect of the drift motion, since it takes more time for the wave to reach the body as it moves further in the y-direction. The computational error for the body motion response is presented in Table 4.4, where $|\eta_{num}|$ is the mean of the peak-to-peak total amplitude of the numerical response, in the respective *DOF*, and $|\eta_{exp}|$ the experimental one. Note that the former amplitudes are computed based on the four periods presented. From these numbers, it can be concluded that, despite the dynamic mesh set-up difficulties, the numerical results are in good agreement with the experimental data.

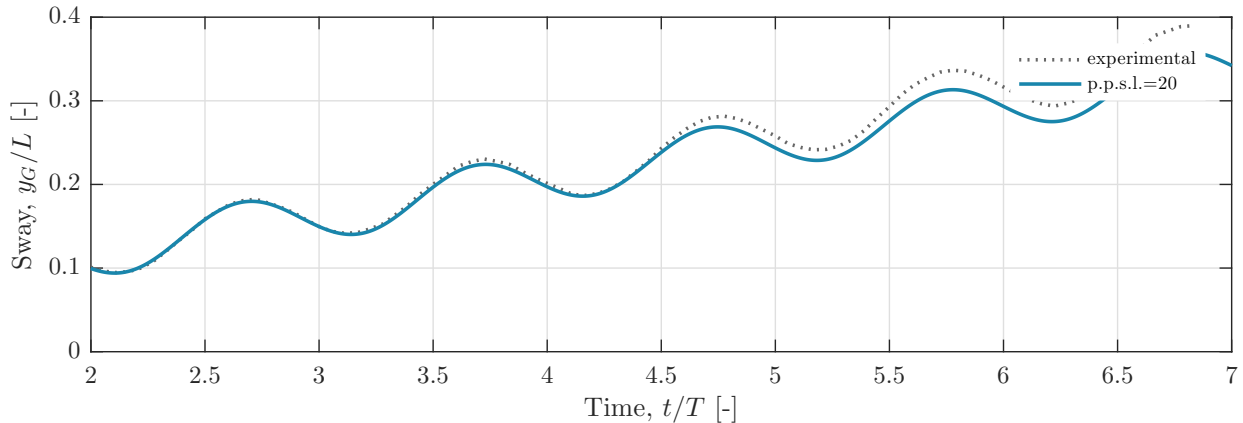Table 4.4: Error study for a background mesh refinement of 20 p.p.s.l., based on five wave periods.

DOF	$|\bar{x}_{i,num}|$	$|\bar{x}_{i,exp}|$	$\Delta\bar{x}_i$ [%]
Heave [m]	0.065	0.066	1.7
Roll [deg]	0.160	0.140	7.1
Sway [m]	1.580	1.500	2.3
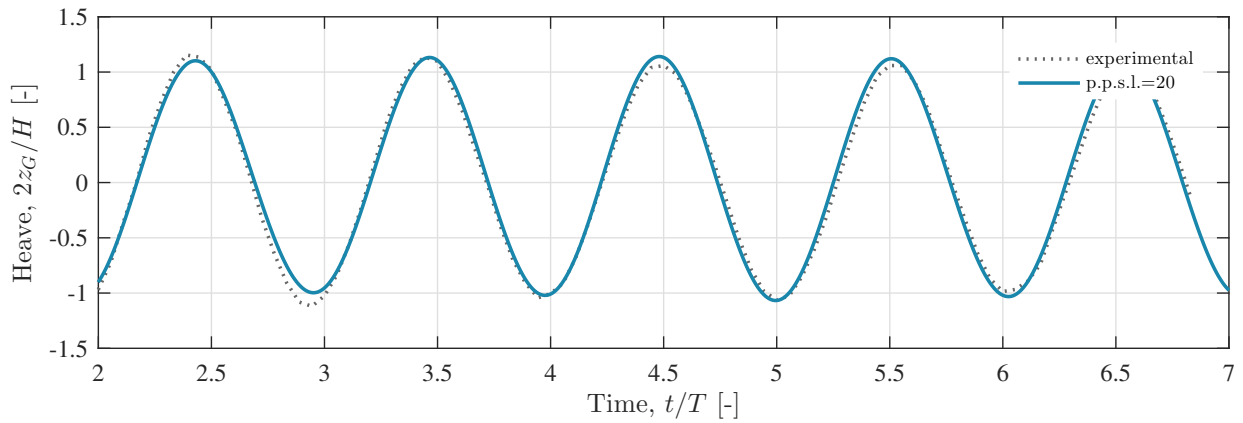
(a) Heave response.
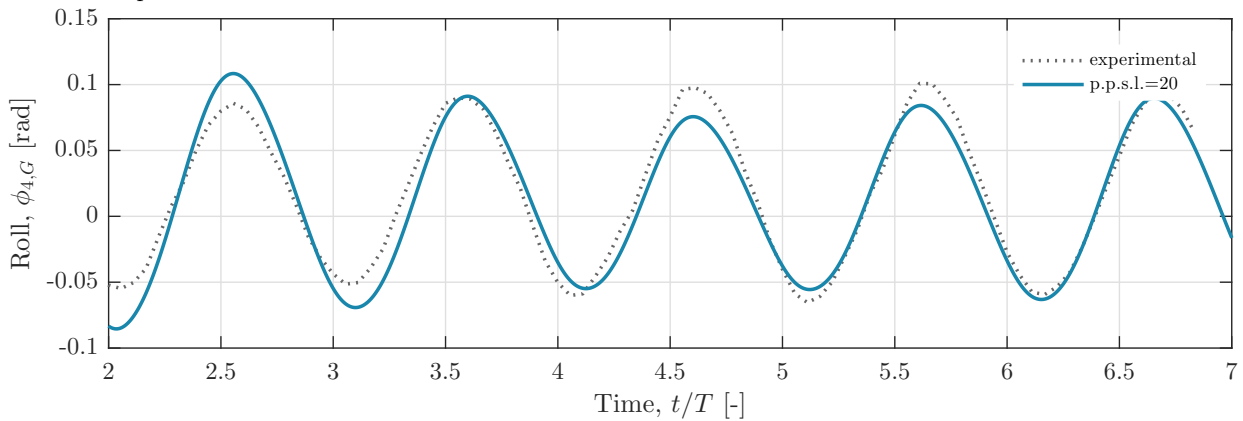
(b) Roll response.

(c) Sway response.

Figure 4.6: Response of the floating box due to an incoming regular wave. The heave is normalised by the wave amplitude and the sway by the characteristic length of the box. The time is normalised by the incoming wave period.

4.3. Response of a Three-dimensional Vertical Floating Cylinder

Throughout this section, the response of a floating vertical cylinder is evaluated. Firstly, free heave and pitch decay tests are completed and compared to the experimental results presented in Palm et al. (2016), where a wave energy converter with the same structural properties is analysed. At a second stage, the structural response of the same vertical cylinder, moored and subjected to regular waves, is examined.

4.3.1. NUMERICAL SET-UP

The current case is run in a three-dimensional domain, with the main dimensions depicted in Figure 4.7. Note that four relaxation zone could be applied, but to have the most similar configuration to the experimental set-up, two relaxation zones are set in the x-direction. The schemes and boundary conditions used for the domain disretisation are the same ones applied to the two-dimensional case. The only change is the boundary condition at the front and back faces of the numerical domain for which in this case, a slip condition is imposed. The body is free in its six degrees of freedom. The characteristics of the structure are presented in Table 4.5.
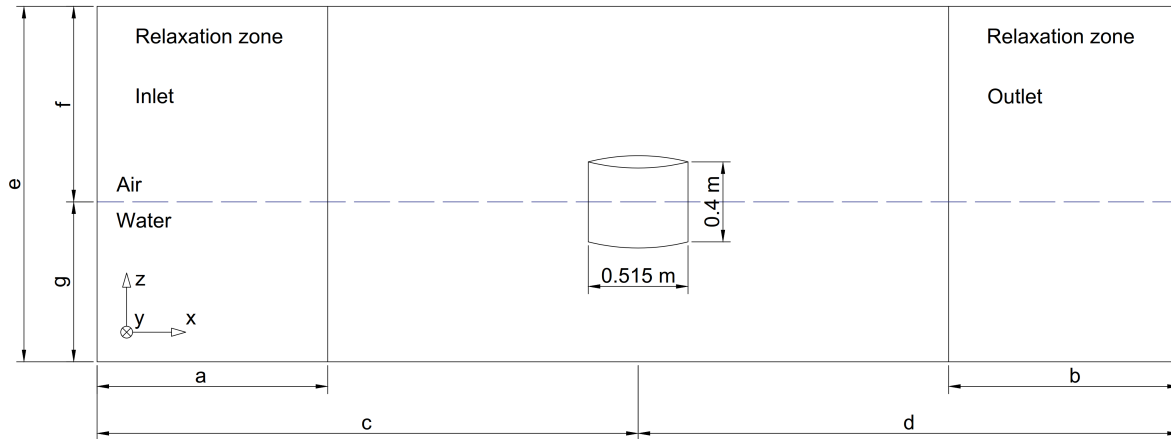
Figure 4.7: Numerical domain set-up, with the dimensions indicated with letters. The dimensions, in meters and cylinder diameters (D), are: a = 0.5 m = 1 D = b; c = 3 m = 5.8 D = d; e = 1.8 m; f = 0.9 m; g = 0.9 m. The width is 5 m.

Table 4.5: Floating cylinder structural properties.

d [m]	H [m]	Draft [m]	Mass [kg]	KG [m]	$I_{yy} = I_{xx}$ [kg· m^2]
0.515	0.401	0.272	35.85	0.0758	0.9

4.3.2. HEAVE AND PITCH DECAY TESTS

The following cases are presented and analysed throughout this section: moored and free heave and pitch decay tests. For the free heave decay test the centre of mass of the cylinder is displaced 0.076 m from its equilibrium. To determine the convergence of the solution, three spatial discretisations are examined, related to the number of points per cylinder diameter (p.p.c.d., analogous to the points per structure length for the previous two-dimensional case). For the free pitch decay test, the centre of mass is initially rotated 8.88° from its equilibrium. The initial rotation of the body is previously implemented in the STL file and then exported to the numerical domain. A convergence study based on the level of mesh refinement around the body is equally carried out. In addition, a sensitivity analysis is completed, to demonstrate how the response of the cylinder in pitch is affected by small variations in the structural properties, namely the moment of inertia and the centre of mass position.

RESULTS AND ANALYSIS OF THE DECAY TESTS

The response in heave is depicted in Figure 4.8. It is normalised by the initial displacement. The two finest grids show very close results, and in good agreement with the experiments. The coarsest mesh presents a large difference in damping, and also in natural period, with an error six times as large as the finest grid evaluated here, as can be seen in Table 4.6. The natural period obtained from the heave decay test experimental data is 1.112 s. The numerical heave natural period for the three levels of refinement is computed based on the first three periods.
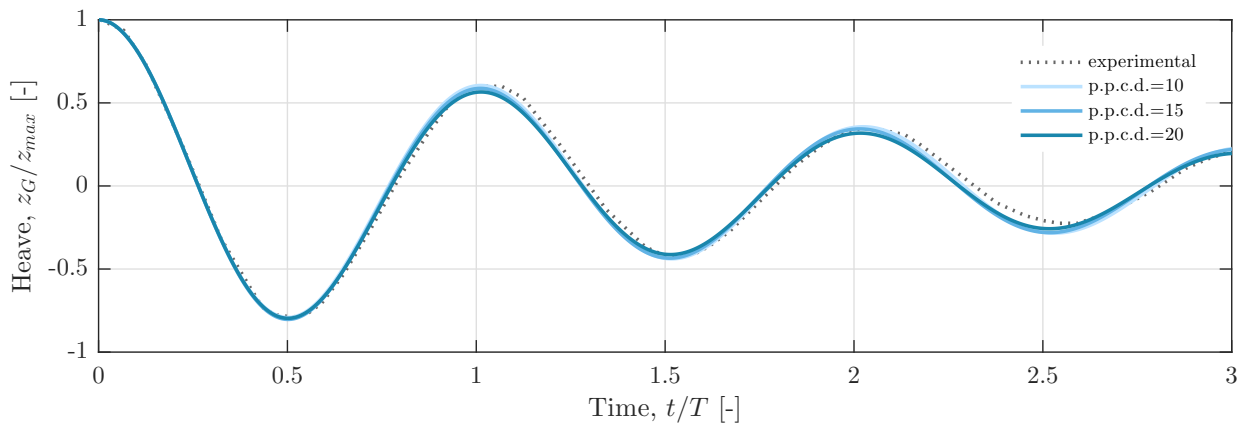
Figure 4.8: Time series of the free heave decay test. The motion of the *COG* is normalised by the maximum displacement, and the time is normalised by the heave experimental natural period of the structure.

Table 4.6: Comparison of the heave natural period for the different spatial discretisations, based on the first three oscillations.

Spatial discretisation [p.p.c.d.]	$T_{n3,num}$	Error [%]
10	1.121	0.81
15	1.114	0.18
20	1.111	0.08

Given the low error, a discretisation of 15 p.p.c.d. is chosen for the following case, which comprises the same heave decay test, but moored. The modelling approach of the mooring lines in OpenFOAM® is explained in Chapter 3, Section 3.2. The mass per length of the chain is 0.1447 kg/m, the submerged weight 1.24 N/m and the diameter 0.0048 m. Therefore the implementation of the mooring lines implies a higher mass and a higher stiffness. It is expected to increase or decrease depending on how much the increase in mass outweighs the increase in stiffness. The heave period is not expected to be significantly affected. The experimental model natural period in heave shows a slight increase, according to Palm et al. (2016). However, this is not seen in the numerical results, which show almost the same natural period, as seen in Figure 4.9, in which the response in heave, normalised by a maximum initial displacement equal to 0.075 m, is depicted. The natural period experimentally obtained is 1.13 s, whereas the numerically obtained is of 1.113, a 1.5% lower.
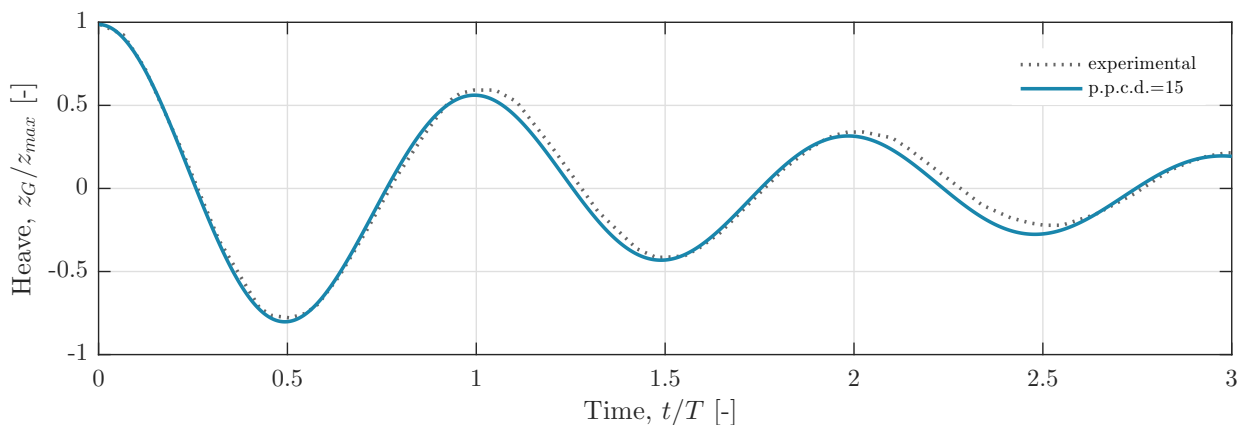
Figure 4.9: Moored heave decay test time series. The motion of the *COG* is normalised by the maximum initial displacement and the time by the heave experimental natural period of the structure.

The response of the body for the pitch free decay test is presented in Figure 4.11, compared to the experimental data. Please note that due to the process of digitising the experimental time series, there are some discontinuities, which do not correspond to the solution, but just to the low number of points digitised. The results are obtained

for a background mesh of 15 p.p.c.d since the level of refinement of the background mesh is not likely to affect the response as much as the refinement around the structure. The results for different levels of refinement around the structure are presented, and defined as *level 1*, *level 2* and *level 3*. They are depicted in Figure 4.10. The first level has the highest refinement around the structure, but the least between layers of refinement, so the cells close to the surface boundary are approximately one sixty-fourth of the size of the base mesh. The third level presents a lower degree of refinement around the structure, but more layers of refinement between the levels. The cells close to the surface boundary are approximately one sixteenth of the size of the base mesh. The second case lies in between the first and the third. The first level presents an abrupt change in the dimensions of the respective neighbour cells between the different layers. This leads to an artificial, or numerical, damping in the response, which can be visualised in Figure 4.11. Here the model with the largest refinement around the structure, but at the same time, with more abrupt changes within the cell size between layers, shows the largest damping. Note that the heave decay tests were carried out with a *level 3* of refinement.

(a) Level 1.   (b) Level 2.   (c) Level 3.
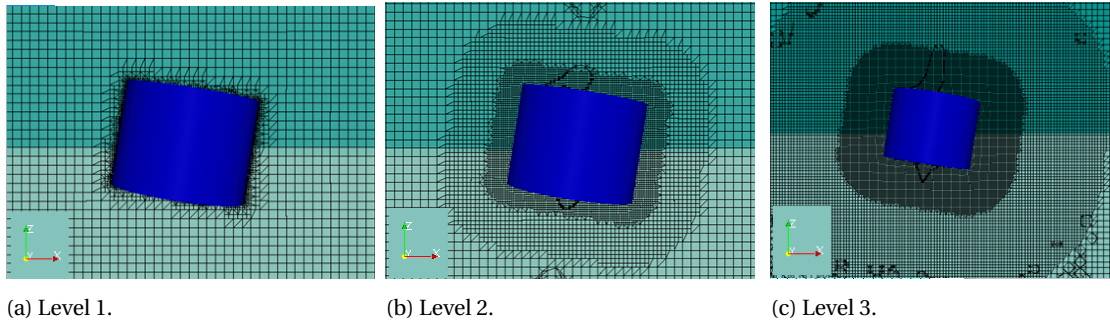
Figure 4.10: Levels of refinement around the floating cylinder for the pitch decay test.
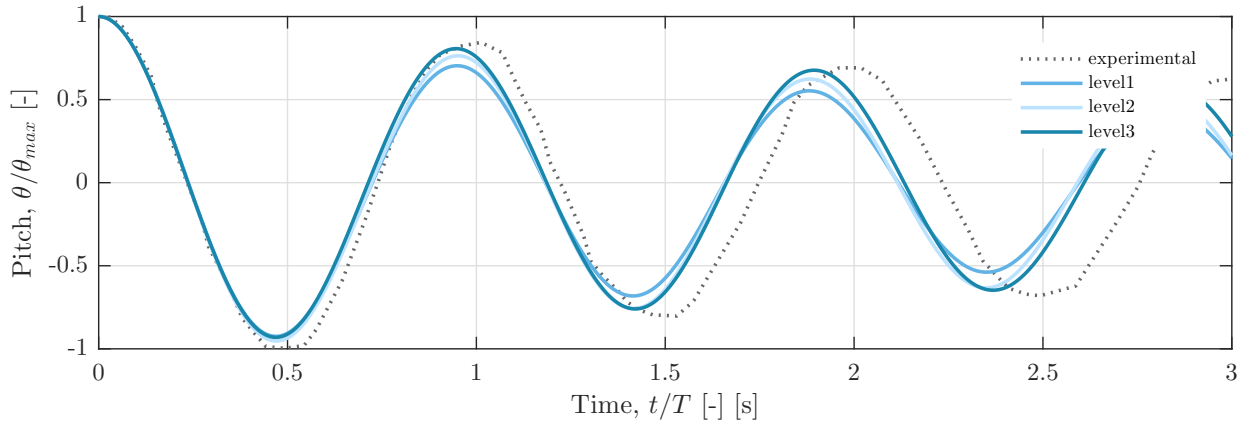

Figure 4.11: Free pitch decay test. The rotation of the *COG* is normalised by the maximum rotation, and the time is normalised by the experimental pitch natural period of the structure.

Table 4.7: Comparison of the pitch natural period for the different spatial discretisations.

Refinement level around structure	$T_{n5,num}$ [s]	Error [%]
1	1.098	6.15
2	1.098	6.15
3	1.110	5.13

Besides the overestimation of the damping, the natural period is seen to be relatively off for the three cases if it is compared to the experimental results, as also seen in Table 4.7. The natural period of the experimental model is stated to be 1.17 s in Palm et al. (2016). If the uncoupled natural period is calculated according to:

$$T_{n,5} = \sqrt{\frac{I_{55} + A_{55}}{C_{55}}}, \tag{4.1}$$

with the hydrodynamic properties stated in Palm et al. (2016), and taking the lower limit of the added mass A_{55}, the period results to be 1.11 s. The numerical results presented in Palm et al. (2016) also show these differences compared to the experimental data presented. This leads to the conclusion that there are some unavoidable inaccuracies in the experimental measurements. The origin of those may be in the measurement of the inertia around the y-axis, or in the position of the centre of mass with respect to the keel of the body. To verify this, a sensitivity analysis varying these parameters is completed and presented in Figure 4.12. From Table 4.8 (and from Figure 4.12), it is seen how the period is increased if the pitch moment of inertia, $I_{yy} = I_{55}$, also does, and the metacentric height GM of the body decreases due to the increment of KG.
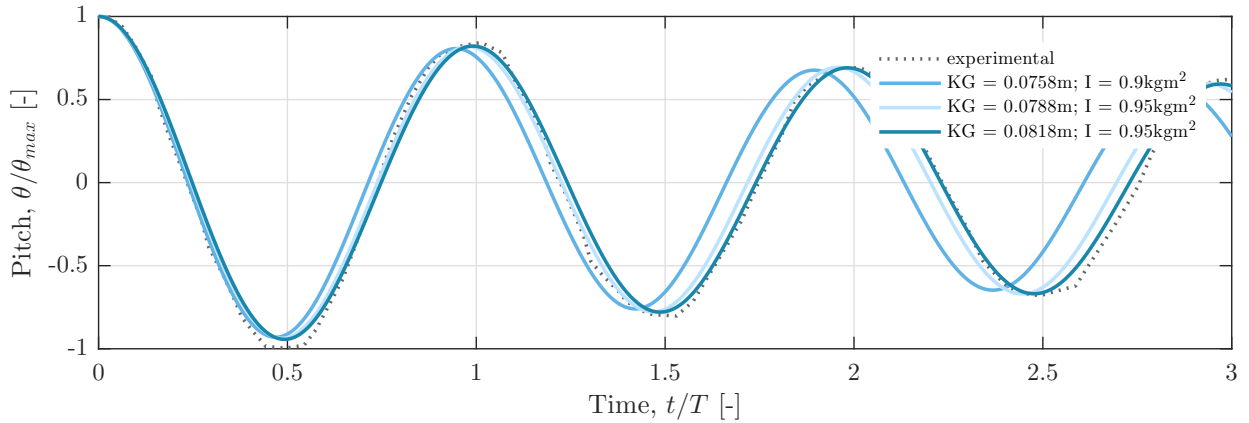
Figure 4.12: Sensitivity analysis of the pitch unforced response for with varying KG and I_{55}.

Table 4.8: Comparison of the pitch natural period for different KG and I_{55}.

KG [m]	I_{55} [kg·m^2]	$T_{n5,num}$ [s]
0.0758	0.90	1.098
0.0788	0.95	1.130
0.0818	0.95	1.147

If the period is hand-calculated for an inertia equal to 0.95 kg·m^2, and $KG = 0.0818$ m, the natural period increases to 1.17 s, which is the one presented in the reference paper. The results from the numerical model for this case are proven to be closer to the theoretical one, as well as to the experimental model. Hence two conclusions can be drawn from the time series of the pitch decay response. The first one concerns the difficulties when measuring the dynamic properties of a floating body and its response. The second one is that the numerical model is capable of fairly reproducing the experiments, and also to be sensitive to any minimal change in the structural properties.

One more aspect of this model has to be noted: the proximity of two natural frequencies for two degrees of freedom, namely heave and pitch. This leads to the excitation of the heave motion if the pitch is also excited, as it is the case, and vice-versa. Consequently, the pitch restoring coefficient varies harmonically, due to the heave variation. The exchange of energy between the two degrees of freedom can be depicted in Figure 4.13, where the amplitude of the motion in heave is seen to increase, while the pitch is damped.

The pitch motion can be described as:

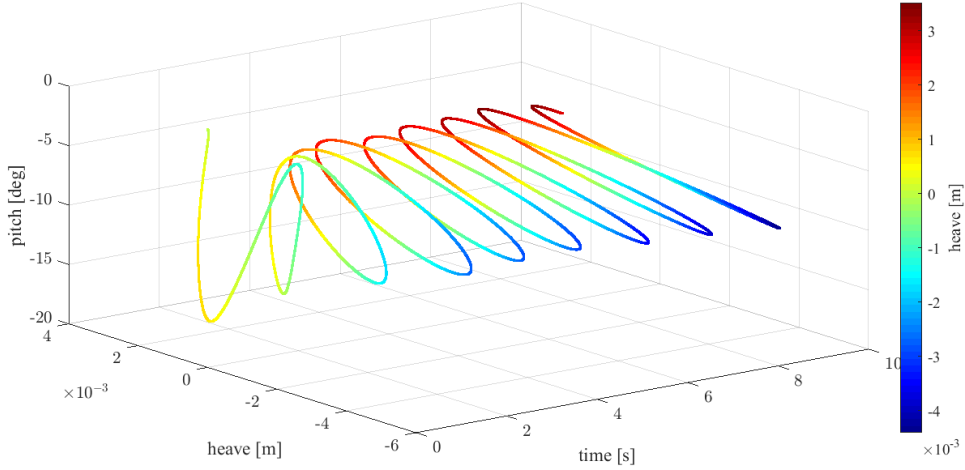$$(I_{55} + A_{55})\frac{d^2\eta_5}{dt^2} + B_{55}\frac{d\eta_5}{dt} + C_{55}(t)\eta_5 = 0, \tag{4.2}$$

Figure 4.13: Heave response for the pitch decay test.

with C_{55} equal to $\rho g V (GM_{Tm} + \delta GM_T \sin(\omega_e t))$, where δGM_{Tm}, ω_e and β are, respectively, the amplitude of the time oscillations of the transverse metacentric height GM_T, its frequency and its phase. These oscillations are caused in the current case by the heave and pitch motions. GM_{Tm} is the mean transverse metacentric height, associated with the mean restoring coefficient as $C_{55} = \rho g V GM_{Tm}$. If Equation 4.2 is divided by $(I_{55} + A_{55})$, it yields:

$$\frac{d^2\eta_5}{dt^2} + 2\xi\omega_n\frac{d\eta_5}{dt} + \omega_n^2\left[1 + \frac{\delta GM_T}{GM_{Tm}}\sin(\omega_e t)\right]\eta_5 = 0 \tag{4.3}$$

where $\xi = B_{55}/[2(I_{55} + A_{55})\omega_n]$ is the fraction of the damping relative to the critical one and $\omega_n = 2\pi\sqrt{\dfrac{C_{55}}{(I_{55} + A_{55})}}$.

From this equation both the coupling in pitch and heave and the displaced volume and change in the metacentric height GM of the cylinder variation in time, can be seen. This is known as Mathieu's (damped) equation, which is a specific case of the second-order ordinary differential equation type known as Hill's equation, with the form that follows:

$$\ddot{x} + c\dot{x} + (\alpha + \beta\cos t)x = 0. \tag{4.4}$$

If Equation 4.3 is divided by the heave frequency of oscillation ω_3 squared, and is compared to Eq. 4.4, the parameters α, β and c yield:

$$\alpha = \frac{\rho g V GM}{(I_{55} + A_{55})\omega_3^2} = \frac{\omega_5^2}{\omega_3^2}, \qquad \beta = \frac{0.5\rho g V \delta GM_T}{(I_{55} + A_{55})\omega_3^2}, \qquad c = \frac{B_{55}}{(I_{55} + A_{55})\omega_3^2}.$$

The condition of instability in Mathieu's equation depends on these parameters. It can be identified using a parametric plane, shown in Figure 4.14, and also known as *Strutt diagram*. Its derivation is based on the solution of the Hill's equation with the Mathieu parameters and can be consulted in Koo et al. (2004). Here α and $\delta GM_T/GM_{Tm}$ are approximately equal to unity (green point). The damping of the system, as well as the increment of α, reduce the area of instability. However, in this case, the damping ξ is calculated and proven to be too low to avoid the unstable region, which is not a desired situation. Nevertheless, the scope of this section is not to design a stable system but to further validate the nonlinear numerical wave tank. Therefore the identification of this instability arising confirms that the numerical model can capture these type of instabilities, arising from nonlinearities. A rigorous study of these is beyond the scope of this master thesis, although a thorough analysis can be found in MacLachlan (1947) or Nayfeh & Mook (1995).
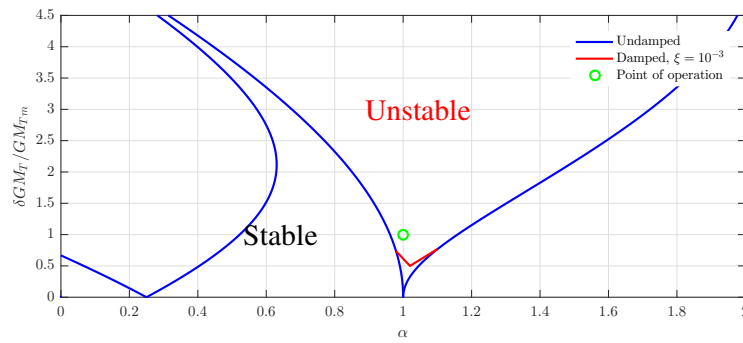
Figure 4.14: Stability diagram for undamped Mathieu's equation. Note that it is symmetric around the α-axis.

The moored pitch decay test is very similar to the free one. The time series is presented in Figure 4.15, from which it can, once again, be inferred that the main parameters affecting the natural response in pitch are very sensitive. Since it was already proven to be the case for the free pitch decay test, a sensitivity analysis is not carried out. The results for the original configuration are presented in Table 4.15 and the time series in Figure 4.15.
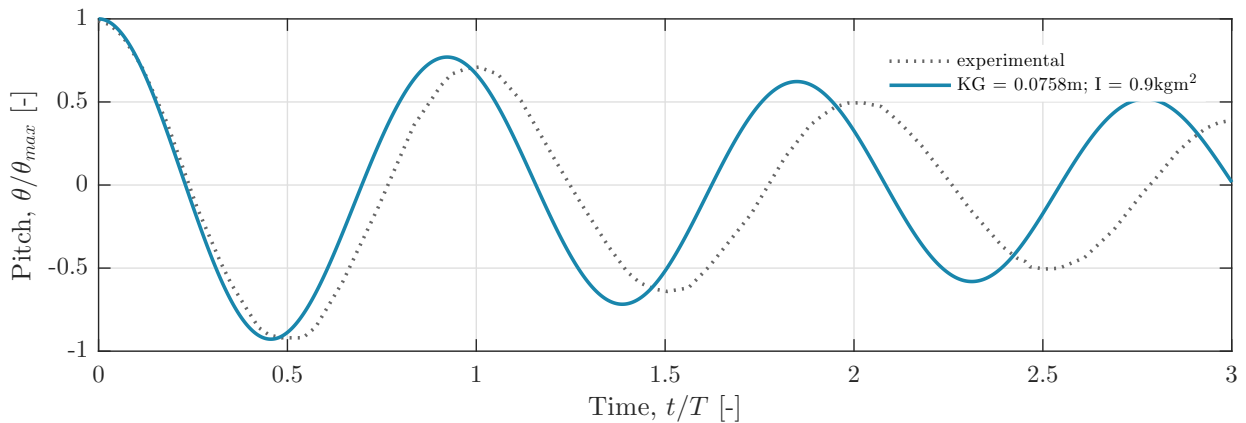
Figure 4.15: Vertical floating cylinder moored pitch decay test. The rotation of the *COG* is normalised by the maximum rotation, and the time is normalised by the experimental pitch natural period of the structure.

Table 4.9: Comparison of the pitch moored natural period for the different spatial discretisations with the counting method.

Spatial discretisation [p.p.c.d.]	$T_{n5,exp}$ [s]	$T_{n5,num}$ [s]	Error [%]
15	1.16	1.05	10.25

4.3.3. WAVE-STRUCTURE INTERACTION

This section presents the response of the moored circular cylinder in heave, pitch and surge to the incoming regular waves presented in Table 4.11. The dimensions of the numerical domain set-up, as referred to in Figure 4.7 are indicated in Table 4.10.

Table 4.10: Dimension of the numerical set-up, with the letters referred to Figure 4.7, in meters (m), diameters (D) and wavelengths (w.l.).

|	a	b = c	d
(m)	3	6	9
(D)	5.80	11.65	17.50
(w.l.)	1.35	2.70	4.00

Prior to subjecting the body to the waves, a convergence study regarding the incoming waves is completed, and presented in Figure 4.16. The cells are efficiently distributed so that the area around the body and the free surface are well refined. The number of cells per wave height is 400, and the number of cells per wavelength is 67, upstream of where the body is going to be placed. Downstream of the structure the number of cells decreases linearly. This way not only the computational costs are lowered but also the transmitted waves downstream are more diffused, and reflections from the relaxation zones are even less likely to occur. The mesh, already with the body there, is presented in Appendix A, Figure A.1.

Table 4.11: Wave parameters of the fully nonlinear regular wave, generated as a stream function.

f [Hz]	T [s]	H [m]	λ [m]	$\dfrac{d}{gT^2}$	$\dfrac{H}{gT^2}$	Fourier modes
0.83	1.2	0.04	2.23	0.063	0.00283	32
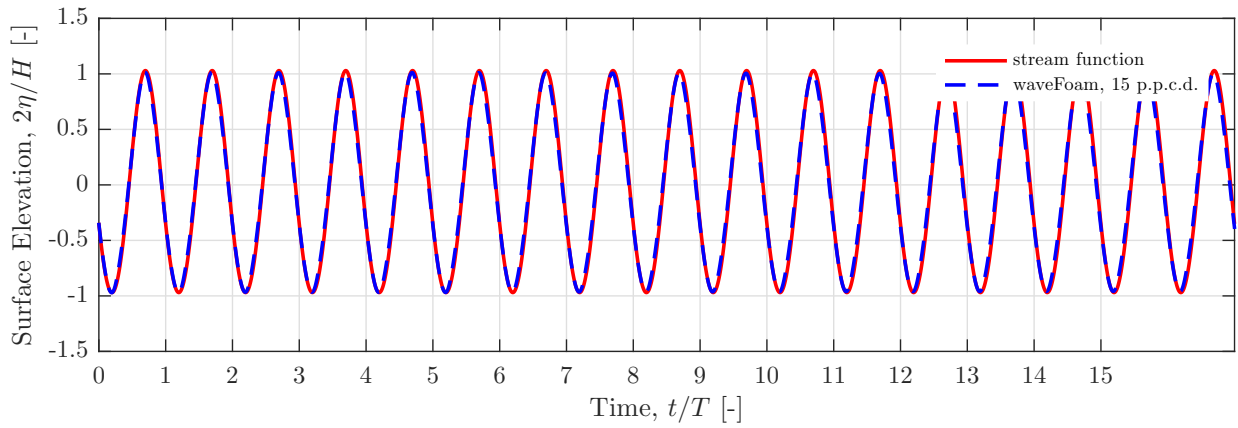
(a) Time series of the surface elevation at $x/D = 0$.
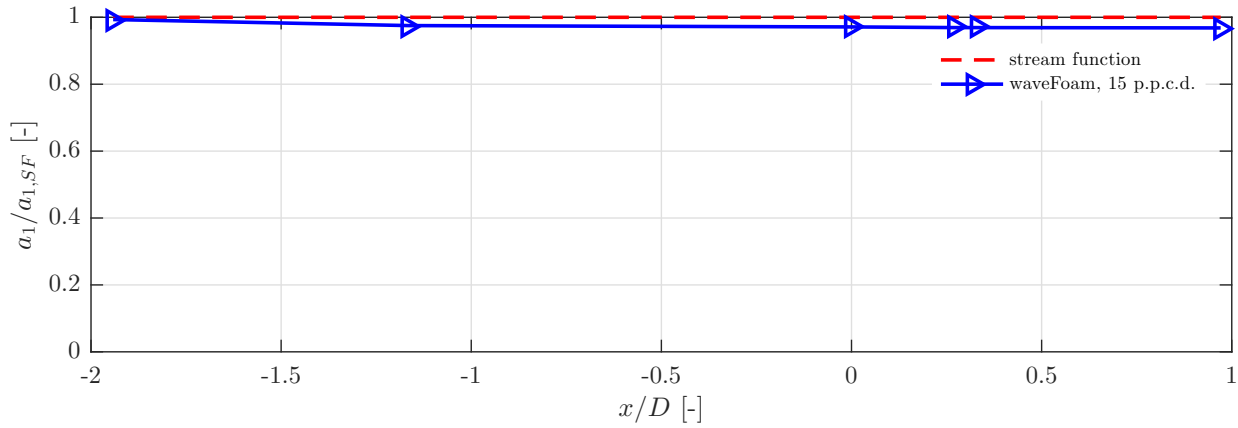
(b) First harmonic amplitude a_1, normalised by the first harmonic amplitude of the analytical solution $a_{1,SF}$.

Figure 4.16: Comparison of the numerical results using *waveFoam* and the analytical solution of the stream function. a_1 is the amplitude of the first harmonic component of the incoming wave, and $x/D = 0$ corresponds to the point where the *COG* of the cylinder is to be placed.

RESULTS AND ANALYSIS

Figure 4.17 presents the motions of the cylinder as a result of the incoming regular waves, shown for four wave periods, from the nineteenth one on. The previous ones are discarded to avoid the ramping-up of the wave, as well as the initial impact on the body. The results are presented for both stability methods for the pressure-velocity coupling algorithm presented in Chapter 3, namely the *acceleration-relaxation* and the *predictor-corrector* method.
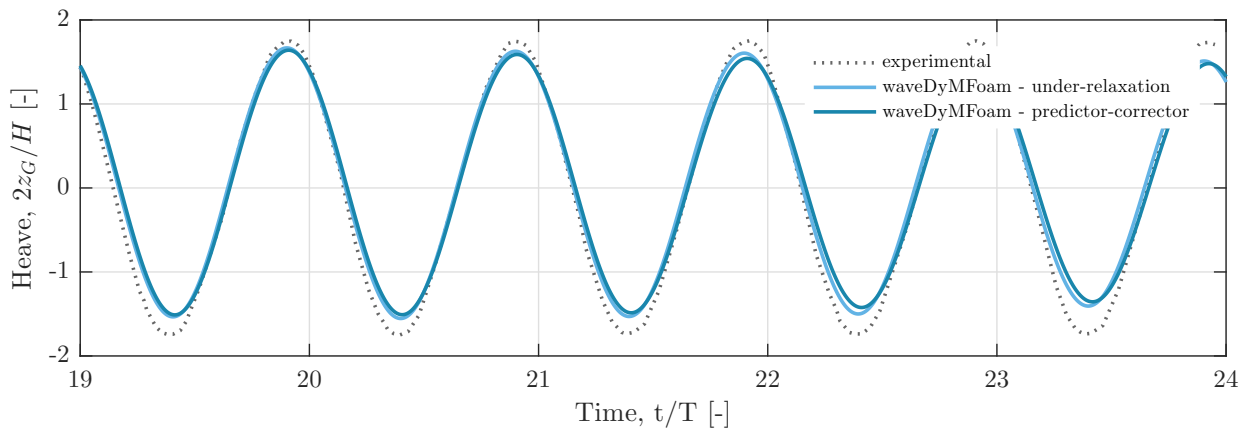
(a) Heave response.
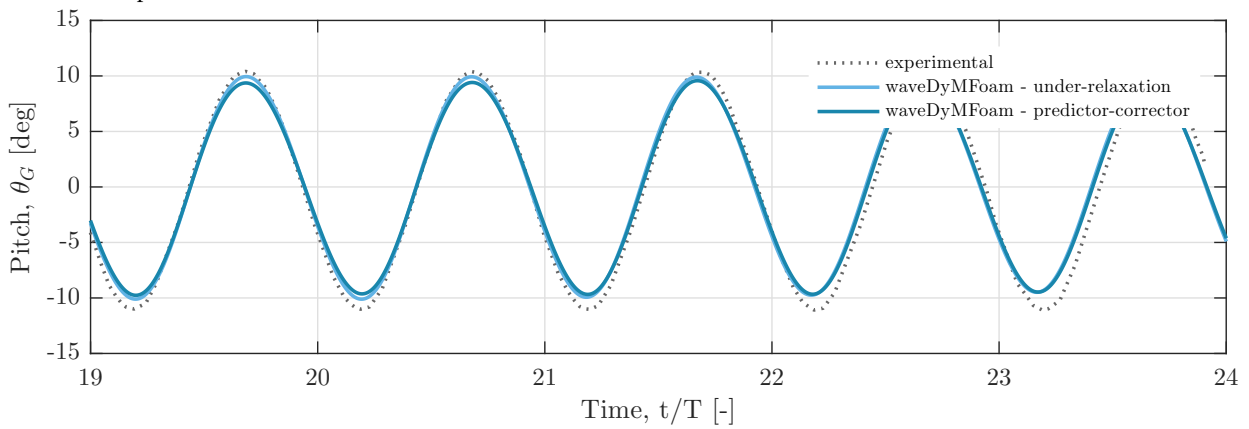
(b) Pitch response.
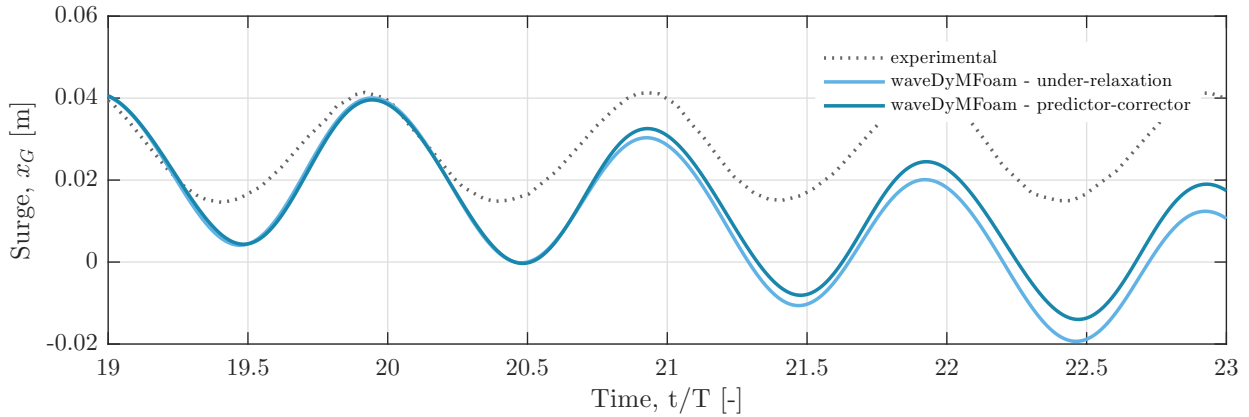
(c) Surge response.

Figure 4.17: Response of the floating cylinder due to an incoming regular wave. The heave is normalised by the wave amplitude. The time is normalised by the incoming wave period.

The experimental data provide the time series for the five periods here depicted. The heave and pitch response show good agreement for both stability methods, with a peak-to-peak error of less than 8% in heave and 9% in pitch. However, the response in surge shows a different behaviour. If a frequency analysis is done for the numerical time series, three clear components show up: the one corresponding to the main wave excitation frequency (around 1.2 s), the second one to the second harmonic of the wave (around 2.4 s) and the lowest one to the natural frequency in surge (around 9 s). The response in the frequency-domain is presented in Appendix A, Section A.1. The main frequency component, which corresponds to the first wave excitation frequency, is seen

to be in agreement with the experimental data, although the amplitude of the motion in the numerical model is a 17% larger. The *predictor-corrector* solution shows a lower error in amplitude. The lower component is not seen in the experimental data for the length of the time series shown. This is expected to be part of the transient response, but in the numerical results, it does not disappear completely, which may indicate that there is some excitation due to loading related to the combination of the first-order motion and the wave elevation exciting this lower component. The mean force is not captured either. Since the motion in surge is mainly governed by the restoring stiffness coming from the mooring lines, an analysis of the forces at the fairlead is done. These, together with the respective components, are presented in Appendix A, Figure A.4. The amplitude of the back mooring line total force from the experiments is seen to be very similar to the numerical ones, although the mean value of the experimental one is slightly lower. The front mooring lines force present a lower amplitude compared to the experimental data, which complies with the smaller amplitude of the main frequency component in the experimental data. In other words, the restoring response in the experiments to the wave excitation is larger, and therefore the motion in surge, smaller.

4.4. SUMMARY

This chapter presented an extensive validation of the fully nonlinear numerical wave tank for a 2D floating box and a 3D vertical floating cylinder. Both cases were compared to experimental data. For the 2D case, despite the difficulties encountered in the dynamic mesh implementation, the results were satisfactory. The 3D case also showed good agreement with the experimental data for the two vertical motions (heave and pitch), both for the decay tests and for the structure subjected to steep regular waves.

5

OC5-SEMISUBMERSIBLE CASE STUDY

5.1. INTRODUCTION

The Offshore Code Comparison, Collaboration, Continued, with Correlation (OC5) project is run under the International Energy Agency (IEA) Wind Research Task 30 and is focused on validating the tools used for modelling offshore wind systems through the comparison of simulated responses of several designs to physical test data. For Phase II of the project, numerical models of the DeepCwind floating semisubmersible wind system, such as the the nonlinear Navier-Stokes numerical wave tank in Bruinsma (2016), were validated using measurement data from a 1:50 scale test campaign performed at the MARIN offshore wave basin, as part of the *TO2 Floating Wind* project. The full-scale dimensions and structural properties of the OC5-semisubmersible concept can be consulted in Appendix B.

The following sections describe the modelling of the floating system within the two frameworks used throughout the current research, namely the fully nonlinear Navier-Stokes/VOF solver (referred to it as *(fully nonlinear) CFD model*, or when presenting the results as *waveDyMFoam*) and the diffraction solver. The latter is validated with respect to the former and the experimental data from the tests held at MARIN, in Section 5.4; it is done by comparing the unforced response of the structure in heave and pitch decay tests and to incoming regular waves to the corresponding experimental data or the CFD model results. The last part of the chapter compares the response of the structure in heave resonance conditions and steep waves of both numerical models. They are presented in Section 5.5 and 5.6. The structure of this chapter is depicted in Figure 5.1.
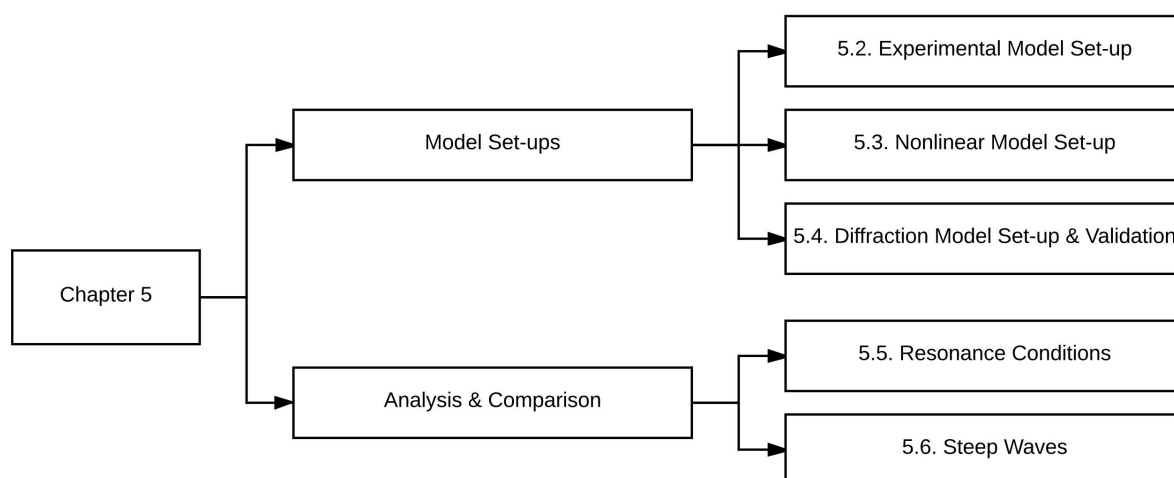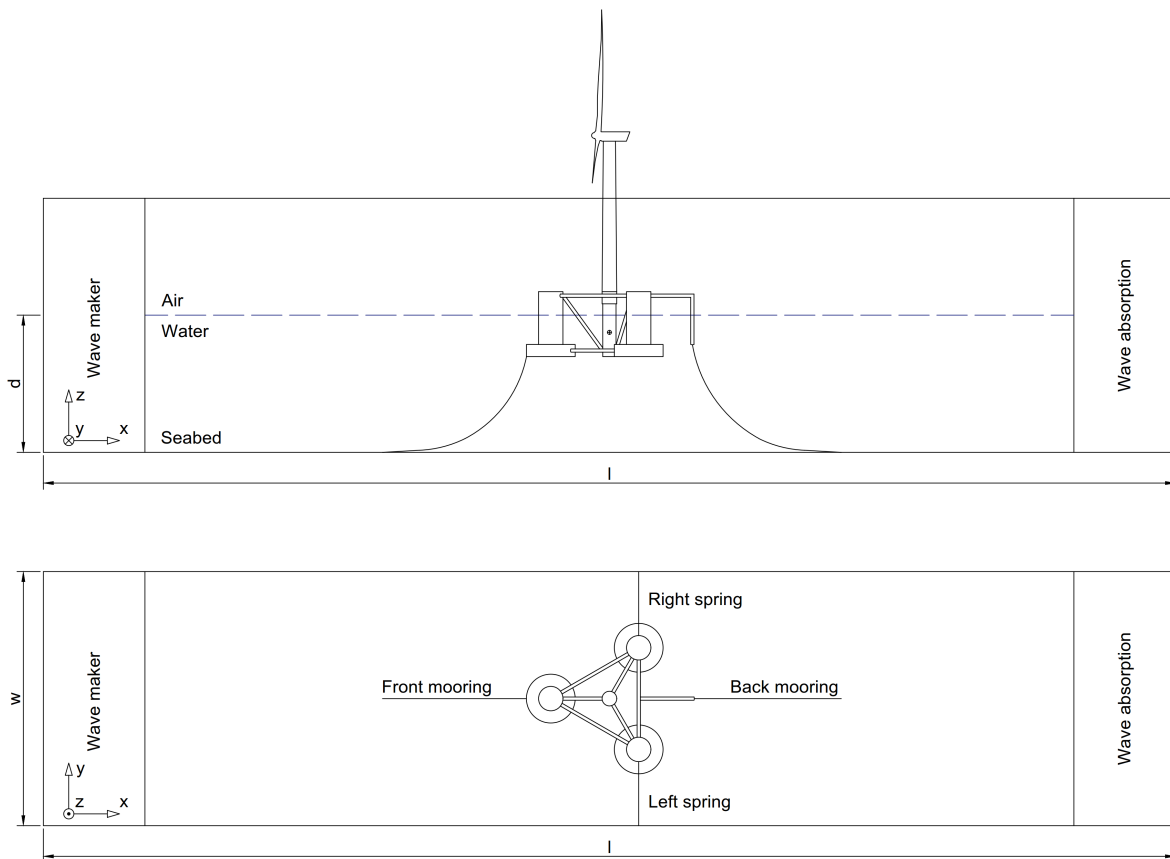

Figure 5.1: Scheme of Chapter 5 structure.

Figure 5.2: Schematic overview of the OC5-semisubmersible experimental set-up, including the mooring lines system. The total length l is 200 m, the width is 4 m and the water depth d is 4 m.

5.2. PHYSICAL EXPERIMENTS SET-UP

Within the *TO2 project* physical experiments were held at one of the wave tanks in MARIN to study the behaviour of the OC5-semisubmersible floating platform, at a 1:50 scale. The basin is equipped with a wave-maker and a wind field generator. The wave tank is depicted in Figure 5.2, where the OC5 is placed approximately at the centre. The down scaling is done based on the Froude number Fn. Since surface waves are gravity driven, equality in the Fn number ensures that the wave resistance and other wave forces are correctly scaled.

The original design of the OC5 has three catenary mooring lines anchored to the seabed and connected to the structure at the top of the heave plates. However, due to the limited extension of the wave tank, compared to the one that the original configuration of the mooring lines required, the mooring system had to be adapted. Therefore the mooring system was implemented as two moorings, one in the front and the other in the back, and two additional horizontal linear springs, as depicted in Figure 5.2. This way the restoring stiffness was approximately the same as the one of the original configuration. To get the right balance of the structure, an extension arm was constructed at the back part of the structure. All the attachment points, dimensions and properties of the mooring lines are given in Appendix B.

The experimental data used throughout the present work are the ones from the decay tests in still water and one of the four wave loading cases that were performed within the same test campaign.

5.3. NONLINEAR NUMERICAL MODEL SET-UP

The OC5-semisubmersible nonlinear numerical model was set-up by Niek Bruinsma (Researcher/advisor at Deltares) and presented in Bruinsma (2016), and in Figure 5.4b. Throughout the current work, the CFD model computations are slightly modified depending on the case.

The implementation of the mooring lines in the fully nonlinear CFD model is done quasi-statically, the same way as it is done in the 3D vertical floating cylinder validation case in Chapter 4. The position and the initial conditions of the mooring configuration of the experiments is precisely reproduced in the CFD model, as presented in Figure 5.3. The numerical domain is built as similar as possible to the experimental set-up, for the cases to be validated. The domain is rectangular, 6.4 m long and 4 m wide. The dimensions are indicated in Figure 5.3. The boundary conditions are the same as for the 3D validation case presented in Chapter 4, with the side walls being fully reflective. The total number of points was measured with respect to the main columns diameter, which yields 5 p.p.c.d. for the decay tests cases base mesh, and 10 p.p.c.d. for the incoming regular wave validation case. A multi-grading technique was used in the vertical direction, so that the majority of the cells are found at the free surface. On top of this base mesh, a refinement is completed around the structure with snappyHexMesh, as it was done for the 2D and 3D validation cases. The structure was modelled with an STL file, and exported to the numerical wave tank.
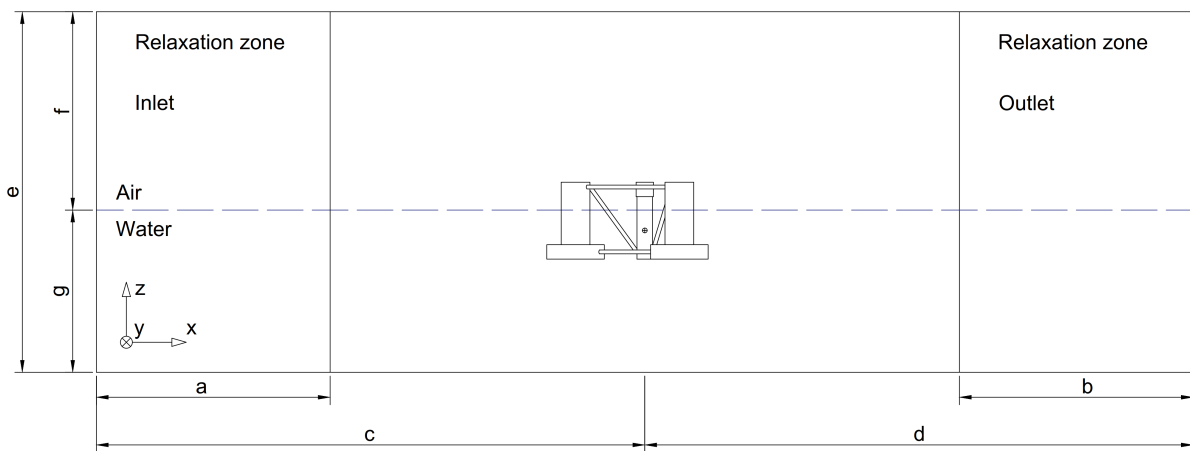

Figure 5.3: Overview of the OC5-semisubmersible numerical set-up, without moorings, for the validation cases against the experimental data. The dimensions, in model-scale, are denoted with letters, corresponding to: a = b = 0.7 m; c = d = 2.0 m; e = 5.2 m; f = 1.2 m; g = 4 m. The width is 4 m.

The numerical schemes and boundary conditions do not differ from the ones presented in Chapter 3, which were the same used for the 3D validation case presented in Chapter 4. Note that for the velocity-pressure coupling stability outer-correctors (*predictor-corrector* method) are used, instead of the *acceleration-relaxation* factor, except for the first of the validation cases, the free heave decay test, for which an acceleration-relaxation factor of 0.5 is applied.

5.4. DIFFRACTION NUMERICAL MODEL SET-UP AND VALIDATION

The diffraction model set-up is divided in two main steps. The first one deals with the discretisation of the model in panels, to carry out the frequency-domain analysis and obtain the velocity potential for each of the subproblems involved. The second one consists of the time-domain analysis using the obtained hydrodynamic properties. The description of these two steps is given in the following sections.

5.4.1. FREQUENCY-DOMAIN ANALYSIS. PANEL MODEL SET-UP

The frequency-domain analysis is done using the software tool supported by DNV-GL, found within the SESAM package. Firstly, GeniE is used to generate the mesh of the panel model, which includes the structure and the free surface to be implemented in Wadam, where the hydrodynamic properties are computed, based on the source-sink approach. The base model in GeniE comprises just half of the body, since symmetry can be applied with respect to the xz-plane. The panel model is depicted in Figure 5.4a. Note that the diffraction model presents full-scale dimensions.

(a) Panel model.   (b) CFD model.
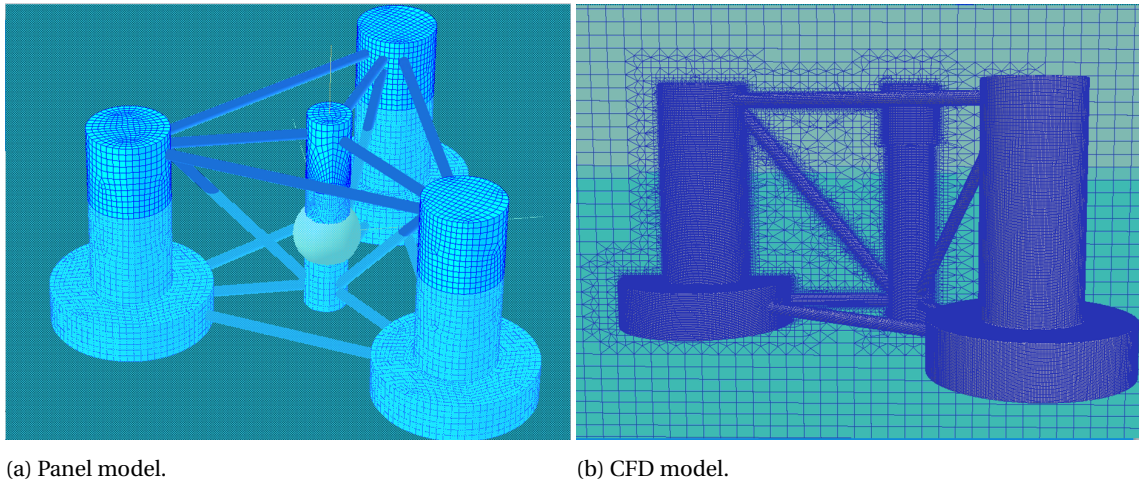
Figure 5.4: OC5 models with the two numerical frameworks used throughout this work. In the panel model, the main columns (MC), the central column (CC) and the heave plates (HP) are depicted in light blue. The braces, treated as slender elements are in dark blue.

The main columns and the heave plates are part of the panel model, whereas the braces are modelled as slender elements, so that Morison's equation is applied. The added mass and the damping coefficients are obtained for a set of frequencies within the wave excitation frequencies range, so from 0.3 to 1.5 rad/s. The wave incidence angle is 0°, i.e. waves propagate along the positive x-axis. The location of the centre of buoyancy z_B and the centre of gravity z_G are the same as if the whole system were there, and therefore the mass to be taken into account is the total one from the system.

To be consistent with the experiments and with the nonlinear model, the mooring lines effects are modelled by including an additional stiffness matrix for the hydrodynamic calculations. Note that this approach is static (and linear), as opposed to the quasi-static one applied in the nonlinear CFD model mooring system. The additional restoring stiffness matrix elements are calculated as presented in Appendix B, Section B.3.

The nonlinear viscous damping contribution from the main and slender members has to be accounted for in the frequency-domain analysis. The values are obtained from the experimental results computed by MARIN. The added mass from the slender elements is taken into account, although not their contribution to the quadratic drag since it is already accounted for it in the quadratic damping matrix. The values of this matrix are presented in Table B.6 in Appendix B. To prove that the model set-up during the frequency-domain analysis is well-established, the first-order response amplitude operator (RAO) is computed, and compared to the one from the numerical simulations and experiments completed at MARIN, as presented in Figure 5.5. The RAO calculated from the experiments, based on white-noise excitation, is presented in blue, whereas the one computed by the diffraction model established here is depicted in yellow. The one in red corresponds to the diffraction model computed by MARIN.
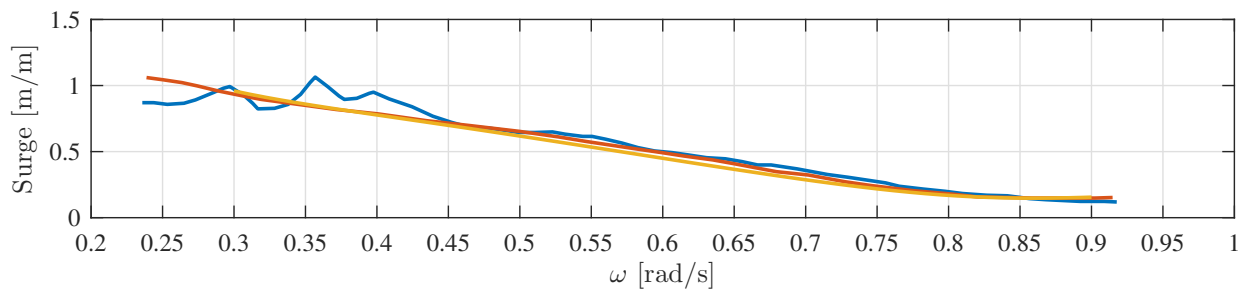
The response amplitude operator in surge is in good agreement with the numerical model from MARIN, quantitatively and qualitatively. However, none of these show the peak at 0.36 rad/s, which corresponds to the heave first natural frequency, meaning that they do not capture cross-coupling interactions. Despite this difference at this frequency, the tendency of the RAO is in agreement with the experimental data.

The response amplitude operator in heave is of greater interest, since its natural frequency lies in a region where the waves might present a high energy content, for instance, in swell sea-states. The first natural frequency of the structure in heave is at 0.36 rad/s, or at 17.5 s. Waves with this excitation frequency are considered to be in a long-wave regime. This implies that the radiation damping in this region is very low. Therefore, the type of damping that plays a role in the response is the quadratic one, which comes from viscous effects; this remarks the importance of properly adjusting these in the diffraction model. The amplitude of the motion at this region is decreased by adding heave plates. Their effect on the total response of the structure is seen in the RAO, not only at the natural frequency, but also at around 0.4 rad/s. The dip observed at this frequency in the numerical models is connected with cancellation effects in the excitation-force contribution in the potential-flow solution, which implies that at this frequency the only excitation forces are the wave induced drag ones. The cancellation frequency is given by:

$$\omega_c = \frac{\omega_{3,n}}{\sqrt{1 - \frac{z_m}{g}\omega_{3,n}^2}},$$

(5.1)

where z_m is the z-coordinate of the geometric centre of the heave plate, equal to 17 m in this case. The full derivation can be consulted in Faltinsen (1990). There is a difference of a 2% between the two numerical models. Since the panel model developed here shows the exact computed cancellation frequency, the difference is neglected. Note that for the rest of the frequencies the RAO is seen to be in agreement. In the time-domain simulations computed in this work, the additional quadratic drag of the heave plates is added explicitly, besides the additional one that accounts for the rest of the contribution of the elements to viscous effects.
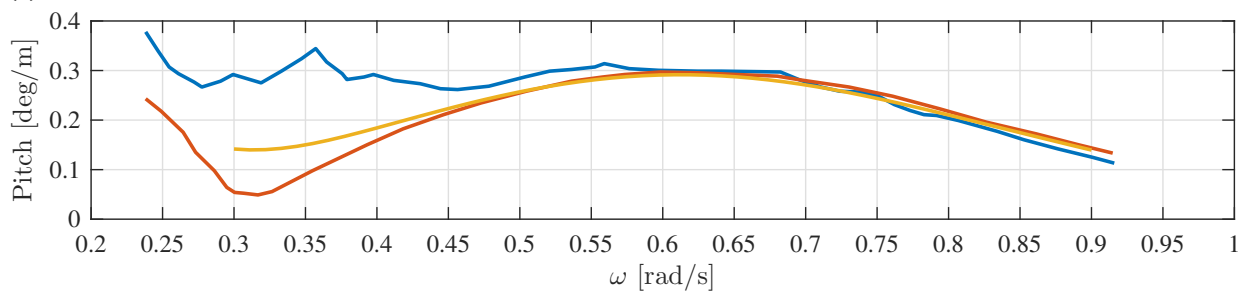
The pitch response amplitude operator for the current model is in agreement with the experimental one for higher frequencies. However, at the heave resonance region, the coupling between motions is not properly captured, and the response amplitude lies at half the value. It should be once again noted that it is very complicated to rigorously obtain the response amplitude operator at these low frequencies, in particular with the white-noise technique used for obtaining the RAO of the experimental model.

(a) Surge RAO.
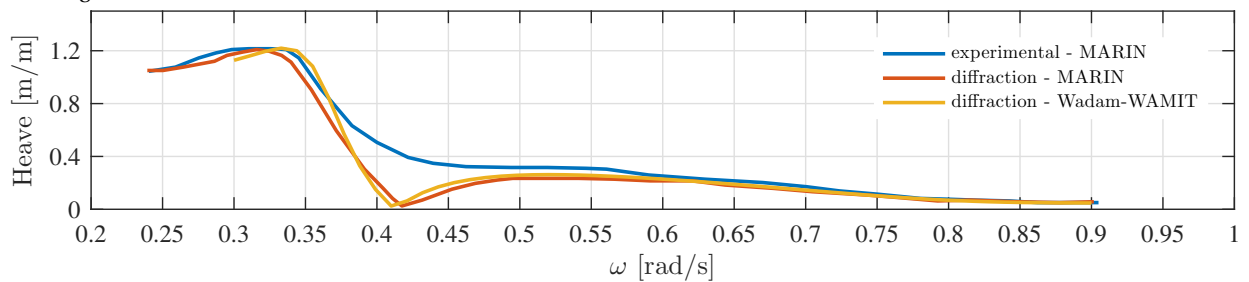
(b) Heave RAO.

(c) Pitch RAO.

Figure 5.5: Response amplitude operator in surge (a), heave (b) and pitch (c) of the experimental model (in blue), and the two potential flow based models computed at MARIN and within this thesis (in red and yellow), respectively.

SECOND-ORDER TRANSFER FUNCTION

In general, second-order effects are harder to estimate since they are typically small relative to the first-order contributions. In the current case irregular waves are not considered, and therefore difference- or sum-frequency

second-order effects coming from the wave frequency interactions are not likely to arise. However, as already presented in Chapter 3, other second-order effects, such as mean forces deriving from the second-order velocity potential, may be present. These are usually smaller than the ones coming from wave frequency interactions, but to account for them, the free surface is modelled in GeniE, and implemented in the frequency-domain calculations. Wadam only allows a maximum of 3000 panels in the base free-surface model, which consequently requires a thorough planning of the free-surface meshing. It has to be as fine as possible in the vicinities of the structure, but at the same time its radius R_m has to be sufficiently broad to capture all the free surface effects. According to Wadam user manual (Wadam (2010)), the radius of the free surface mesh has to be $R_m \approx O(H)$ in the case of shallow waters and $R_m \approx O(\lambda)$ for deep waters. In the present work the full-scale depth is 200 m, and therefore for waves shorter than 16 s approximately, deep water assumption applies. The mesh is finally chosen to have a radius R_m of 200 m, to apply a grid refinement closer to the structure, without exceeding 3000 panels. The final mesh has 2896 elements. Since there are no significant second-order effects in the simulations analysed here, the mesh is not presented in the main text, although it can be consulted in Appendix B, Figure B.5, together with the difference-frequency quadratic transfer function (QTF), based on Pinkster's theory, presented in Pinkster & Huijsmans (1982).

5.4.2. TIME-DOMAIN ANALYSES

To validate the diffraction model against the experiments and the CFD model, time-domain analyses, namely decay tests and tests in regular waves, are completed. For this purpose, the frequency dependent hydrodynamic properties are converted to the time-domain, using the retardation function, as presented in Chapter 3, Section 3.3.6. The linear damping values are the ones obtained from Wadam. Since the slender elements are not directly exported, their non-negligible effect to the added mass has to be accounted for. Furthermore, the additional contribution of the heave plates to the quadratic drag is explicitly included. A quadratic drag coefficient of 0.68 is applied, based on the reference model (Robertson et al. (2014)).

The heave free decay test is validated by comparing the results to the fully nonlinear CFD model, whereas the free pitch decay test is validated with respect to the experimental data. The moored decay tests and the test in regular waves of 12 s excitation period are validated for both the experiments and the CFD model.

HEAVE AND PITCH FREE DECAY TESTS

A free decay in heave is done for two different initial conditions. During the first test, the body is subjected to an initial displacement in heave of 1 m, whereas the initial displacement corresponding to the second test is of 6 m. Note that even though in the experiments the draft of the structure without the moorings is of 19.49 m, full-scale, the numerical equilibrium in the nonlinear CFD model is achieved at a draft of 20 m. This could be explained by a mismatch in mass of 193 tonnes in full-scale, or 1.5 kg in model-scale. Since the further steps of the validation are compared to this model, the draft taken into account is consistently chosen to be equal to this one. There are no experiments available for the free heave decay test, so the results are compared to the ones presented in Dunbar et al. (2015), where a CFD model of the OC5-semisubmersible, solved with a tightly-coupled version of the OpenFOAM® interDyMFoam solver, is compared to the time-domain solver FAST, from NREL. The time series for the free heave decay test is presented in Figure 5.6.

The diffraction model for the free floating structure is in good agreement with the other models regarding the natural period for both initial displacements. However, whereas the time series that correspond to an initial displacement of 1 m present similar amplitudes, the second initial displacement test time series show a clear discrepancy in amplitude during the first period. There is a good correspondence between the two CFD models and the two diffraction models. An explanation of this can be found in the way that the quadratic drag is tuned; it is adjusted based on a specific KC number, which is proportional to the maximum relative velocity. However, as shown in Figure 3.6a, the C_D is dependent on the KC number. In both tests, the velocity is different; this yields the difference in amplitude of the first period. During the following periods, the model computed with waveDyMFoam shows a higher damping than the tightly-coupled one, and closer to the two diffraction models. The damping in the SIMO diffraction model and the waveDyMFoam nonlinear model is compared using the corresponding linear and quadratic coefficients, based on the three first periods; these are presented in Table 5.1. Although research is ongoing regarding the calculation of the damping coefficients, with the method used here, usually applied in the industry, a good agreement in the quadratic damping coefficients is observed. The linear damping for the two initial displacements is different, although the values for both models are in agreement.
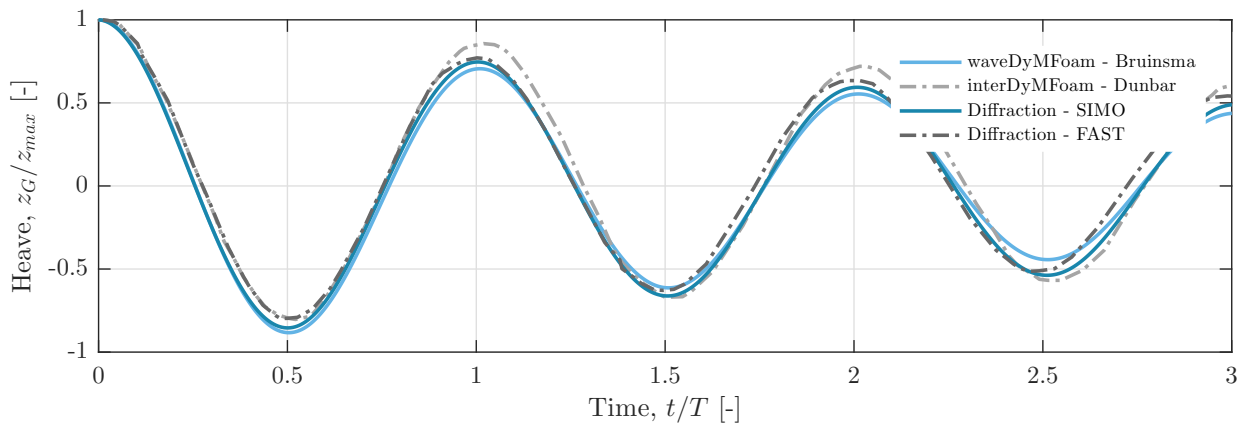
(a) Initial displacement of 1 m.
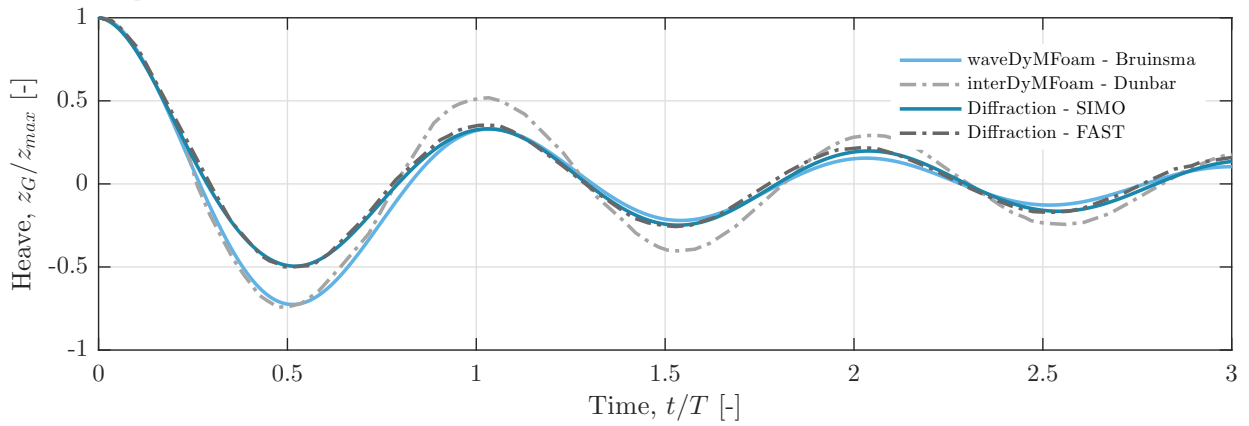
(b) Initial displacement of 6 m.

Figure 5.6: Free heave displacement of the *COG*. Both of them are normalised by the maximum displacement, equal to the initial one. The time is normalised by the natural heave period. The *waveDyMFoam* and *interDyMFoam* legend correspond to nonlinear numerical models, whereas *Diffraction* is referred to the time-domain simulations of the diffraction model, with the used tool indicated accordingly.

Table 5.1: Damping coefficients computed for the decay tests with different initial displacements.

	Initial displacement [m]	b_1 [m/s]	b_2 [1/m]
waveDyMFoam - CFD	1	0.004	0.16
	6	0.027	0.14
SIMO - diffraction	1	0.003	0.11
	6	0.017	0.10

Figure 5.7 presents the pitch response of the freely floating body, for both the experimental and the diffraction model. Since in this case the validation is made with respect to the former, the draft is 19.49 m. The structure is initially rotated 3.13° around the *y*-axis. The body is implemented with this initial rotation in the nonlinear numerical wave tank using an STL file, as it is previously done with the vertical floating cylinder during the 3D vertical floating cylinder validation case in Chapter 4.

The periods of both decay tests are calculated by applying a *fft*, since it yields more accurate results than the counting method, and in this case the sufficient length of the time-series allows this procedure. Table 5.2 presents the error in the period, which is seen to be less than 1% in heave, and almost non-existent in pitch. It can therefore be concluded that the free floating OC5-semisubmersible SIMO diffraction model without the moorings is properly adjusted with respect to the experimental data.
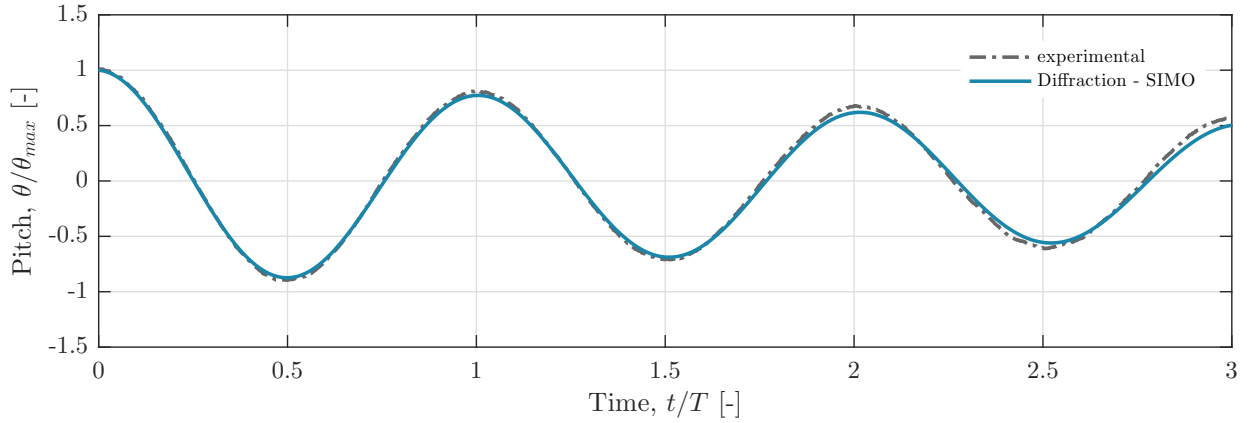
Figure 5.7: Free pitch decay test, normalised by the maximum rotation, equal to the initial one. The time is normalised by the experimental natural pitch period, 35.50 s.

Table 5.2: First natural periods in heave and in pitch for the unmoored floating body.

DOF	$T_{waveDyMFoam}/T_{exp}$[s]	T_{SIMO} [s]	ΔT [%]
Heave	17.50	17.57	0.39
Pitch	35.50	35.48	0.03

HEAVE AND PITCH MOORED DECAY TESTS

The mooring lines are implemented for the current case. A difference in draft of 0.543 m, measured in full-scale, is equally observed, which implies 2.75% increase with respect to the experimental one. The time series of the *COG* displacement in the heave decay test for the three models, with an initial displacement of 1 m, is presented in Figure 5.8a. The natural period is well captured in the diffraction model, as indicated in Table 5.3. However, the damping is higher from the second period on. It could be explained by the fact that low-frequency components show up if the entire experimental data time series is analysed for the 2000 s it lasts. One of the low-frequency components takes place at 81.5 s, which corresponds to the yaw natural frequency. However, this is not the only one, as shown in Figure B.7, in Appendix B. The source may be found on disturbances in the experiments, which may yield to excitation forces. Regardless, the numerical models show good correspondence.

The pitch unforced response of the diffraction model, together with the fully nonlinear CFD model response and the experimental data, is depicted in Figure 5.8b. The initial rotation angle in pitch is 3.34°. The natural period is in agreement with the CFD model, although it is shorter compared to the experimental data. The damping is also properly reproduced. From both the free and moored decay tests analyses and the calculated natural periods, presented in Table 5.3, it can be concluded that the diffraction model is able to reproduce the response of the floating platform for the different decay tests performed.

Table 5.3: First natural periods in heave and pitch for the moored floating body. Note that the one presented for the pitch corresponds to the one adjusted to the CFD model.

DOF	$T_{waveDyMFoam}$ [s]	T_{SIMO} [s]	ΔT [%]
Heave	17.48	17.46	0.11
Pitch	32.65	32.65	0.00
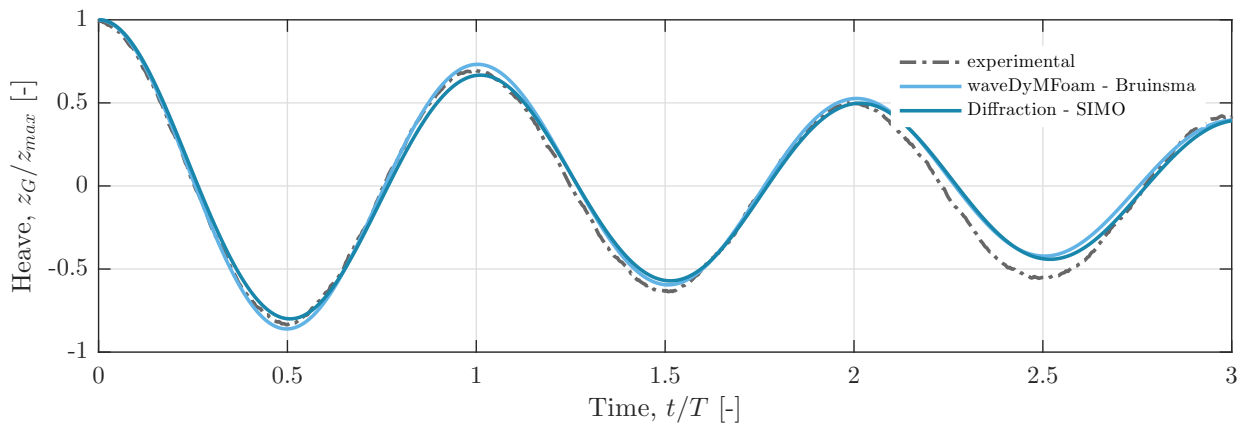
(a) Heave moored decay test. The time is normalised by the experimental model heave natural period, 17.5 s.
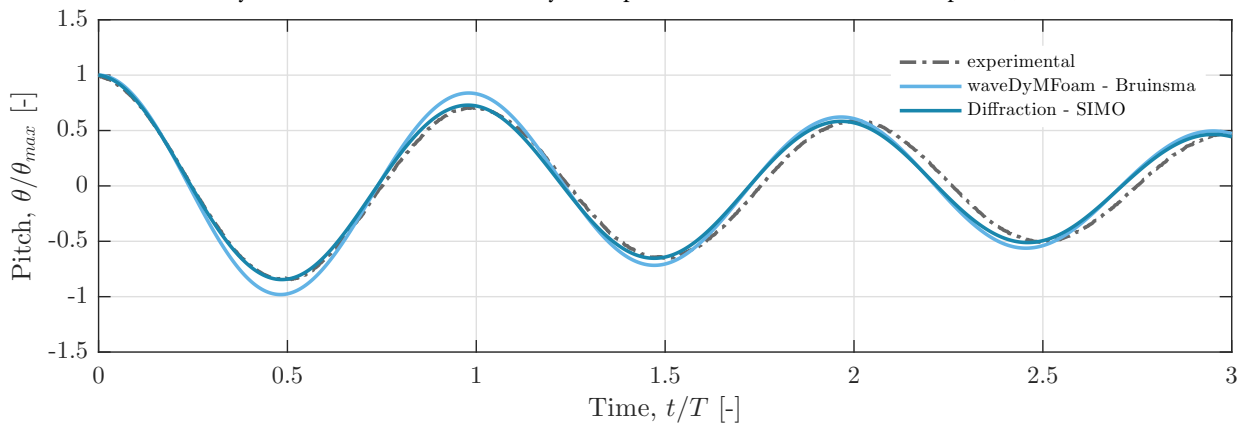
(b) Pitch moored decay test. The time is normalised by the experimental model heave natural period, 33.1 s.

Figure 5.8: Moored decay tests in heave and pitch. The displacements are normalised by the maximum initial values.

WAVE-STRUCTURE INTERACTION

Additionally to the validation of the diffraction model based on decay tests, the structure is subjected to a regular incoming wave whose characteristics are presented in Table 5.4. The results are compared against the corresponding experimental data and the CFD model response.

Table 5.4: Regular wave parameters.

f [Hz]	T [s]	H [m]	λ [m]	$\dfrac{d}{gT^2}$	$\dfrac{H}{gT^2}$	Wave theory CFD
0.08	12.1	7.1	231.0	0.139	0.005	Stream function

Before the structure is in the nonlinear numerical wave tank, the free surface elevation is measured at the same x-coordinate as where the *COG* of the body is to be placed. The distances to the wave generator are not the same as in the experimental model, as neither is the ramping-up time span. The domain dimensions are the same ones used for the decay tests, although this time the absorption relaxation zone is extended two meters, resulting in 4 m length, which corresponds to approximately one wave length. The absorption zone is imposed to be a potential current with zero velocity, i.e. still water. Table 5.5 presents the dimensions of the nonlinear numerical domain for this specific case, where the letters are indicated in Figure 5.3. The dimensions e, f and g, as well as the width, do not change. The total number of cells is 6 million, with 95 points per wave length.

The surface elevation amplitude, aligned with respect to the experimental data, is in good agreement with the experiments, although a higher crest and smoother trough start to be devised in the fully nonlinear CFD solution, since the wave is not linear anymore. The ramping-up process is depicted in the experimental data time series

Table 5.5: Dimension of the numerical set-up, with the letters referred to Figure 5.3, in wave lengths (w.l.).

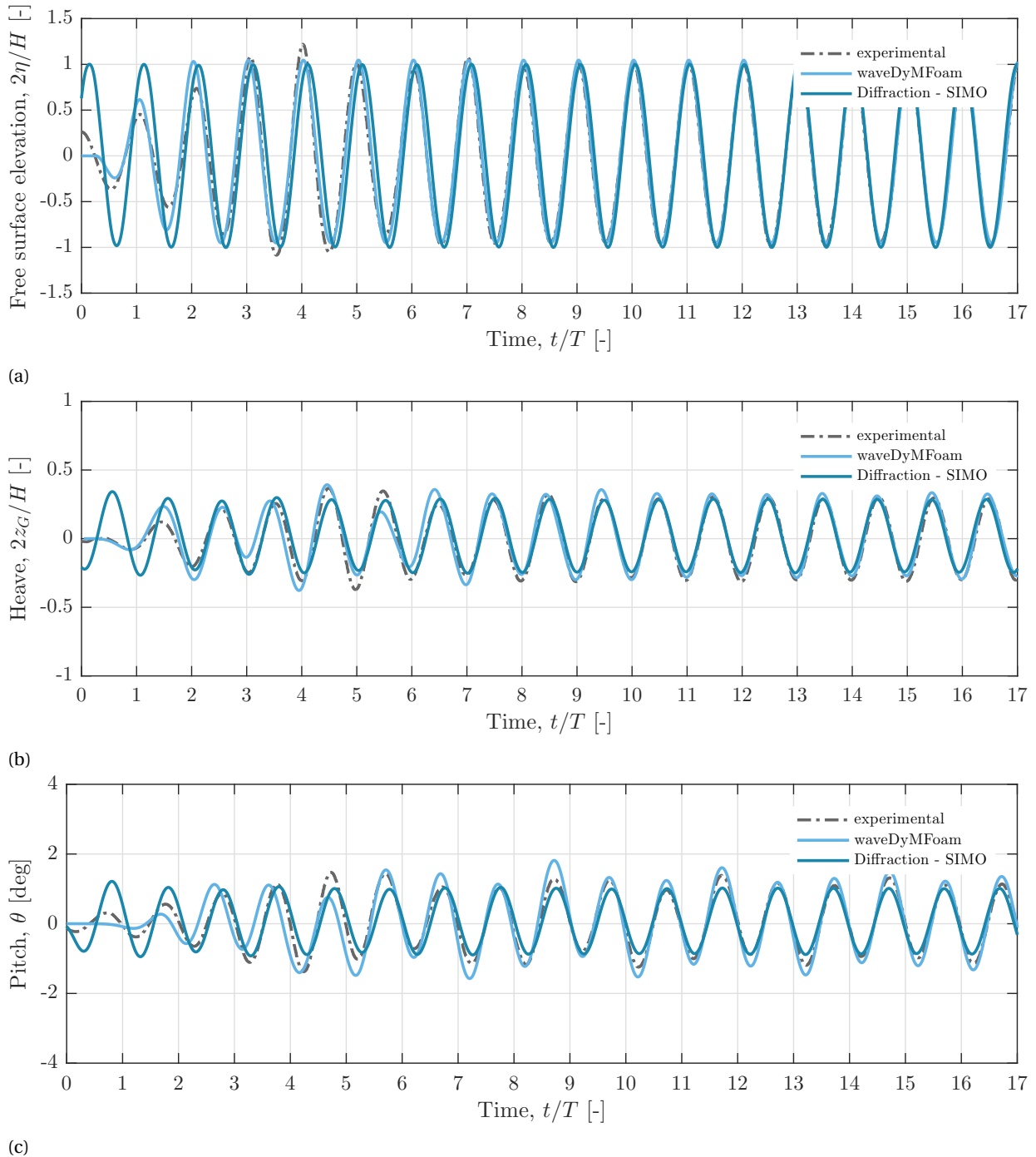|	a	b	c	d
(w.l.)	0.5	1.0	0.8	1.2

(a)

(b)

(c)

Figure 5.9: Free surface elevation measured right after the generation zone (a), heave (b) and pitch (b) response of the moored floating platform.

and in the CFD model response; in the former an overshooting of the wave elevation right after the fourth wave period is seen, which consequently increases the response in pitch and heave. Note that there is no ramping-

up of the wave in the diffraction model. If the surface elevation is analysed from the sixth wave period on, the amplitude complies with the experiments, for both of the numerical models.

The response of the diffraction model in heave amplitude matches both the experimental data and the nonlinear CFD model. A lower frequency component is identified in the latter at 36 s period, which indicates that the pitch is excited around its natural frequency by the third harmonic of the wave, and due to the coupling, it shows up in the heave response. Both responses present an almost negligible phase shift in heave with respect to the excitation one.

For the pitch response, a good agreement is observed with the experiments. Both the experimental data and the CFD model show again a lower frequency component at the same period as the response in heave, around the pitch natural frequency, which is excited by the third harmonic of the wave. The amplitude of heave and pitch responses of the diffraction model comply with the obtained RAO for the case of the experimental model data and the diffraction model computations, as seen in Table 5.6. As previously discussed, at this frequency range the effect of the heave plates is not as relevant as closer to the resonance region. In this table, *RAO experiment* and *RAO diffraction* indicate the ones experimentally obtained and from the frequency-domain analysis with Wadam, respectively. The *MARIN exp*, *waveDyMFoam* and *SIMO simul.* indicate the averaged amplitude oscillation at the main excitation frequency component, taking into account from the sixth period on of the time series presented in Figure 5.9. These amplitudes can be visualised in Figure 5.18 for an excitation frequency of 0.52 rad/s, with the results obtained for the fully nonlinear CFD model denoted with black stars, and the ones corresponding to the diffraction model, indicated by red triangles.

Table 5.6: Response amplitude in m/m for the different models at an excitation frequency of 0.52 rad/s.

DOF	RAO experiment	MARIN exp.	waveDyMFoam	RAO diffraction	SIMO simul.
Heave [m/m]	0.31	0.28	0.32	0.27	0.28
Pitch [deg/m]	0.29	0.32	0.35	0.26	0.31

5.5. RESPONSE IN HEAVE RESONANCE CONDITIONS

The natural frequencies of the semisubmersible floating platform treated here in pitch and roll are over 30 s. At these periods the wave energy is expected to be small, and therefore large resonant motions are not likely to take place in these modes. However, the heave natural frequency is lower than 20 s; waves with such long periods may be given after a storm generated far away. These periods may lead to the structure's excitation in heave. This section addresses the response of the floating platform in pitch and heave under these conditions. The incoming wave is defined by the parameters presented in Table 5.7. To estimate the length of the domain given such a large wave length, a propagation study of the wave without the presence of the structure at the numerical wave tank is done, to verify that no reflections from the boundaries take place. After several iterations, the minimum length of the numerical domain to avoid any disturbances results to be 22 m, with the absorption zone of at least one wave length long. Table 5.8 presents the dimensions of the nonlinear numerical domain for this specific case, where the letters are indicated in Figure 5.3. The dimensions e, f and g, as well as the width, do not change. In order to be as computationally efficient as possible, the same multi-grading meshing strategy as it was followed for the floating vertical cylinder subjected to waves is applied: from the wave generation zone up to 1.25 m downstream the body, the mesh cells present a constant aspect ratio equal to unity, with 100 points per wave length. This yields a numerical diffusion of less than 4% at the point where the structure will be placed, as seen in Figure 5.11. Downstream, the mesh is expanded linearly, so the further from the body, the larger Δx, as seen in Figure 5.10.

Table 5.7: Wave parameters of the fully nonlinear regular wave with a period close to heave resonance of the structure.

f [Hz]	T [s]	H [m]	λ [m]	$\dfrac{d}{gT^2}$	$\dfrac{H}{gT^2}$	Wave theory CFD
0.06	17.4	3.0	472.70	0.0673	0.001	Stream function

The response of the structure to the 17.4 s wave excitation period is presented in Figure 5.12. The undisturbed free surface elevation at the generation zone, as well as its phase, is seen to be in complete agreement for the two models.

Table 5.8: Dimension of the numerical set-up, with the letters as indicated in Figure 5.3, in wave lengths (w.l.).

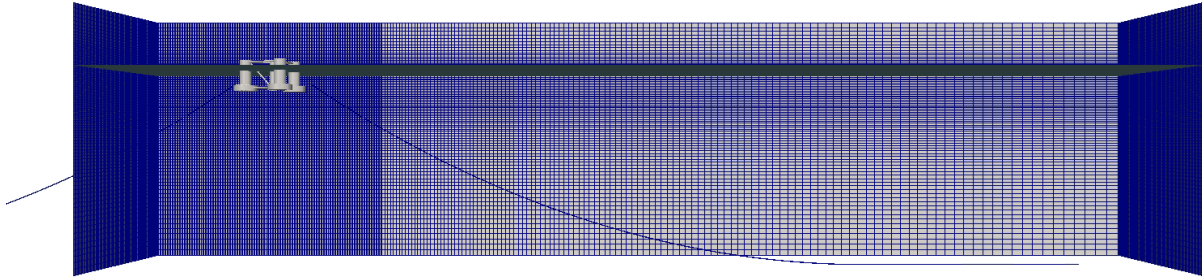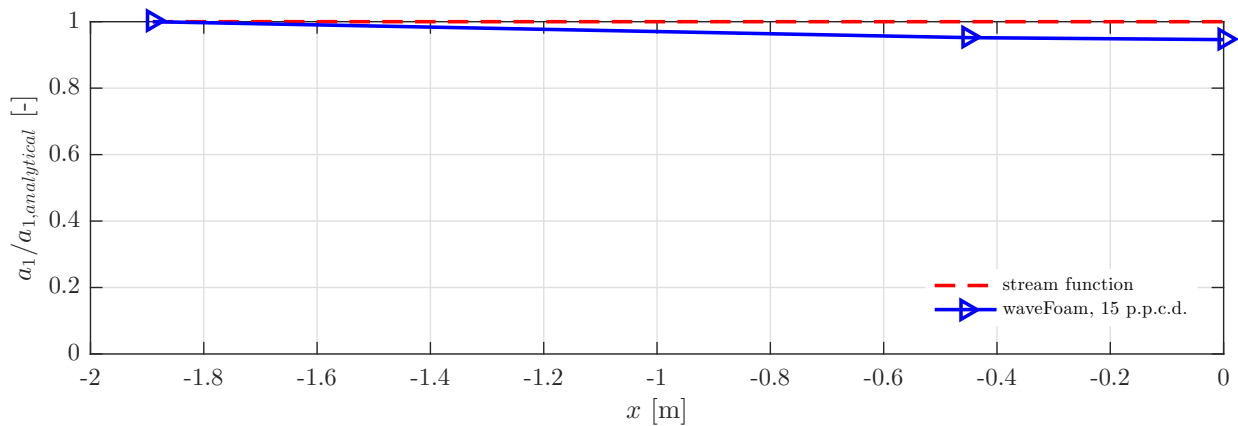|	a	b	c	d
(w.l.)	0.2	1.1	0.3	2.0

Figure 5.10: Background mesh of the resonance in heave conditions.

Figure 5.11: Comparison of the numerical free-surface elevation against the analytical solution given by the stream function. the horizontal coordinate is the distance to the first main column. a_1 is the amplitude of the first harmonic component of the incoming wave in the nonlinear CFD tank.

Due to the small potential damping given at this excitation frequency, the resonant motion is governed almost entirely by nonlinear drag forces on the platform. The amplitude of the CFD nonlinear model heave response is seen to increase up to the sixth period, from where it seems to reach a steady-state. The response of the diffraction model is 40% lower, although it complies with the RAO experimentally obtained, since the model was adjusted to this one. The vertical velocities are larger in these conditions, which has an effect on the KC and Re number, and therefore on the drag coefficient, as depicted in Figure 3.6a. Furthermore, the wave height affects the transfer function in heave, particularly close to resonance, as studied in Kirk (1985). Here the amplitude operator for semisubmersibles in resonant heave conditions, i.e. with excitation periods around 20 s, is expressed as a function of the wave height, and is also compared to the results for similar structures given in Paulling (1977), Kim & Chou (1972) and Clauss (1978). This does not directly imply that the diffraction model here developed is not able to capture the amplitude of the heave motion in resonance, but that the adjustment of the model for conditions close to resonance should be carefully done, and studied for different wave heights.

The response amplitude as computed here with the fully nonlinear CFD model is seen to be of almost 1.8 times the wave amplitude. Since waves with 17.4 s wave period may present large wave heights, other techniques to limit the motions at this frequency should be proposed. The response in pitch shows better agreement between the models; it also complies with the obtained RAO in pitch at this frequency, as seen in Figure 5.18b.
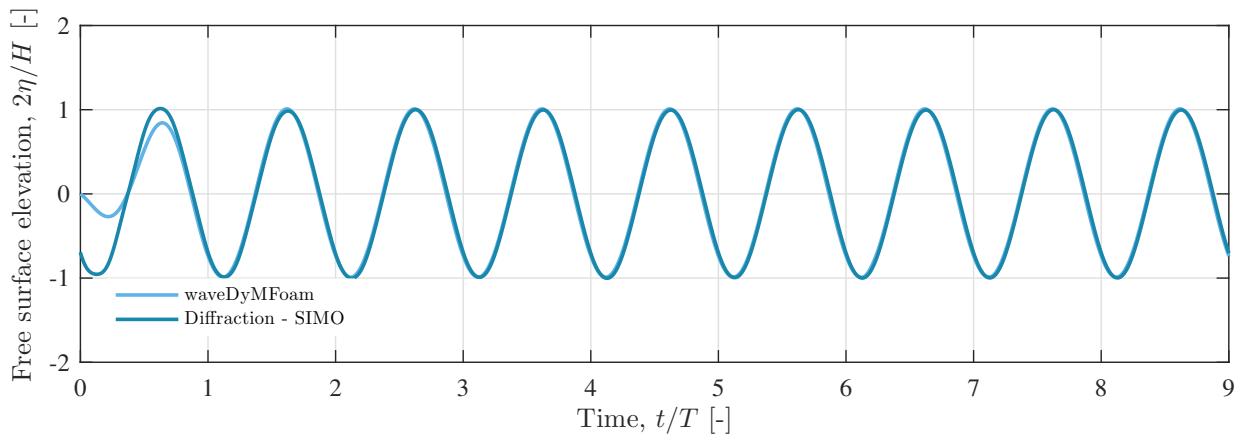
(a) Free surface elevation.
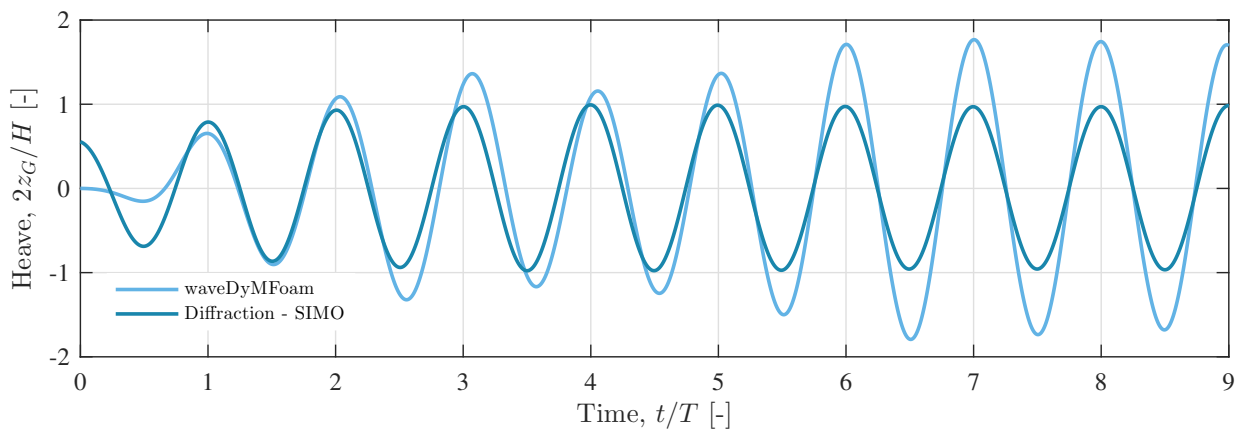
(b) Heave response.
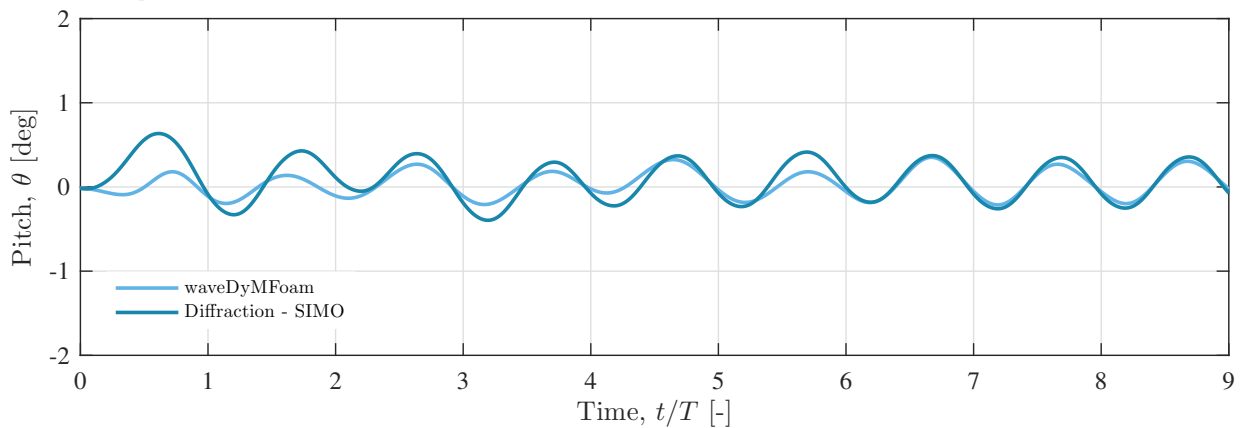
(c) Pitch response.

Figure 5.12: Free surface elevation (a), heave (b) and pitch (b) response of the moored floating platform.

5.6. Response to Waves Increasing in Steepness

To investigate the response of both numerical models to waves increasing in steepness, four waves are chosen based on the data in Li et al. (2013). The wave parameters are presented in Table 5.9. The maximum wave height is calculated with Equation 2.18, and the parameters according to the fully nonlinear stream theory (Fenton (1988)), for the CFD model. Note that for the sake of consistency the wave amplitude is considered to be $H/2$. The dimensions of the numerical set-up of the CFD model are the same ones as indicated in Figure 5.3. The number of points per wave length is 41 at the free surface for the four cases.

Table 5.9: Wave parameters of the fully nonlinear regular waves with increasing steepness.

H/H_{max} [-]	d [m]	H [m]	T [s]	λ [m]	D [m]	kA [-]	kd [-]	kD [-]
0.50	200	6.76	8	105.88	55.44	0.20	11.87	3.29
0.55	200	7.73	8	107.82	55.44	0.23	11.65	3.23
0.60	200	8.45	8	108.77	55.44	0.24	11.55	3.20
0.73	200	10.30	8	112.35	55.44	0.29	11.19	3.10

The free surface elevation of the undisturbed incident waves for the four cases, as generated in the nonlinear numerical wave tank, is presented in Figure 5.13, normalised by the water depth. The higher the steepness, the shorter the crest and the wider the trough.
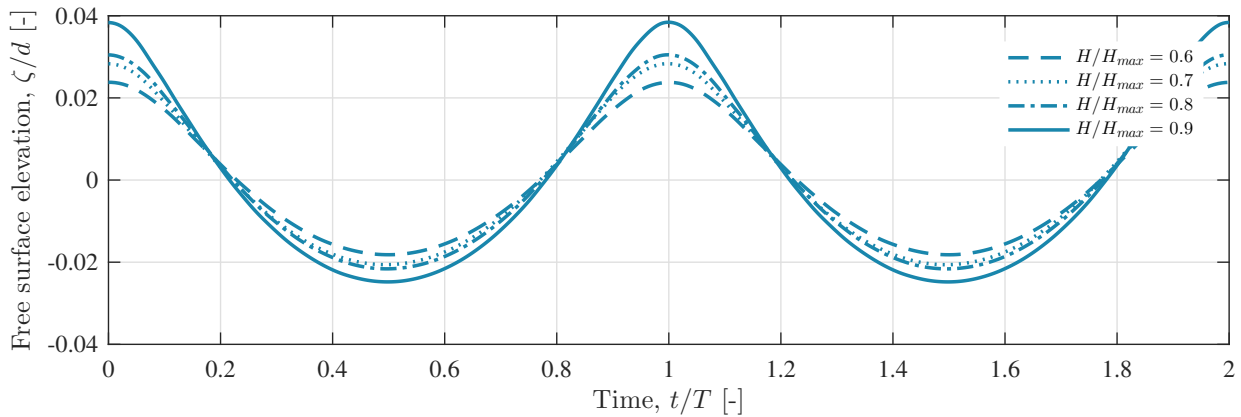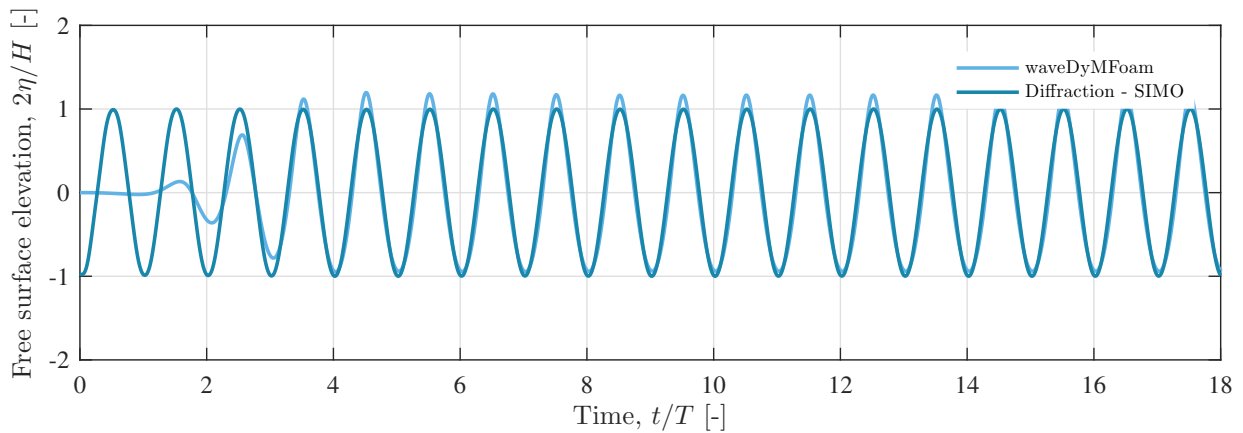

Figure 5.13: Surface elevation of the incident stream function waves, normalised by the water depth. Note that the crest is aligned to the first wave period, for visualisation purposes.

From the generation zone of the nonlinear numerical wave tank up to approximately 1 m upstream the *COG* (or 0.25 m upstream the front main column of the floater), the wave presents an 8% lower wave height, due to numerical diffusion. Therefore, for the sake of consistency in the comparison of the two numerical models, the same wave height is applied in the diffraction model. The ideal practice should be to avoid the numerical diffusion, but due to time restrictions and computational resources, the adopted approach is the most feasible one. The undisturbed free surface elevation in Figure 5.14a, measured 0.25 m upstream the *COG* of the structure, corresponds to an effective $H/H_{max} = 0.5$. The steeper waves, presented in Appendix B, Section B.7, correspond to effective incident wave heights of $H/H_{max} = 0.55$, $H/H_{max} = 0.60$ and $H/H_{max} = 0.73$, respectively, as presented in Table 5.9.

5.6.1. MOTIONS

The response in heave and pitch for an incident wave height of $H/H_{max} = 0.5$ is presented in Figure 5.14.
A transient response is observed up to the sixth period, from where steady-state is reached. The motions are very small compared to the incoming wave height. The response is inertia dominated, which implies that the drag forces do not play such an important role; furthermore, a shift in the response phase with respect to the incoming excitation one takes place. The nonlinearity of the wave is identified in the response in heave of the CFD model, which presents a slightly lower amplitude at the trough. The RAO values at this frequency (0.79 rad/s) are indicated in Figure 5.18: they are approximately 0.1. Note that this value is used just for reference purposes, since it is not certain that the number of waves at 8 s with the wave height used to compute the experimental RAO is enough to be able to directly compare the results obtained. The phase of the motions is well captured by both models. The mean difference in peak-to-peak amplitude, calculated based on the last ten periods, is presented in Table 5.10. The main difference in heave comes from the amplitude at the trough. Based on a frequency-domain analysis of the CFD model response, a lower frequency component is also observed in the pitch time series: the

one corresponding to the natural frequency in this same mode, which may be excited by the fourth harmonic of the wave. Even though its content in frequency is negligible with respect the three first ones, it may still be enough to excite the pitch around its natural frequency.

(a) Undisturbed free surface elevation 0.25 m upstream the structure, normalised by the incoming wave height.
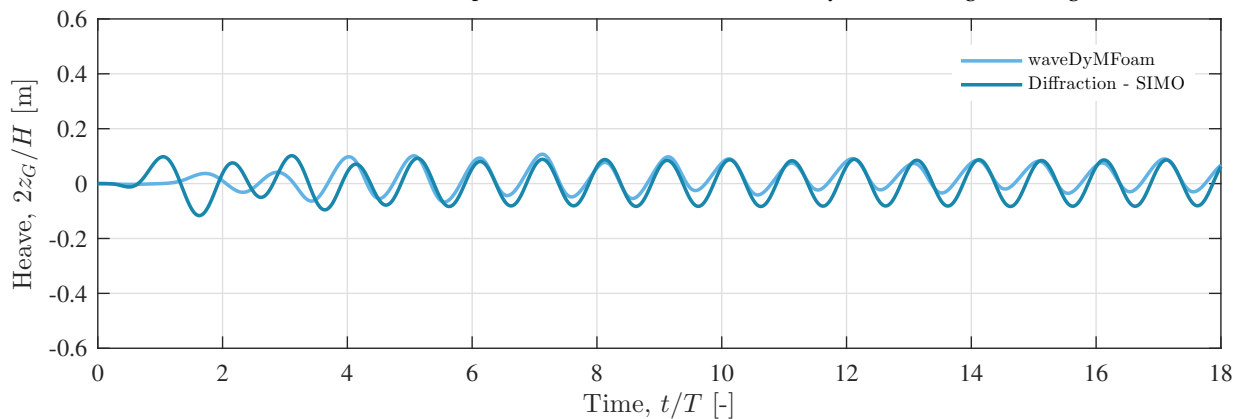
(b) Heave response of the *COG*, normalised by the incoming wave height.
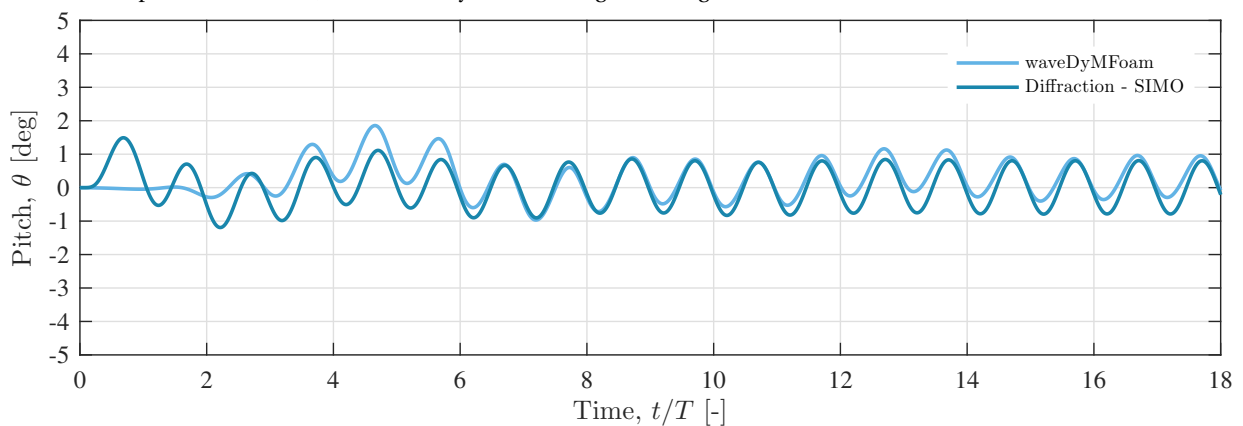
(c) Pitch response of the *COG*.

Figure 5.14: Free surface elevation (a), heave (b) and pitch (b) response of the moored floating platform. The time is normalised by the incoming wave period, 8 s.

For steeper wave conditions the results are presented in Appendix B, section B.7, Figures B.8 to B.10; they follow the same pattern as for the presented wave height. The response amplitude operator remains the same, so the responses increase with the wave height; the motions of the structure in heave are still small in absolute value, even for the steepest wave case. A wave height of $0.73 H_{max}$, with a crest elevation of 10.3 m, yields a heave crest

amplitude of approximately 0.5 m, according to both numerical models. Since the structure has a free-board of approximately 12 m, in principle no green water or downflooding is likely to occur. However, this is not the maximum wave height that can be given at these conditions, and therefore an analysis with larger wave heights is recommended. Figure 5.17 presents the snapshots for the two steepest waves. Although the wave run-up does not seem to have any contribution to the motions, this one should be considered for detailed design purposes of the structure, as discussed in the following section.

Table 5.10: Wave parameters of the fully nonlinear regular waves with increasing steepness.

DOF	$|\bar{x}_{i,diff}|$	$|\bar{x}_{i,CFD}|$	$\Delta|\bar{x}_i|$ [%]
Heave [m]	0.12	0.16	25
Pitch [deg]	1.25	1.6	22

5.6.2. HYDRODYNAMIC LOADS ON THE STRUCTURE

The total vertical and inline integrated hydrodynamic forces to which the structure is subjected are calculated for both models. Note that the overall response is inertia dominated. Prior to comparing the loads, the forcing computed with the diffraction model is decomposed into the excitation forces (F_{exc}), added mass, total damping and restoring forces (F_{am}, F_{damp} and F_{rest}, respectively). The linear and quadratic drag forces are not presented since the relative contribution is negligible. It is presented in Figure 5.15, for a wave with $H = 0.5H_{max}$. The vertical force main contribution comes from the added mass and from the excitation forces, whereas for the inline force the latter is the largest contributor.

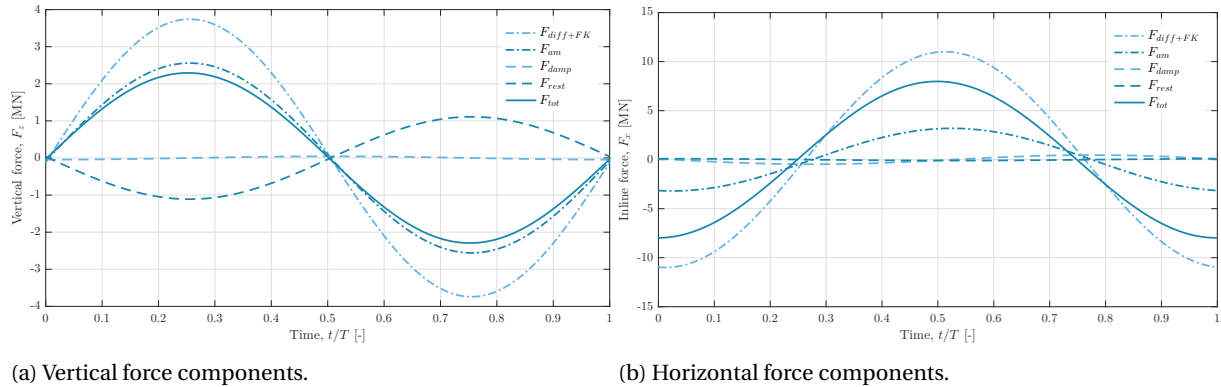(a) Vertical force components.   (b) Horizontal force components.

Figure 5.15: Force components of the total forcing on the structure computed with the diffraction model for a wave height of $0.5H_{max,break}$.

Both numerical models are compared in Figure 5.16 for one loading period. The forces are aligned to a zero-crossing at $t/T = 0.5$. The order of magnitude of the peak-force vertical component is very similar for both models, with a maximum difference in the steepest case of less than 14%. The difference at the crest and the trough is explained by the shape of the wave itself. The loading shape of the diffraction model corresponds to the first, linear, mode of the wave. However, the CFD model shows a different pattern. An initial analysis of this one, based on the observations, is done, supported by the snapshots for the two steepest waves-structure interaction in Figure 5.17 and in Figures B.11 and B.12, in Appendix B.

The general loading pattern for the three waves is very similar. The wave hits the main column at the front (at around $t/T = 0.21$ in Figure 5.17). Then the wave is diffracted, and right after passing the first column, and hitting the braces, it hits back the first column, after which it impacts at the other two main columns. At around $t/T = 0.55$ the vertical accelerations are zero at the main part of the body (central column and back main columns), whereas the horizontal ones are maximum at this same point. Once it has passed the whole body, the wave propagates upstream and impacts the two main columns at the back. Although the same loading sequence is observed for the three waves, the degree of steepness is seen to have an influence.
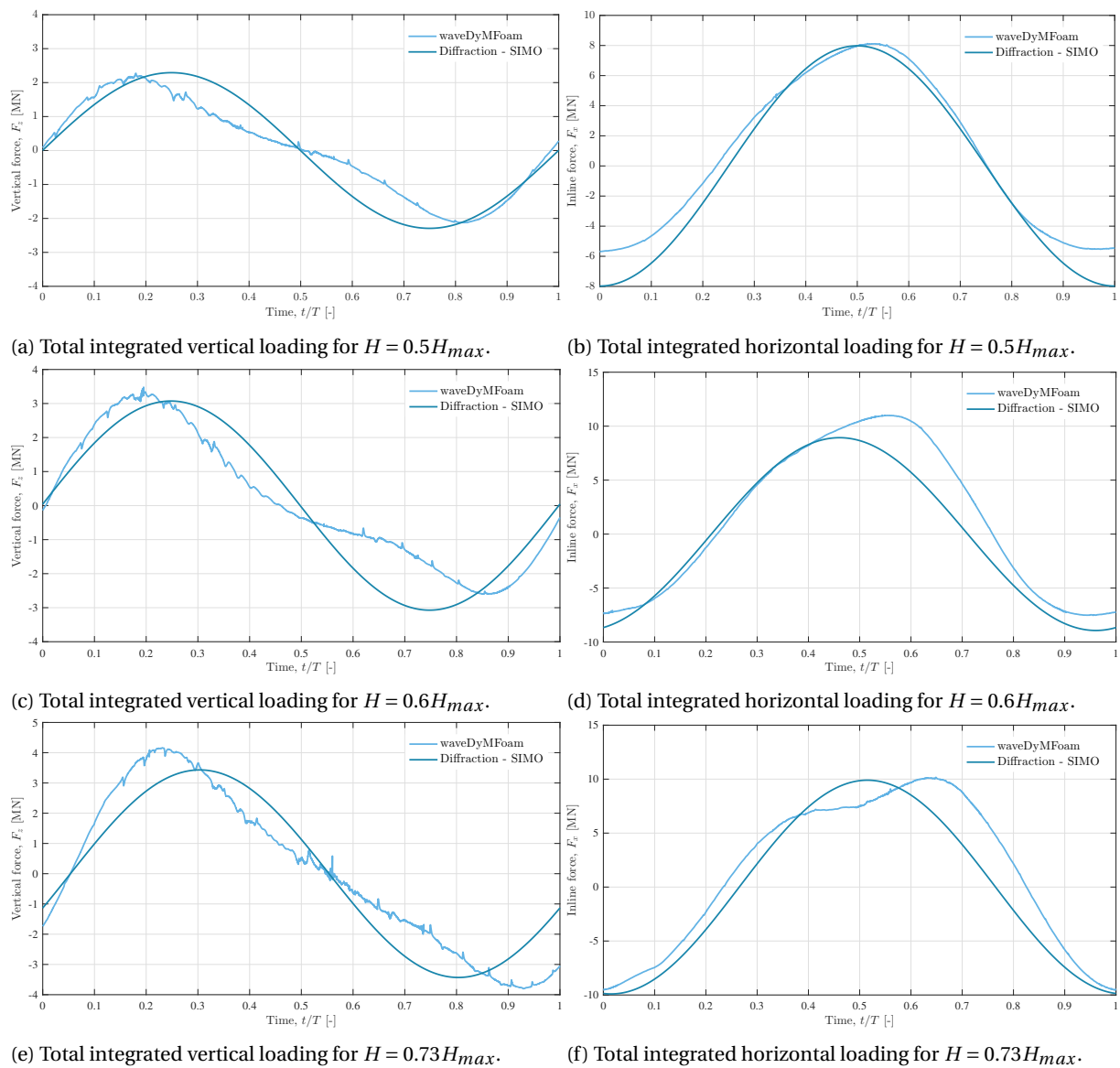
(a) Total integrated vertical loading for $H = 0.5H_{max}$.

(b) Total integrated horizontal loading for $H = 0.5H_{max}$.

(c) Total integrated vertical loading for $H = 0.6H_{max}$.

(d) Total integrated horizontal loading for $H = 0.6H_{max}$.

(e) Total integrated vertical loading for $H = 0.73H_{max}$.

(f) Total integrated horizontal loading for $H = 0.73H_{max}$.

Figure 5.16: Vertical and horizontal forcing.

From the frequency-domain analysis of the vertical loading it is seen that besides the main first wave harmonic component, there is a lower frequency component that coincides approximately with the heave natural frequency, at 17.8 s. The higher harmonics components of the wave, up to the sixth one, are also observed. The natural frequency of the structure in roll is at around 32 s, which implies that the fourth harmonic of the wave may excite it. For the inline force, the first four wave harmonics show up in the frequency-domain. This feature cannot be identified by means of the diffraction model.

The maximum values of the vertical force for the two steepest waves ($H = 0.73H_{max}$ and $H = 0.60H_{max}$) are given when the trough of the wave is hitting the main part of the body (central column and the two back main cylinders) at around $t/T = 0.20$. Note the delay in the structure's response to the two waves with different steepness. This can be explained by a larger displacement caused by a larger impact of the steepest wave, which causes the phase of the wave to arrive later to a same part of the body. Then the wave crest arrives at the main column and causes a local force (around $t/T = 0.37$); part of the wave is reflected back, and part diffracts and moves forward, and hits this first column at its back part, causing a local forcing at this point. This is followed by the impact of the wave crest at the main part of the structure, namely the central column and the two back main columns. The body has approximately half the diameter of the wave length, so when the crest hits the main body, the trough is

at the front column. Since the vertical accelerations are maximum in absolute value at the crest and the trough, when the maximum overall vertical loading takes place, so the trough is hitting the main part of the body, the crest is approximately at the first main column. From this point, the largest accelerations at the main part of the body start to decrease more slowly than the accelerations at the front main column increase, due to the shape of the wave. In the case with lower steepness, the accelerations at the front column increase with a lower gradient than for the steepest case ($H = 0.73H_{max}$); on the contrary, the accelerations at the main part of the structure decrease faster than for the steepest case. Consequently, the small dip before the zero-crossing of the loading is seen to be more pronounced for this case. The same is observed after the zero-crossing, where the positive accelerations taking place at the front main column in the less steep case make less negative the overall loading at this point. To better understand the different contributions of the elements involved and their interaction with the wave phase, and how the local effects influence the total vertical loading, a further study on the different elements of the structure should be completed.

The maximum horizontal force is given at $t/T = 0.69$ for $H = 0.73H_{max}$ and at $t/T = 0.59$ for the wave with $H = 0.60H_{max}$. The delay of the instants at which the maximum forces take place for both cases is seen in Figure 5.17, at $t/T = 0.55$. The maximum horizontal accelerations in absolute values are given at the zero-crossings of the wave. Right before the maximum load in the steepest case, a dip is observed. A possible explanation for it is the wider trough and its influence while the maximum accelerations are taking place at the main part of the body. There are larger negative gradients at the front main column than the positive gradients at the main part of the structure; the former will decrease the overall force, as seen where the dip is observed. For the wave with $H = 0.60H_{max}$, while the main part of the structure is being subjected to the acceleration previous to the largest ones, the front main column is also contributing to decreasing the overall force, but with lower negative gradients. Another remarkable factor that should be addressed is the heave plates interaction with the wave, which present a much larger diameter, and at the bottom of these the accelerations have still an important contribution. A thorough study of the different elements and their contribution to the overall horizontal loading should be completed.

(a) $H/H_{max} = 0.60$.
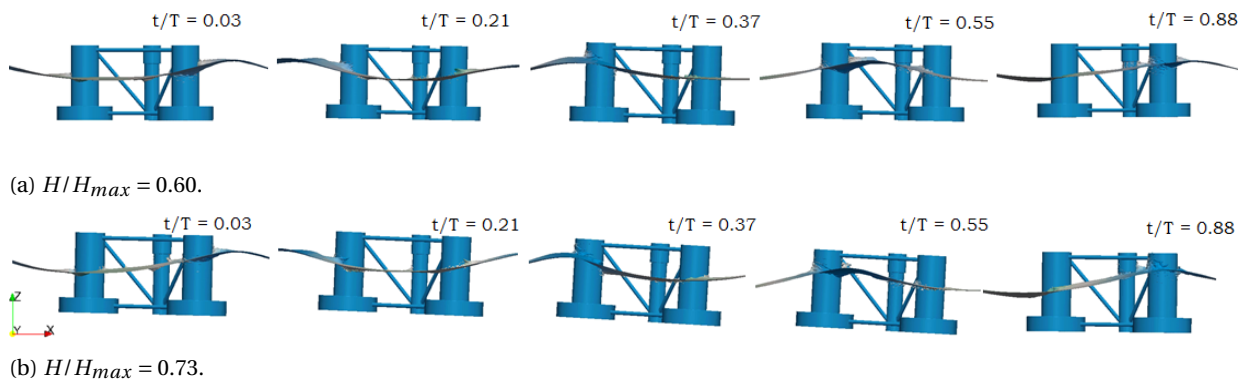

(b) $H/H_{max} = 0.73$.

Figure 5.17: Snapshots of the free surface elevation showing the passage of the steep wave. Note that the mooring lines are not visualised.

The purpose of this structure is to have a wind turbine mounted on top. This has been disregarded for the hydrodynamic study. The most relevant effect observed here is wave run-up. Maximum run-up levels determine the design of the platform. Furthermore, a good estimation of the wave run-up allows for an optimal location of the boat landing, ladder and door. Several studies concerning the effects of highly nonlinear waves have been done on semisubmersibles, such as the one reported in Paulling (2009), where wave run-up on the platform columns and fluid pressures at various locations are calculated with a Navier-Stokes/VOF solver and verified against experiments. These are proven to be underestimated by linear theory, as reported in Martin et al. (2001), where an experimental investigation of wave run-up on columns was conducted on semisubmersibles in steep regular waves. L. Vos (2007) developed and validated a semi-empirical approach to predict wave run-up, based on a small-scale experimental study that examined both regular and irregular wave run-up cylindrical and conical pile foundations.

5.7. SUMMARY

Throughout this chapter firstly a validation of the OC5-semisubmersible diffraction model against 1:50 scale experimental data and fully nonlinear CFD model was done, based on free and moored decay tests in pitch and heave and on a wave-structure interaction case. The diffraction model showed to be properly adjusted with respect to both the experimental and the fully nonlinear numerical models. Since some discrepancies were observed between the CFD and the experimental model, the diffraction model was adjusted with a focus on the former, given that the cases to be analysed at a latter stage were compared to this one. The wave-structure interaction validation case (waves at ω =0.56 rad/s) shows a good correspondence of the experiments and the two numerical models, both for pitch and heave, as it can be inferred from the summarising Figure 5.18, where all the amplitude responses for different excitation frequencies are presented.

Secondly, the structure was subjected to a regular incoming wave with a period equal to the heave natural one (at ω =0.36 rad/s). The amplitude in heave of the response of the diffraction model was seen to be 40% lower, although it complies with the RAO experimentally obtained, as seen in Figure 5.18a, since the model was adjusted to this one. However, as the transfer function at this region depends on the wave height, the diffraction should be adjusted accordingly, not only with different wave heights, but concerning the drag coefficient, dependent on the KC and Re numbers. The amplitude of the response in pitch is the same for both numerical models.

Lastly, the wave-structure interaction for three regular waves with the same frequency (at ω =0.79 rad/s), but increasing in wave height, or in steepness, was studied. The response in motion of the diffraction model was seen to be very similar to the CFD model, although the difference in the trough amplitude due to the nonlinearity of the wave led to a larger error, as it can also be depicted from Figure 5.18. From this figure, it is seen that the diffraction model complies with the calculated and experimental RAO. However, at this region, with such wave height, the task of obtaining an accurate RAO based on the white-noise technique is not trivial. Furthermore, linear wave theory did not apply in this case. The vertical and inline loads on the structure were also presented. A good agreement between both models is seen in terms of the total integrated peak forces, both vertical and inline. However, the loading pattern, as well as the visualisation of the structure subjected to waves, indicate that the diffraction model does not capture other phenomena, such as wave run-up, resulting from waves with high nonlinearities.
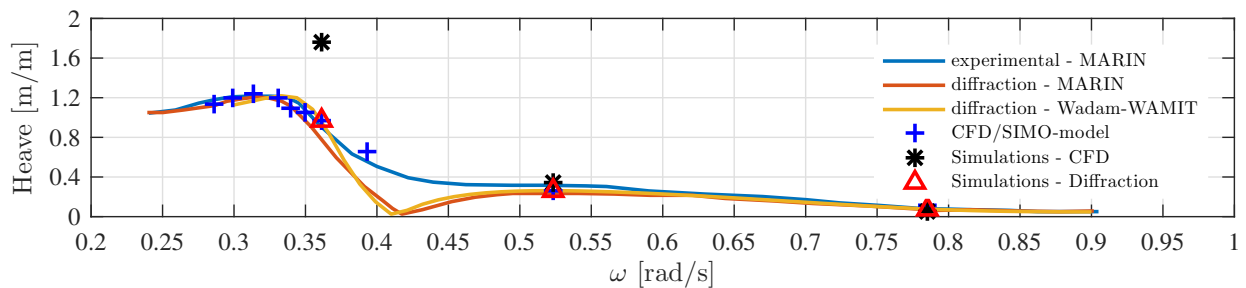
(a) Heave.
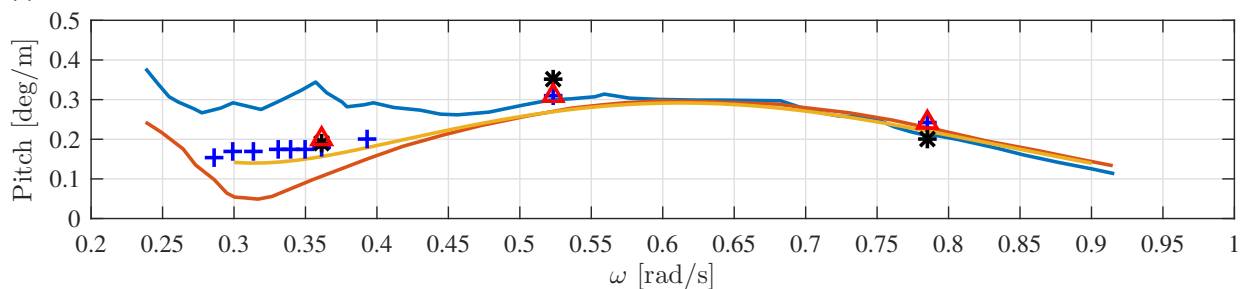
(b) Pitch.

Figure 5.18: In blue, the RAO obtained from the experiments at MARIN, based on white-noise technique; in red the one obtained from the diffraction model developed at MARIN. In yellow, the RAO computed with Wadam, reproducing the model from the experiments. The blue crosses correspond to the model in SIMO, but reproducing identically the CFD model. The black stars correspond to the RAO based on the simulations with OpenFOAM®. The red triangles is the RAO based on the same simulations with SIMO, based on the nonlinear numerical model.

6

CONCLUSIONS AND FURTHER RESEARCH

In this thesis, the response of three different floating structures to nonlinear wave loading is investigated using a fully nonlinear Navier-Stokes/VOF solver (in the following referred to as *fully nonlinear CFD model*). The third of the structures, the OC5-semisubmersible floating platform, is also studied with a second-order potential flow theory solver (in the following referred to as *diffraction model*).

First, the fully nonlinear Navier-Stokes/VOF numerical wave tank, developed within the open-source CFD toolbox OpenFOAM® framework (version 1606+), is validated against experimental data that include the response of a 2D floating box and a 3D floating vertical cylinder. To model the motions of the floating structures and the generation and absorption of waves, the interDyMFoam solver, provided by the OpenFOAM® library, is extended with the waveFoam package, developed by Jacobsen et al. (2012). Furthermore, a simple catenary mooring line, developed by Niels G. Jacobsen (Deltares), is implemented for the moored cases. The OC5-semisubmersible floating platform study is also completed in this numerical wave tank.

Second, a potential flow theory based model of the OC5-semisubmersible floating platform is generated. The frequency-domain analysis is done with the Wadam software and the time-domain simulations with SIMO. Both tools are commercial software found within the SESAM package by DNV-GL. The diffraction model is validated against the experimental data and the fully nonlinear CFD solver described above.

Lastly, both numerical approaches are compared to assess their suitability for modelling two different conditions where nonlinearities are of relevance: heave resonance conditions and regular waves with increasing steepness. A discussion of the results and conclusions, followed by recommended further research, are presented in the following sections.

6.1. DISCUSSION

To answer the main research question, presented in Chapter 1, three sub-questions are addressed. The first one is covered in Chapter 4, whereas the answer to the second and third sub-questions are presented within Chapter 5. The discussion of these is provided below.

- *Is the nonlinear numerical wave tank capable of predicting the motions and capturing the nonlinearities of floating bodies subjected to steep regular waves?*

  This sub-question is answered in two parts, corresponding to the two validation cases (floating box in a 2D domain and vertical floating cylinder in a 3D domain) treated here to assess the fully nonlinear CFD numerical wave tank capability for predicting the motions and capturing the nonlinearities:

  – **2D floating box**: this case is run in a 2D numerical domain. Physically, it implies that the body has three degrees of freedom, namely heave, roll and sway. Numerically, it means that the Navier-Stokes equations are not solved in the third dimension. A roll decay test is performed to obtain the natural period and the damping coefficients for different mesh refinements. The results are seen to converge to a solution which is in agreement with the experimental data presented in Ming et al. (2014), both in natural period and in the computed damping. Prior to subjecting the structure to incoming waves, a

wave propagation convergence study is done and a wave-structure interaction case is also computed and compared to the experimental data. Despite the difficulties encountered in the dynamic mesh capabilities, the numerical wave tank is validated for this 2D case, as proven in Section 4.2.

– **3D floating vertical cylinder**: this case considers a cylinder allowed to rotate and translate in six degrees of freedom. The results of the different tests computed in this part are validated against experimental data from Palm et al. (2016). Firstly, heave and pitch free decay tests are done, to compare the unforced response of the body, and to compute the degree of linear and nonlinear damping. The heave decay test is in agreement with the experimental data, whereas the pitch response shows discrepancies. These are not due to the model itself, but due to inaccuracies when measuring these in the experimental model and to the sensitivity of the response to changes in the structural properties, as proven in Section 4.3. Furthermore, the fully nonlinear CFD solver is capable of capturing an instability arising from the transfer of energy between heave and pitch, known as Mathieu instability. Secondly, moored decay tests are carried out for the same configuration. The response of the structure with the mooring lines implementation does not show different results compared to the free decay tests. Lastly, the moored vertical cylinder is subjected to incoming steep regular waves. The structural response is in agreement with the experimental data for both heave and pitch, although not for surge. Given this mismatch between the fully nonlinear numerical model and the experimental results, a study with a different stability method for the velocity-pressure coupling is executed. This modification yields a better agreement between the numerical and the experimental data, although the difference is still considerable. The forces on the fairlead of the cylinder are also computed, to verify that these are in agreement with the experimental data. The mean value of the front fairleads is properly captured, although the amplitude is underestimated by the CFD model. The mean value at the back mooring is underestimated, although the amplitude is in good agreement. A possible reason may lie on the use of a quasi-static model of the mooring lines, instead of a dynamic one. Despite these differences, the phase of the response, as well as the amplitude of the system, is well predicted.

Based on the analysis of the previously discussed results, it can be stated that the fully nonlinear Navier-Stokes solver is capable of predicting the motions and capturing the nonlinearities involved in both cases.

• *How does the motion of a semisubmersible floating platform under heave resonance conditions computed by both numerical models compare?*

Prior to addressing this sub-question, the OC5-semisubmersible diffraction model is built, as described in Section 5.4. A frequency-domain analysis is done for obtaining the frequency-dependent hydrodynamic properties of the floating structure, including the response amplitude operators (RAO). The nonlinear damping is adjusted based on the experimental data from MARIN. To validate the diffraction model against the experimental results and the fully nonlinear numerical model first heave and pitch decays are performed, after which the floating structure is subjected to linear regular waves. The diffraction model is proven to be capable of reproducing the experimental data, as well as the fully nonlinear CFD model response.

At the next stage the structure is subjected to incoming regular waves with a period of 17.4 s, i.e. right at the heave resonance one. Due to the small potential damping given at this excitation frequency, the resonant motion is governed by nonlinear drag forces on the floating platform. The amplitude of the fully nonlinear CFD model steady-state response in heave is 40% higher. The response of the diffraction model complies with the RAO experimentally obtained, since the model was adjusted to this one. However, the vertical velocities are larger in these conditions; these affect the KC and Re number which inherently influence the drag coefficient.

Furthermore, as proven by Paulling (1977), the wave height has an effect on the transfer function in heave, particularly close to resonance, so the RAO should be obtained for different wave heights. This does not directly imply that the diffraction model is not able to capture the amplitude of the heave motion in resonance, but that the way of adjusting the model for conditions close to resonance should be carefully done, and studied for different wave heights. The response in pitch shows a good agreement between the models; it also complies with the obtained RAO in pitch.

• *What is the limit of a potential flow based solver regarding wave steepness?*

The last point of this work addresses the response of both models of the OC5-semisubmersible when it is subjected to three waves with a period of 8 s, but with increasing wave height, or steepness, up to 73% of the wave height breaking limit. Both the motions in heave and pitch and the inline and vertical forces are calculated and compared. It is observed that the motions computed with the diffraction model are larger, which is explained by the shape of the nonlinear wave, whose trough does not reach such a large value. From the vertical and horizontal loads analysis, it is seen that the peak forces are in agreement between the models, with a mere maximum discrepancy of less than 14% for the steepest wave case. However, the loading pattern is not in agreement. The interactions of the steepest waves with the elements of the structure should be further analysed. No green water on-deck is observed, although the case treated here does not correspond to the steepest wave that can take place. The most relevant effect observed in the current case is wave run-up, which may affect secondary elements on offshore wind turbine platforms, such as boat landing facilities, J-Tubes, ladders or accessing doors. Therefore for these cases either a diffraction model in combination with a validated semi-empirical model is used, or a fully nonlinear CFD is needed.

6.2. CONCLUSION

The sub-questions were discussed to provide an answer to the following main research question:

How does a (second-order) potential flow theory based diffraction model compare to a fully nonlinear Navier-Stokes numerical wave tank when solving complex fluid-structure interaction problems for offshore floating wind platforms?

To answer this question, the main conclusions that support the final analysis are presented. The conclusions drawn from the first part of the thesis, in which the nonlinear wave tank is further validated for two floating structures (2D floating box and 3D floating vertical cylinder) are given in the following.

• The fully nonlinear Navier-Stokes/VOF numerical wave tank is successfully validated for a floating box in a 2D domain and a floating vertical cylinder in a 3D domain.

• The waveDyMFoam solver with a quasi-static mooring system model implementation is capable of predicting the vertical motions and capturing the nonlinearities of floating bodies subjected to steep regular waves.

• The under-relaxation method is seen to provide decent and stable results for the cases studied here.

The conclusions that can be drawn from the second part of the thesis, which concerns the two numerical models of the OC5-semisubmersible floating wind platform, are enumerated hereafter.

• Both the diffraction and the fully nonlinear CFD model are capable of reproducing wave-structure interaction where linear wave theory applies. However, the computational cost of the diffraction model is much lower.

• Under heave resonance conditions, The response in heave of the diffraction model shows a 40% lower amplitude. The reason behind is related to the the transfer function dependency on the wave height. Moreover, the velocities in these conditions are different to the ones used to adjust the quadratic damping of the diffraction model. The response in pitch for both numerical models is in agreement.

• The peak vertical and horizontal loads predicted by both numerical models are proven to be in agreement, although the loading pattern is not captured by the diffraction model. Furthermore, the main local effect identified here, a wave run-up on the columns as the wave crest impacts on them, cannot be captured by the diffraction model.

The main research question is answered based on the presented conclusions. The numerical tools that are used throughout this research represent two very different approaches to solving the same problem. On the one side, the diffraction model solves the inviscid and irrotational governing equations of the boundary value problem up to the second-order. On the other side, the fully nonlinear CFD solver resolves the fully nonlinear Navier-Stokes equations.

During the current research, two different types of three-dimensional wave-structure interaction problem are studied with the fully nonlinear CFD solver. On the one hand, the second validation case (the 3D vertical floating cylinder) comprises a geometry with low complexity. This permits the a refinement of the mesh at specific locations without exceeding a large computational cost. Consequently, the nonlinear effects are captured and can be analysed in detail at not so high computational costs. On the other hand, the OC5-semisubmersible presents a more complex geometry, which implies a larger amount of cells, and therefore higher computational resources for the same length-scales. Hence a high degree of refinement in the areas of interest is not as feasible, due to computational resources.

Therefore, from a computational efficiency point of view, the answer to the research question is that for structures with low geometrical complexity, for capturing and studying the physical phenomena involved, a nonlinear CFD model is recommended. For structural design purposes, which usually imply more complex geometrical shapes than a cylinder or a box, a fully nonlinear CFD model is needed to calibrate the diffraction model. However, once the latter is adjusted and validated, the results are given at a much lower computational cost. Based on the findings during the current research, for more detailed design and optimisation stages, a CFD model should be applied, so that local effects of nonlinearities on the structure, and their consequences, are captured and analysed. These events include wave run-up, slamming loads on secondary elements or green-water on deck. Moreover, the possible frequency components different from the first (and second) mode on the loading are usually not captured by a diffraction model. These might be of higher relevance for TLP structures, which are more likely to be excited by higher-order components. For these, and other types of offshore structures, a similar analysis should be done, since depending on the structural properties the effects of nonlinearities may differ. A summary of the conclusions discussed is presented in Table 6.1.

Structure's complexity	Case		Nonlinear model (CFD)	Diffraction model
Low	Validation cases (2D box & 3D cylinder)		Detailed refinement allowed	Detailed refinement not allowed
High (OC5-semisubmersible)	Resonance conditions (at T=17s)		Suitable, at very high computational cost	Suitable, at low computational cost, but requires viscous model
	Steepness (at T=8s)	Low	Suitable, includes local effects, convenient for detailed design and optimisation phases	Suitable
		High		Partially suitable, peak forces are captured, convenient for preliminary design

Figure 6.1: Overview of the suitability for numerical models for the cases treated during the current research.

6.3. FURTHER RESEARCH

Although the capability of the fully nonlinear CFD solver to predict motions and to capture the nonlinearities has been proven during the validation process of the same in Chapter 4, several areas that require improvement have been identified. These are listed as recommendations for further research.

- **Capabilities of the dynamic mesh in the Navier-Stokes/VOF solver.** For moored floating wind structures this should not be as relevant, since they are likely to be studied under deep-water conditions, and therefore the radial outer mesh function of the dynamic mesh solver should not be a problem. However, for other offshore applications, such as wave energy converters, where shallower waters apply, the dynamic mesh motion should not be limited by the radial distance, which cannot be larger than the water depth, although it is still on an improvement stage. The new version of OpenFOAM®, v1706, includes a new functionality which would enable to perform overset mesh calculations. Therefore the application of this technique to avoid the difficulties encountered in this research should be investigated for wave-structure interaction problems dealing with long waves.

- **Implementation of turbulent models in the Navier-Stokes/VOF solver.** In all the validation cases analysed, the viscous boundaries are neglected, by applying slip conditions to the solid wall boundaries. For further research, the effect of shear stresses at the wall boundaries should be studied.

- **Procedure to calculate the damping of the system, especially in roll/pitch.** The linear-plus-quadratic damping model used throughout this work is widely applied in industry. However, it should be born in mind that the task of identifying roll damping is not trivial, due to the highly nonlinear damping mechanism, as described in Chakrabarti (2001), which may also involve higher-order components.

- **Validation of the motions and loads of the quasi-static model of the mooring lines.** The model implemented here shows good results in the vertical motions. However, the moorings are substantial for the horizontal ones, and therefore a validation of the model implemented here should be done.

Regarding the second part of this research, further development is recommended in the following areas.

- **Efficiency of the fully nonlinear CFD model for long waves.** One of the alternatives to the use of relaxation zones for absorbing the waves in order to avoid reflections is the Generating and Absorbing Boundary Conditions (GABC), as presented in Düz et al. (2017), although it still presents some limitations.

- **Effects of the wave height in the response amplitude operator under resonance conditions.** In order to be able to fully understand how the wave height affects the behaviour of semisubmersibles, not only for wind energy purposes, more analyses in these conditions, but with different wave heights, should be done.

- **Effects of the heave plates under heave resonance conditions.** An analysis of the nonlinear physical phenomena taking place in resonance conditions at the heave plates should be investigated.

- **Computation of wave loads on the moored structure.** The computed loads with both models should be validated with experimental data.

- **Computation of the local effects of steep waves on the different structural elements.** The nonlinear effects deriving from steeper waves should be studied at the different elements of the floating platform.

- **Computation of impact loads on semisubmersibles in irregular sea states.** Additional sea states to make a better comparison of both models, including phase-focused irregular sea states, using the efficient fully nonlinear potential flow solver developed by Paulsen et al. (2014*a*), should be implemented.

- **Development of semi-empirical models to be coupled with diffraction models.** In order to be able to decrease the computational costs related to phenomena that imply high nonlinearities, the development and coupling of semi-empirical models with diffraction models, such as the ones mentioned here concerning wave run-up, should be investigated and validated.

REFERENCES

Bachynski, E. (2014), Design and Dynamic Analysis of Tension Leg Platform Wind Turbines, PhD thesis, Norwegian University of Science and Technology, NTNU (Trondheim).

Bruinsma, N. (2016), Validation and Application of a Fully Nonlinear Numerical Wave Tank, Master's thesis, Technical University of Delft.

Chakrabarti, S. (2001), 'Empirical Calculation of Roll Damping for Ships and Barges', *International Journal of Marine Energy* **28**, 915–932.

Chan, G., Sclavounos, P., Jonkman, J. & Hayman, G. (2015), 'Computation of Nonlinear Hydrodynamic Loads on Floating Wind Turbines using Fluid-Impulse Theory', *34th International Conference on Ocean, Offshore and Arctic Engineering (OMAE2015)* .

Clauss, G. (1978), 'Multi-scale Model Tests with a Ring-Shaped Semi-submersible', *In proceedings of the Offshore Technology Conference (OTC-3297)* .

DNV (2013), Design of Floating Wind Turbine Structures, Technical report, Det Norske Veritas.

Dunbar, A., Craven, B. A. & Paterson, E. G. (2015), 'Development and Validation of a Tightly Coupled CFD/6-DOF Solver for Simulating Floating Offshore Wind Turbine Platforms', *Ocean Engineering* **110**, 98–105.

Düz, B., Huijsmans, R., Borsboom, M. & Veldman, A. (2017), 'An Absorbing Boundary Condition for Free Surface Water Waves', *Computers & Fluids* .

EU (2010), Energy 2020 — A Strategy for Competitive, Sustainable and Secure Energy; COM(2010), Technical report, European Comission, Brussels.

EU (2014), A Policy Framework for Climate and Energy in the Period from 2020 to 2030; COM(2014), Technical report, European Comission, Brussels.

Faltinsen, O. (1990), *Sea Loads on Ships and Offshore Structures*, Cambridge University Press.

Faltinsen, O. (2005), *Hydrodynamics of High-speed Marine Vehicles*, Cambridge University Press.

Faltinsen, O., Newman, J. & Vinje, T. (1995), 'Nonlinear Wave Loads on a Slender Vertical Cylinder', *Journal of Fluid Mechanics* **78**, 179–198.

Fenton, J. (1988), 'The Numerical Solution of Steady Water Wave Problems', *Computers and Geosciences* **14**(3), 357 – 368.

Ferziger, J. & Perić, M. (2012), *Computational Methods for Fluid Dynamics*, Springer-Verlag, Heidelberg, Berlin.

Ghadimi, P., Bandari, H. & Rostami, A. (2012), 'Determination of the Heave and Pitch Motions of a Floating Cylinder by Analytical Solution of its Diffraction Problem and Examination of the Effects of Geometric Parameters on its Dynamics in Regular waves', *International Journal of Applied Mathematical Research* **1**(4), 611–633.

GWEC (2016), Global Wind Report. Annual Market Update 2016, Technical report, Global Wind Energy Council.

Hirt, C. & Nichols, B. (1981), 'Volume of Fluid (VOF) Method for the Dynamics of Free Boundaries', *Journal of Computational Physics* **39**, 201–225.

Ho, A. & Mbistrova, A. (2017), The European Offshore Wind Industry, Technical report, WindEurope.

Hoff, J. (2001), Estimation of Linear and Quadratic Roll Damping from Free-decay Tests, Technical report, Norwegian University of Science and Technology (NTNU), Trondheim.

Huijs, F., de Bruijn, R. & Savenije, F. (2014), 'Concept Design Verification of a Semi-submersible Floating Wind Turbine Using Coupled Simulations', *Energy Procedia* **53**, 2–12.

Jacobsen, N., Fuhrman, D. & Fredsøe, J. (2012), 'A Wave Generation Toolbox for the Open-source CFD library: OpenFoam®', *International Journal for Numerical Methods in Fluids* **70**(9), 1073–1088.

Jonkman, J. (2009), Definition of a 5-MW Reference Wind Turbine for Offshore System Development, Technical report, National Renewable Energy Laboratory (NREL).

Jonkman, J. (2010), Definition of the Floating System for Phase IV of OC3, Technical report, National Renewable Energy Laboratory (NREL).

Journée, J. & Massie, W. (2001), 'Offshore Hydromechanics', Lecture Notes. TU Delft.

Kim, C. & Chou, F. (1972), 'Motions of a Semisubmersible Drilling Platform in Head Seas', *SNAME News* .

Kirk, C. (1985), 'Resonant Heave Motion of Semisubmersible Vessels', *Ocean Engineering* **12**(2), 177–184.

Koo, B., Kim, M. & Randall, R. (2004), 'Mathieu Instability of a Spar Platform with Moorings and Risers', *Ocean Engineering* **31**, 2175–2208.

Krenk, S. (2001), *Mechanics and Analysis of Beams, Columns and Cables: a Modern Introduction to the Classic Theories*, Springer Science & Business Media.

L. Vos, P. Frigaard, J. R. (2007), 'Wave Run-up on Cylindrical and Cone Shaped Foundations for Offshore Wind Turbines', *Coastal Engineering* **54**(1), 17–29.

Lee, C.-H. (1995), WAMIT. Theory Manual, Technical report, MIT.

Lee, C.-H. & Newman, J. N. (1989), 'First- and Second-order Wave Effects on a Submerged Spheroid', *J. Ship Research* .

Li, L., Gao, Z. & Moan, T. (2013), 'Joint Environmental Data at Five European Offshore Sites for Design of Combined Wind and Wave Energy Devices', *Proceedings of the ASME 28th International Conference on Ocean, Offshore and Arctic Engineering (OMAE2013)* .

MacLachlan, N. (1947), 'Mathieu Functions of Fractional Order', *Studies in Applied Mathematics* **26**, 29–41.

Madsen, P. & Fuhrman, D. (2012), 'High-order Bousinesq-type Modeling of Nonlinear Wave Phenomena in Deep and Shallow Water', *Advances in numerical simulation of nonlinear water waves* **5**, 245–285.

Malenica, S. & Molin, B. (1995), 'Third-harmonic Wave Diffraction by a Vertical Cylinder', *Journal of Fluid Mechanics* **302**, 203–229.

Martin, A., Easson, W. & Bruce, T. (2001), 'Run-up on Columns in Steep, Deep Water Regular Waves', *Journal of Waterway, Port, Coastal, and Ocean Engineering* **127**(1), 26–32.

Maruyama, D., Bailly, D. & Carrier, G. (2012), 'High Quality Mesh Deformation Using Quaternions for Orthogonality Preservation ', *American Institute of Aeronautics and Astronautics* **52**(12), 9–12.

Masciola, M., Chen, X. & Yu, Q. (2008), 'Evaluation of the Dynamic-response-based intact Stability Criterion for Floating Wind Turbines', *American Bureau of Shipping* .

Ming, H., Bing, R. & Da-Hong, Q. (2014), 'Experimental Study of Nonlinear Behaviors of a Free-floating Body in Waves', *China Ocean Engineering* .

Morison, J., Johnson, J. & Schaaf, S. (1950), 'The Force Exerted by Surface Waves on Piles', *Journal of Petroleum technology* **2**(5), 149–154.

Moukalled, F., Darwish, M. & Mangani, L. (2015), *The Finite Volume Method in Computational Fluid Dynamics. An advanced introduction with OpenFOAM©and Matlab©*, Springer-Verlag.

Nayfeh, A. & Mook, D. (1995), *Nonlinear Oscillations*, NY: Wiley Interscience.

Newman, J. (1996), 'Nonlinear Scattering of Long Waves by a Vertical Cylinder', *Waves and Nonlinear Processes in Hydrodynamics; J. Grue, B. Gjevik and J. E. Weber* **1**, 91–97.

Palm, J., Eskilsson, C., Paredes, G. M. & Bergdahl, L. (2016), 'Coupled Mooring Analysis for Floating Wave Energy Converters using CFD: Formulation and Validation', *International Journal of Marine Energy* **16**, 83 – 99.

Paulling, J. (1977), 'Analysis of Semisubmerisble Catamaran-type Platforms', *OTC paper-2975* .

Paulling, J. (2009), 'CFD Simulation of Wave Run-up on a Semi-submersible and Comparison with Experiment', *Proceedings of the ASME 28 International Conference on Ocean, Offshore and Arctic Engineering (OMAE2009)* .

Paulsen, B., Bredmose, H. & Bingham, H. (2014*a*), 'An Efficient Domain Decomposition Strategy for Wave Loads on Surface Piercing Circular Cylinders', *Coastal Engineering* **86**, 57–76.

Paulsen, B. T., Bredmose, H. & Bingham, H. (2014*b*), 'Forcing of a Bottom-mounted Circular Cylinder by Steep Water Waves at Finite Depth', *Journal of Fluid Mechanics* **755**, 1–34.

Penalba, M., Giorgi, G. & Ringwood, J. V. (2017), 'Mathematical Modelling of Wave Energy Converters: A Review of Nonlinear Approaches', *Renewable and Sustainable Energy Reviews* **78**, 1188–1207.

Pinkster, J. & Huijsmans, H. (1982), 'The Low-frequency Motion of a Semisubmersible in Waves', *Netherlands Ship Model Basin, The Netherlands* .

Rainey, R. (2007), 'Weak or Strong Nonlinearity: the Vital Issue', *Journal of Engineering Mathematics* **58**(1-4), 229–249.

Rienecker, M. M. & Fenton, J. D. (1981), 'A Fourier Approximation Method for Steady Water Waves', *Journal of Fluid Mechanics* **104**, 119 – 137.

Robertson, A., Jonkman, J., Masciola, M., Song, H., Goupee, A., Coulling, A. & Luan, C. (2014), Definition of the Semisubmersible Floating System for Phase II of OC4, Technical report, National Renewable Energy Laboratory (NREL).

Roddier, D., Peiffer, A., Aubault, A. & Weinstein, J. (2011), 'A Generic 5 MW Windfloat for Numerical Tool Validation & Comparison Against a Generic Spar', *Proceedings of the ASME 2011 30th International Conference on Ocean, Offshore and Arctic Engineering* .

Rusche, H. (2002), A Numerical Method for Two-Dimensional Studies of Large Amplitude Motions of Floating Bodies in Steep Waves, PhD thesis, Imperial College of Science, Technology & Medicine.

Samareh, J. (2002), Application of Quaternions for Mesh Deformation, Technical report, NASA.

Sarpkaya, T. & Isaacson, M. (1981), *Mechanics of Wave Forces on Offshore Structures*, van Nostrand Reinhold, New York.

SIMO (2012), SIMO Theory Manual, Technical report, DNV.

Sumer, B. M. & Fredsøe, J. (2006), *Hydrodynamics Around Cylindrical Structures*, World Scientific Publishing Co. Pte. Ltd.

Tao, L. & Cai, S. (2004), 'Heave Motion Suppression of a Spar with a Heave Plate', *Ocean Engineering* **31**, 669–692.

Tedesco, J. W., McDougal, W. G. & Ross, C. A. (1999), *Structural Dynamics. Theory and Applications.*, Addison Wesley Longman, Inc.

Viré, A., Spinneken, J., Piggott, M., Painc, C. & Kramer, S. (2016), 'Application of the Immersed-body Method to Simulate Wave–structure Interactions', *European Journal of Mechanics - B/Fluids* **55**, 330–339.

Wadam (2010), Wadam. Wave Analysis by Diffraction and Morison Theory. User Manual., Technical report, Det Norske Veritas.

WindEurope (2017), Floating Offshore Wind Vision Statement - June 2017, Technical report, WindEurope.

A

VALIDATION CASES

A.1. 3D CASE. FLOATING VERTICAL CYLINDER

The mesh of the numerical domain of the 3D vertical floating cylinder when subjected to steep regular waves, presented in Chapter 4, Section 4.3.3 is depicted in Figure A.1. The finest mesh is identified upstream the body and around the free surface; downstream the grid coarsens linearly.
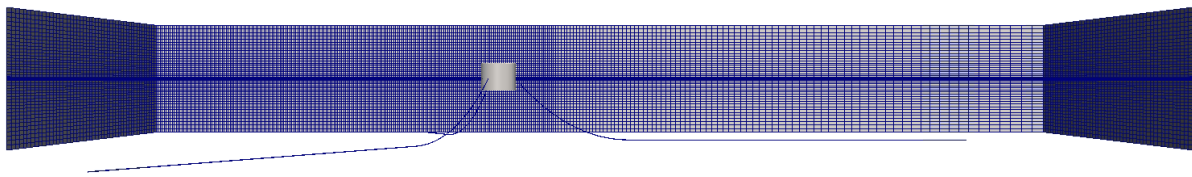

Figure A.1: Overview of the numerical set-up of the vertical floating cylinder.

A.1.1. SURGE RESPONSE TO INCOMING WAVES FREQUENCY ANALYSIS

Figure A.2 presents the frequency-domain decomposition of the time-domain response of the floating vertical cylinder subjected to regular waves ($T = 1.2$ s and $H = 0.04$ m), as presented in Chapter 4, Section 4.3.3. Three frequencies are identified: the one corresponding to the main wave excitation frequency (around 1.2 s), the second one to the second harmonic of the wave (around 2.4 s) and the lowest one to the natural frequency in surge (around 9 s).
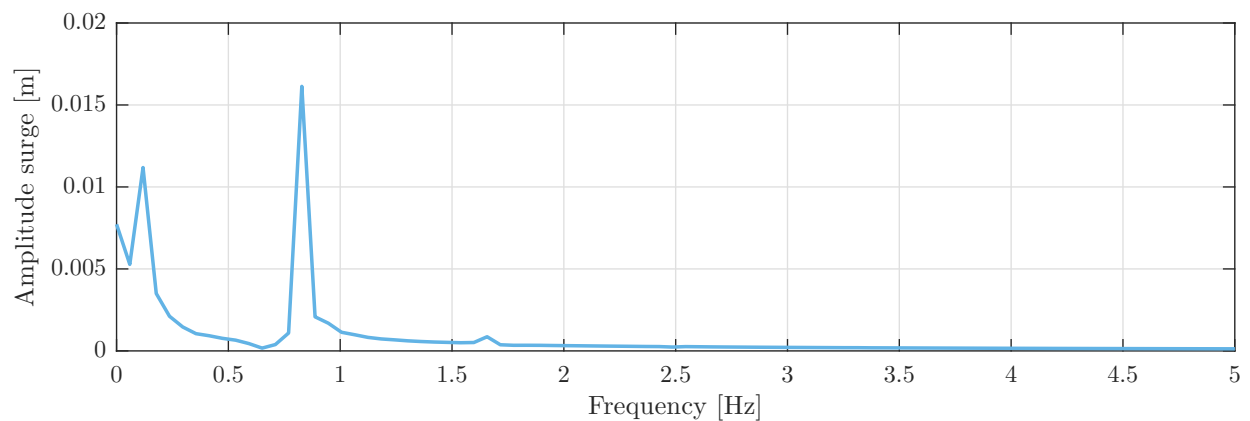
Figure A.2: Response of the floating cylinder to the waves in surge in the frequency-domain.

A.1.2. Mooring lines forces

The mooring system consists of three mooring lines, implemented quasi-statically on the floating cylinder. The one in the back is placed at a zero degree angle, with respect to the incident waves angle. The two mooring lines in the front are implemented 120° separated from each other, as it can be seen in Figures A.1 and A.3. The mass per length of the chain is 0.1447 kg/m, the submerged weight 1.24 N/m and the diameter 0.0048 m, as stated in Palm et al. (2016).
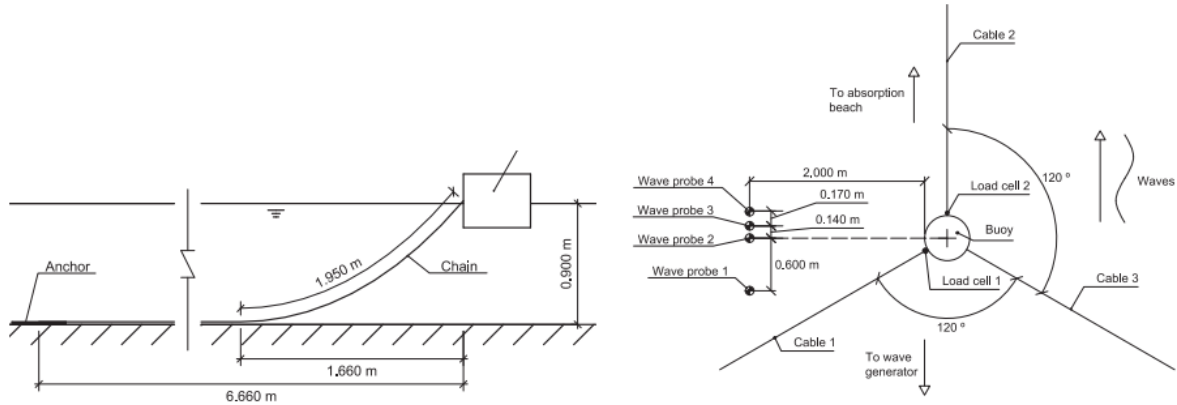
Figure A.3: Geometric description of the experimental setup and the mooring cable configuration (Palm et al. (2016)). Here cable 1 and cable 3 correspond to the front 1 and front2 mooring lines, respectively.

The forces are calculated at the fairlead position. The initial vertical component is equal to the submerged weight of the mooring line. All the reactions are consistent with each other. However, the total force does not match the one measured experimentally. The results presented here correspond to the simulation completed with the *predictor-corrector* method.
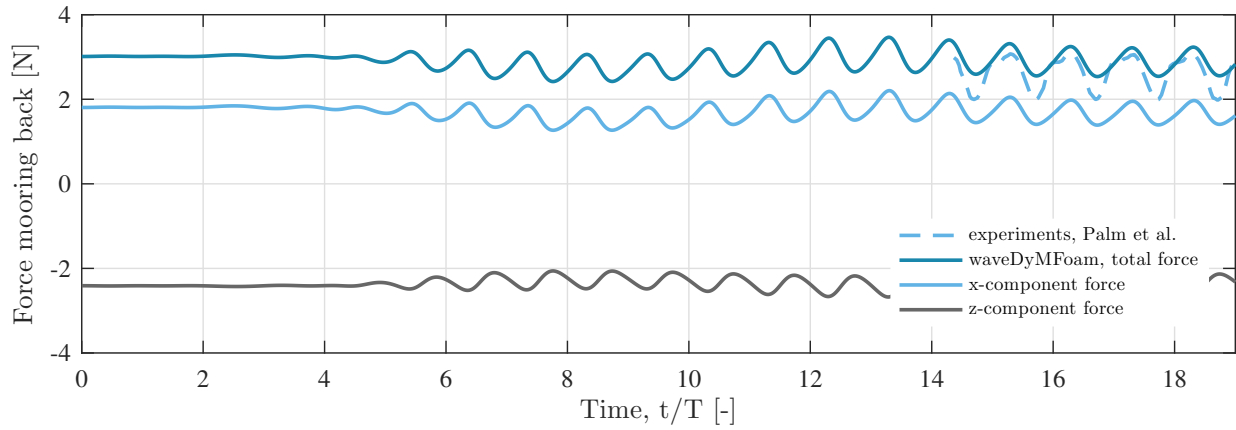
(a) Total force and components at the fairlead of the back mooring line.
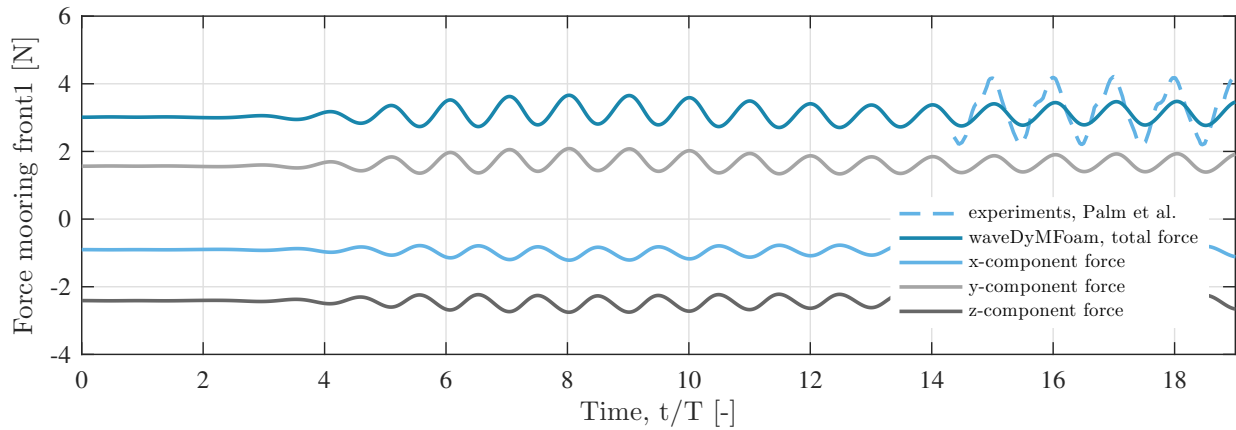
(b) Total force and components at the fairlead of the front mooring line.
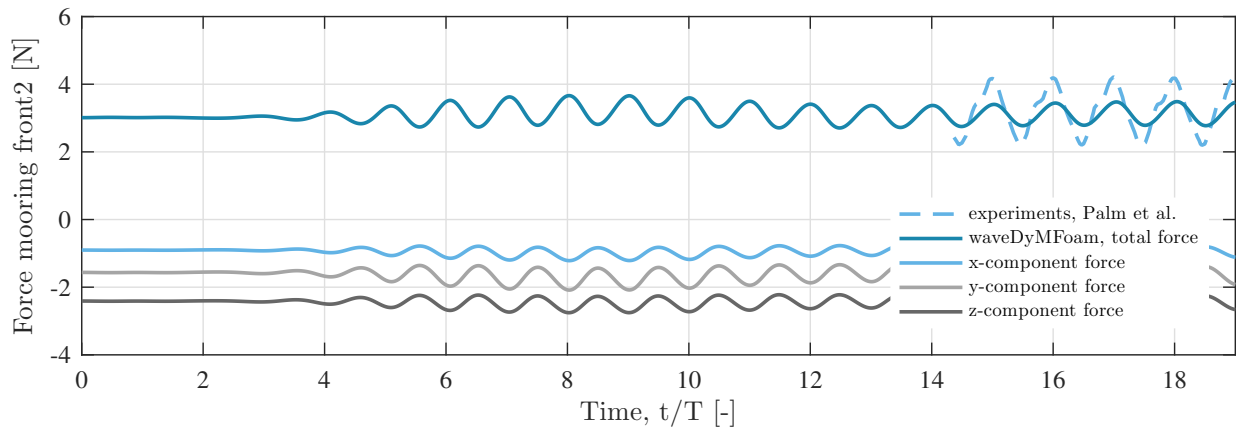
(c) Total and components at the fairlead of the front mooring line.

Figure A.4: Mooring lines total forces and the components.

B

OC5-SEMISUBMERSIBLE CASE STUDY

B.1. DIMENSIONS OF THE OC5-SEMISUBMERSIBLE FLOATING SUBSTRUCTURE

Table B.1: Dimensions of the of the full-scale OC5-semisubmersible sub-structure of the floating wind system, as indicated in Figures B.1, B.2 and B.3.

Indicator	a	b	c	d	e	f	g	h	i	j	k
Length [m]	14.0	24.0	6.0	26.0	43.3	28.9	14.4	24.0	3.0	26.4	50.0
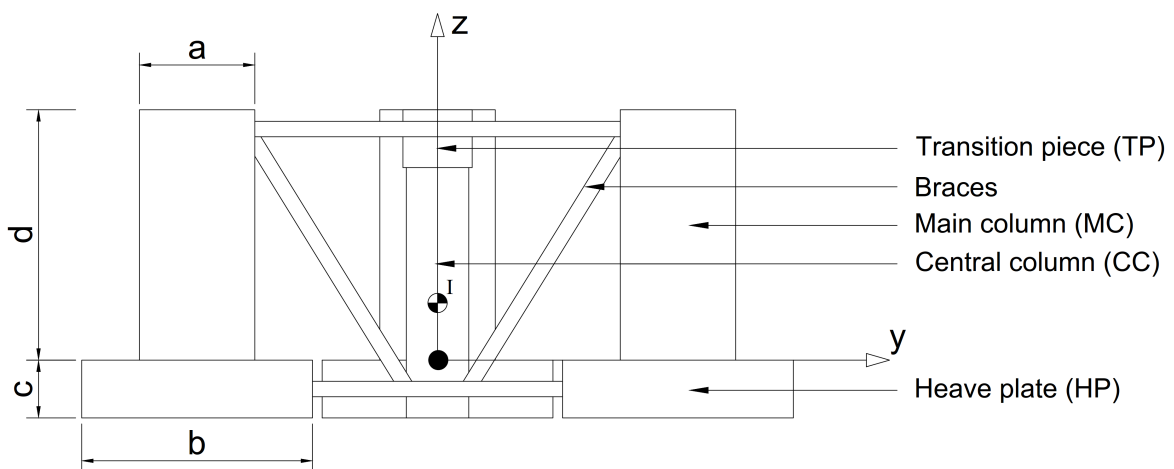
Figure B.1: Left-view of the sub-structure of the floating wind structure, the OC5-semisubmersible. All the dimensions, referred with letters, are defined in Table B.1. The *COG* is denoted as I.
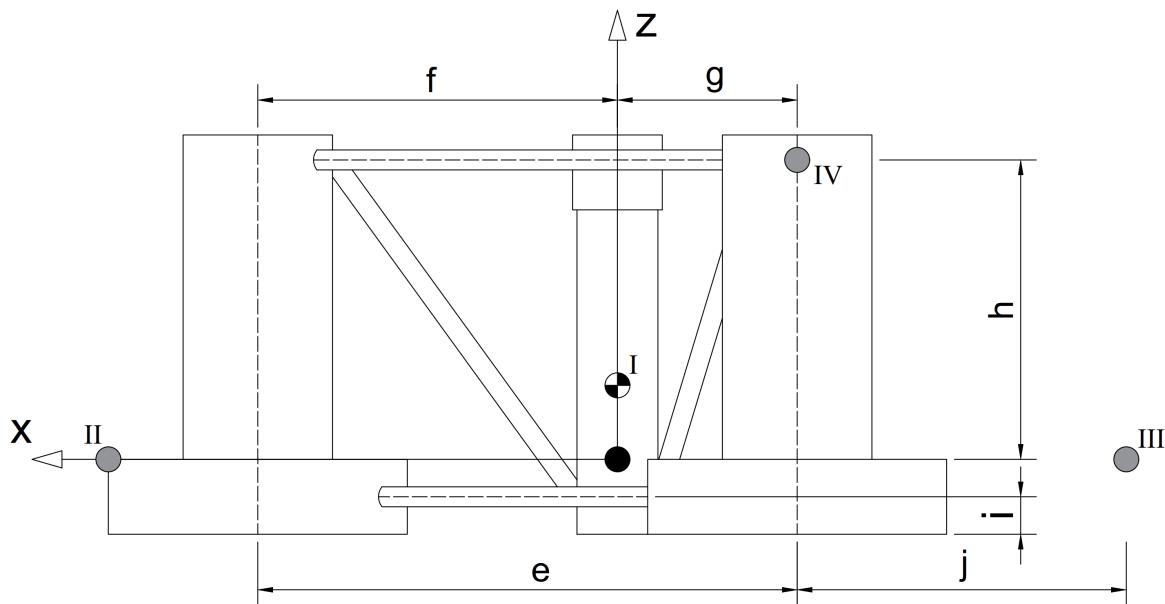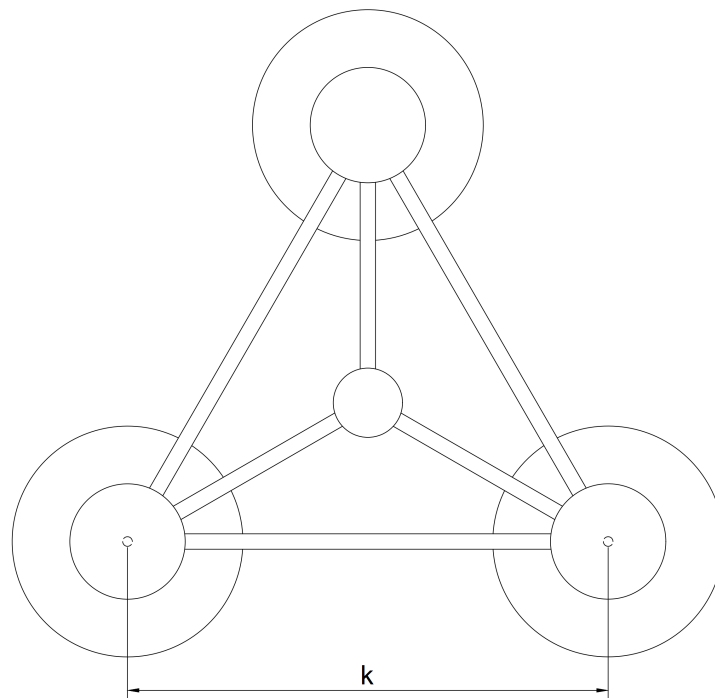
Figure B.2: Back-view of the sub-structure of the floating wind structure, the OC5-semisubmersible. All the dimensions, referred with letters, are defined in Table B.1. The *COG* is denoted as I.

Figure B.3: Top-view of the sub-structure of the floating wind structure.

B.2. FLOATING PLATFORM STRUCTURAL PROPERTIES

Table B.2: Dimensions of the main components of the full-scale OC5-semisubmersible floating structure.

Element [m]	Number	Diameter [m]	Length [m]
Transition piece (TP)	1	7	6
Central column (CC)	1	6.5	26
Main columns (MC)	3	12	26
Heave plates (HP)	3	24	6
Braces	9	1.6	-

Table B.3: Properties of the full-scale OC5-semisubmersible floating platform as implemented in the numerical models. Note that d^1 and d^2 denote the draft with and without moorings, respectively.

d^1	d^2	KG	Total mass	Buoyancy	I_{xx}	I_{yy}	I_{zz}
20.54 m	20.00 m	11.93 m	$1.42 \cdot 10^7$ kg	13900 m^3	$1.55 \cdot 10^{10}$ kg·m^2	$1.49 \cdot 10^{10}$ kg·m^2	$1.37 \cdot 10^{10}$ kg·m^2

B.3. RESTRAINTS (MOORING LINES AND HORIZONTAL SPRINGS)

Table B.4: Properties of the full-scale restraining system of the floating wind structure and points of attachment on the body (fairlead) and at the seabed (anchor). In brackets the label for each element as indicated in Figures in Figures B.1, B.2 and B.3 is given.

	Unstretched length [m]	Submerged weight [N/m]	Fairlead	Anchor
COG (I)	-	-	0.0, 0.0, 5.93	-
Front mooring (II)	919.09	1066.35	(40.9, 0.0, 0.0)	(921.7, 0.0, 0.0)
Back mooring (III)	835.50	1066.35	(-40.9, 0.0, 0.0)	(838.1, 0.0, 0.0)
Springs (IV, V)	-	$k = 37250$	(-20.4, -/+35.4, 30.0)	(-20.4, -/+100.0, 30.0)

B.3.1. MOORING LINES STIFFNESS

To account for the mooring system stiffness in the diffraction model, the stiffness components of the lines are calculated according to the following expressions:

$$
\begin{aligned}
k_{11} &= S_h \cos^2 \alpha_x \\
k_{21} &= S_h \cos \alpha_x \sin \alpha_x \\
k_{51} &= k_{11} z &= k_{15} \\
k_{22} &= S_h \sin^2 \alpha_x \\
k_{41} &= -k_{21} z &= k_{14} \\
k_{42} &= -k_{22} z &= k_{24} \\
k_{62} &= k_{22} x - k_{21} y &= k_{26} \\
k_{44} &= -k_{42} z + P_y y + P_z z \\
k_{46} &= k_{24} x - k_{41} y - P_x z \\
k_{64} &= k_{24} x - k_{41} y - P_z x \\
k_{55} &= k_{51} z - k_{53} x + P_x x + P_z z \\
k_{66} &= k_{62} x - k_{61} y + P_y y + P_x x
\end{aligned}
\tag{B.1}
$$

S_h is the horizontal constant and α_x is the angle at which the fairlead is placed with respect to the positive x-direction. P_x and P_y are the x- and y- components of the pre-tension. In order to illustrate stiffness derivation

procedure for every component, the one in surge (K_{11}) is derived in the following.

$$S_h = \mu_{sub} g \left[\frac{-2}{\sqrt{1 + 2\dfrac{\tau^*}{h}}} + \cosh^{-1}\left(1 + \frac{h}{\tau^*}\right) \right],$$ (B.2)

where μ is the submerged mass and $\tau^* = \frac{\tau_{hor}}{\mu g}$, where τ_{hor} is the horizontal pretension, already known. h is the vertical coordinate of the touchdown point, and is given by:

$$h = \frac{\mu_{sub} g l_{eff}^2}{2EA} + \tau^* \left(\sqrt{1 + \left(\frac{l_{eff}}{\tau^*}\right)^2} - 1 \right)$$ (B.3)

The effective length l_{eff}, indicated in Figure B.4, is calculated iteratively by:

$$l_{rest} = l_{tot} - l_{eff} = l_{hor,tot} - l_{hor} = l_{hor,tot} - \tau^* \sinh^{-1}\left(\frac{l_{eff}}{\tau^*}\right) - \frac{\tau_{hor} l_{eff}}{EA},$$ (B.4)

where l_{tot} is the total length of the catenary, from p_l to p_0. The total restoring stiffness in surge is given by the sum of the two mooring lines contributions, 1 and 2, respectively, as:

$$K_{11} = k_{11,1} + k_{11,2} = S_{h,1} \cos^2 \alpha_{x,1} + S_{h,2} \cos^2 \alpha_{x,2},$$ (B.5)

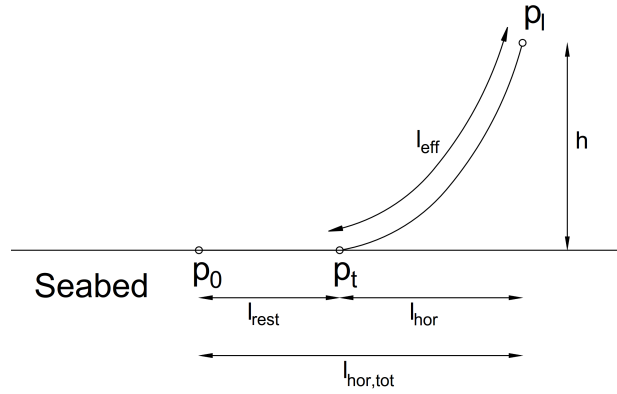where $\alpha_{x,1}$ and $\alpha_{x,2}$ are $0°$ and $180°$, respectively.

Figure B.4: Catenary mooring line, with p_0 the anchor point, p_t the touchdown point and p_l the fairlead.

B.4. HYDRODYNAMIC PROPERTIES

Table B.5: Hydrostatic stiffness of the full-scale OC5-semisubmersible floating platform diffraction model.

C_{33} [N/m]	C_{44} [N·m]	C_{55} [N·m]
$3.8 \cdot 10^6$	$7.5 \cdot 10^8$	$7.5 \cdot 10^8$

Table B.6: Viscous (quadratic) damping implemented in the hydrodynamic computations in Wadam. Obtained form the computations based on the experiments carried out in MARIN.

B_{11}^* [Ns^2/m^2]	B_{22}^* [Ns^2/m^2]	B_{33}^* [Ns^2/m^2]	B_{44}^* [Ns^{2}m]	B_{55}^* [Ns^{2}m]
$1.02 \cdot 10^6$	$1.02 \cdot 10^6$	$1.90 \cdot 10^6$	$2.91 \cdot 10^9$	$2.91 \cdot 10^9$

B.5. QUADRATIC TRANSFER FUNCTION (QTF)
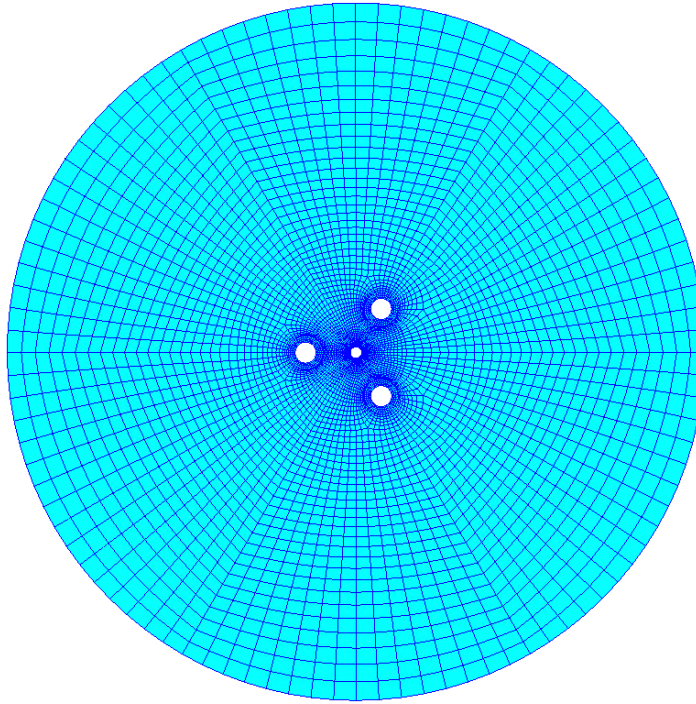
Figure B.5: Free surface mesh.
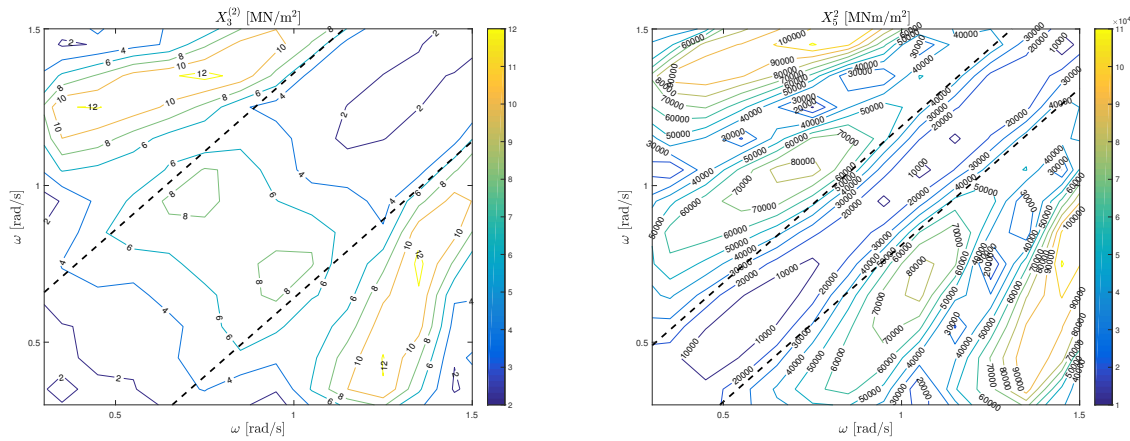
(a) QTF heave.

(b) QTF pitch.

Figure B.6: Difference-frequency quadratic transfer function in heave and in pitch.

B.6. VALIDATION OF THE DIFFRACTION MODEL

The frequency-domain decomposition of the experimental decay test (presented in Section 5.3, Figure 5.8a) from MARIN and the diffraction model is presented in order to identify the lower frequency components.
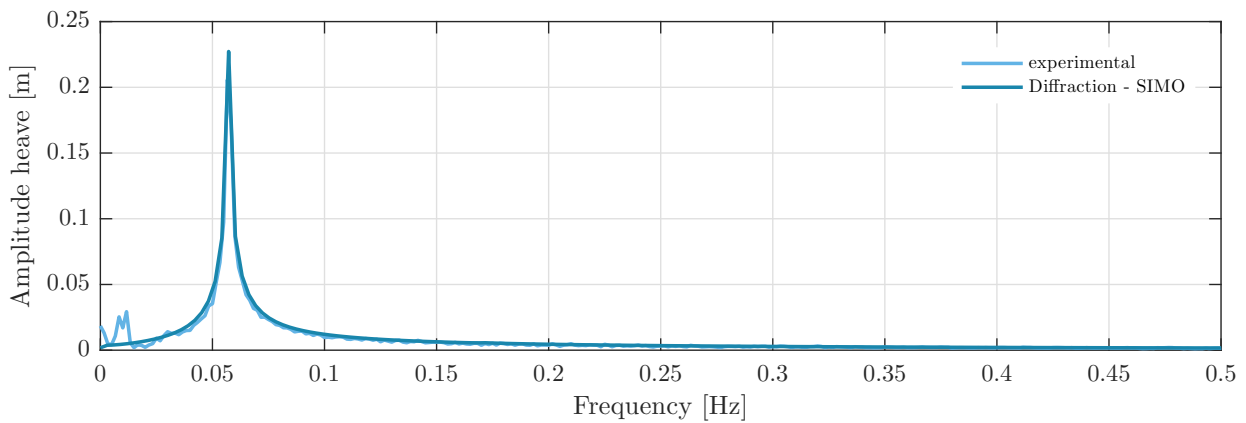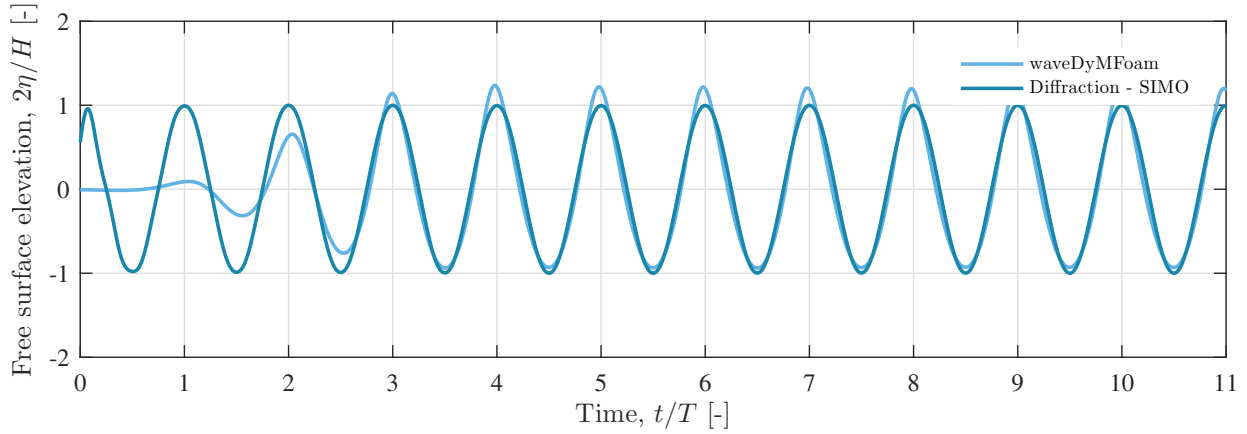

Figure B.7: Frequency-domain decomposition of the heave decay test.
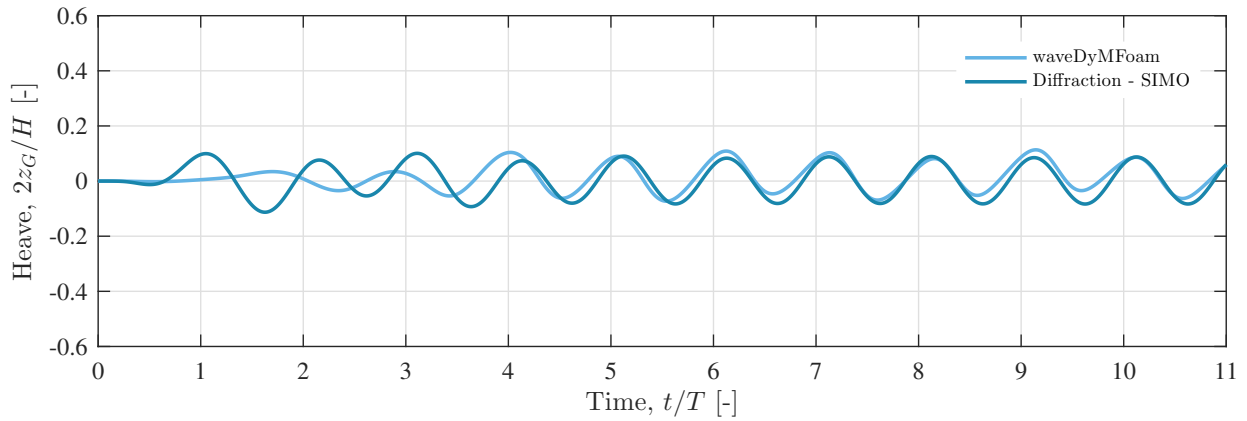
B.7. Response to Regular Waves Increasing in Steepness

Here the free surface elevation, together with the motions with waves increasing in steepness is presented.
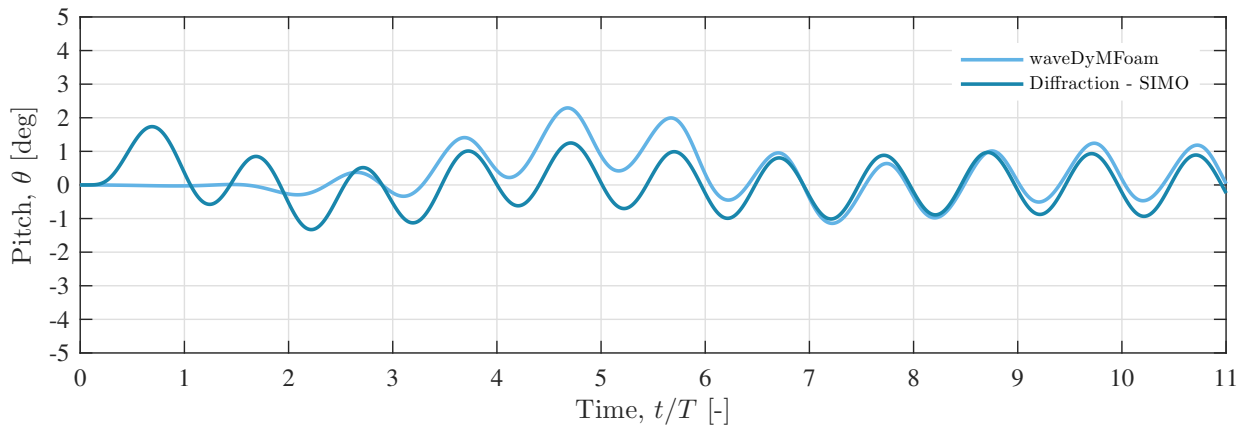
B.7.1. H/Hmax = 0.55

(a) Undisturbed free surface elevation 0.25 m upstream of the structure, normalised by the incoming wave height.
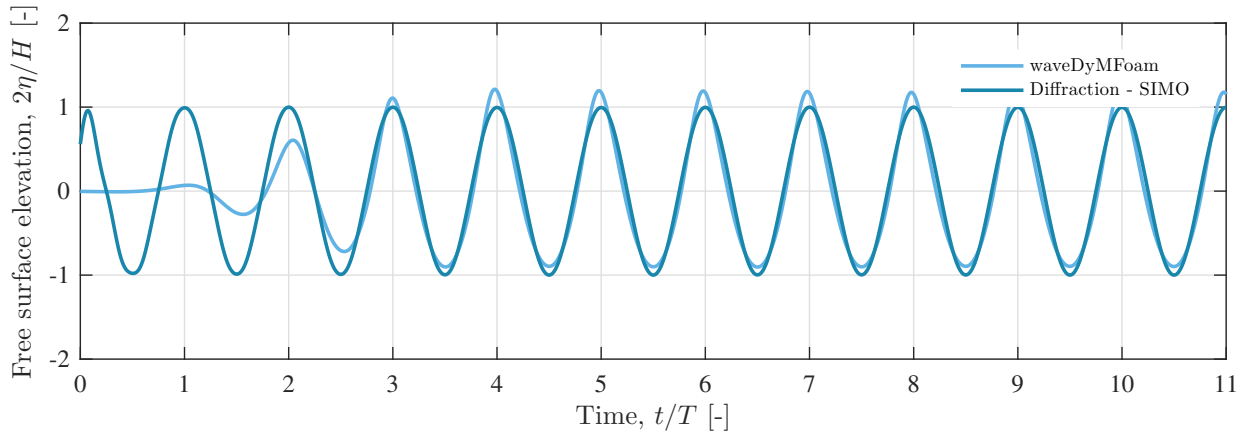

(b) Heave response.

(c) Pitch response.

Figure B.8: Free surface elevation (a), heave (b) and pitch (c) response of the moored floating platform.

B.7.2. $H/H_{MAX} = 0.60$

(a) Undisturbed free surface elevation 0.25 m upstream of the structure, normalised by the incoming wave height.
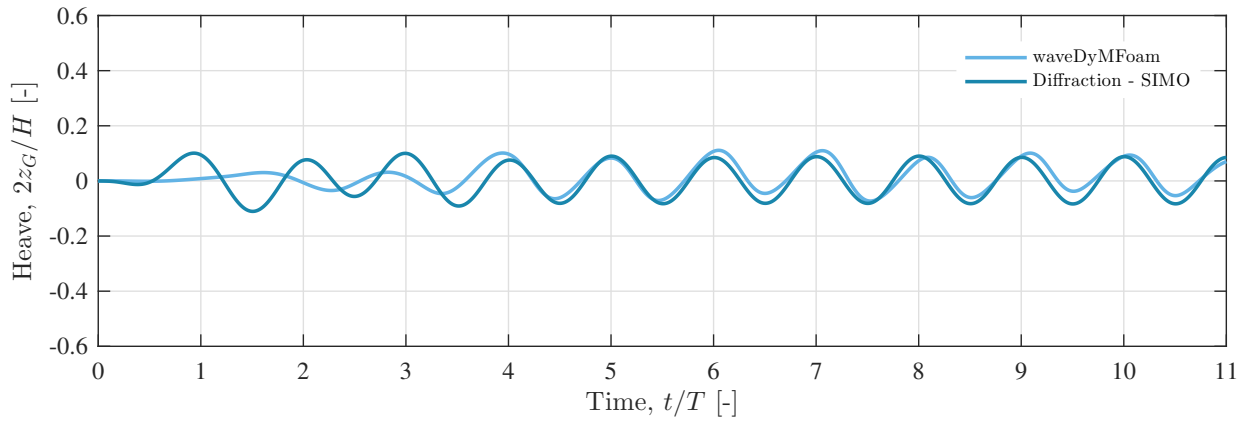

(b) Heave response.

(c) Pitch response.

Figure B.9: Free surface elevation (a), heave (b) and pitch (c) response of the moored floating platform.

B.7.3. H/Hmax = 0.73

(a) Undisturbed free surface elevation 0.25 m upstream of the structure, normalised by the incoming wave height.

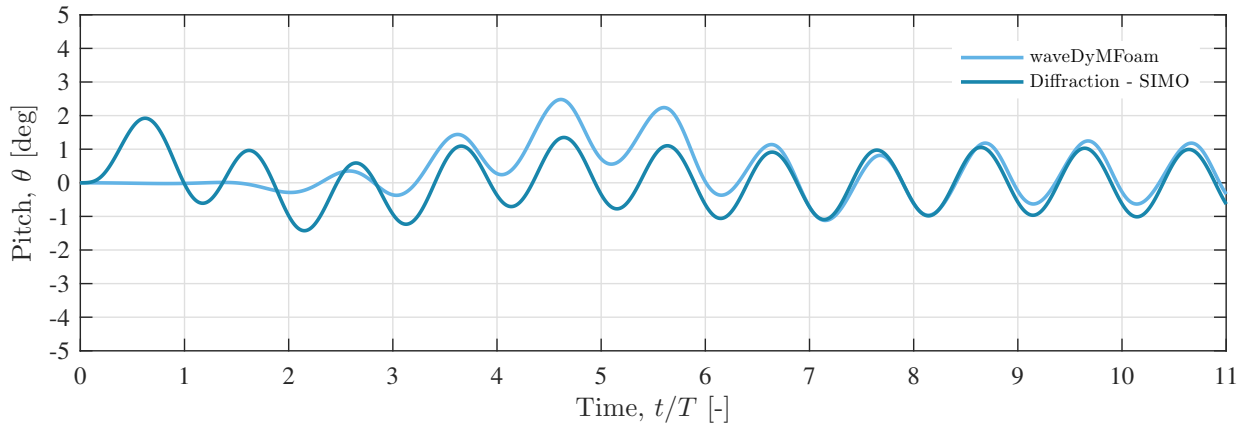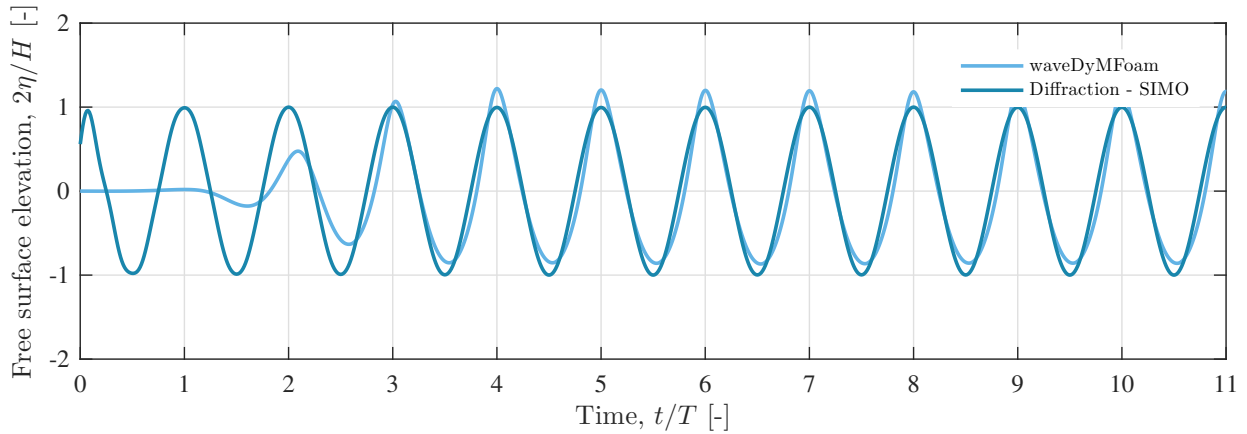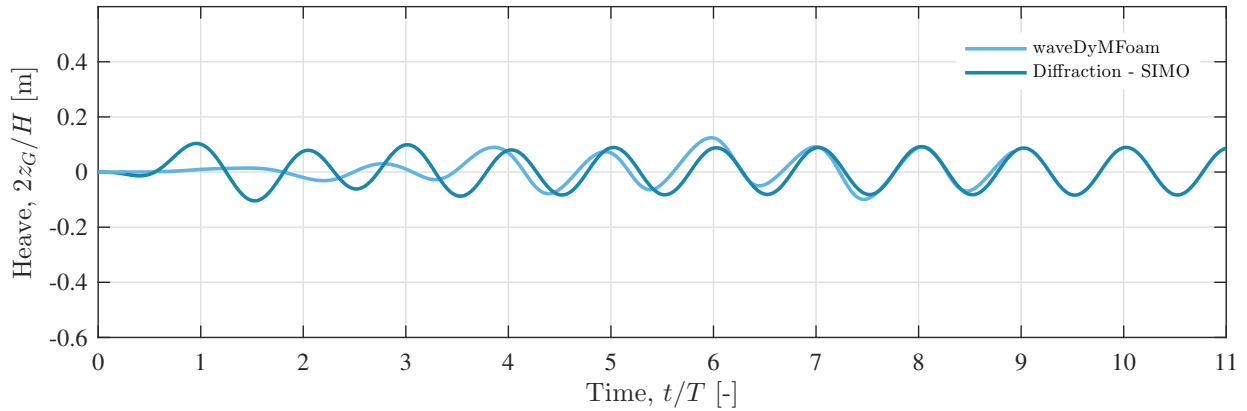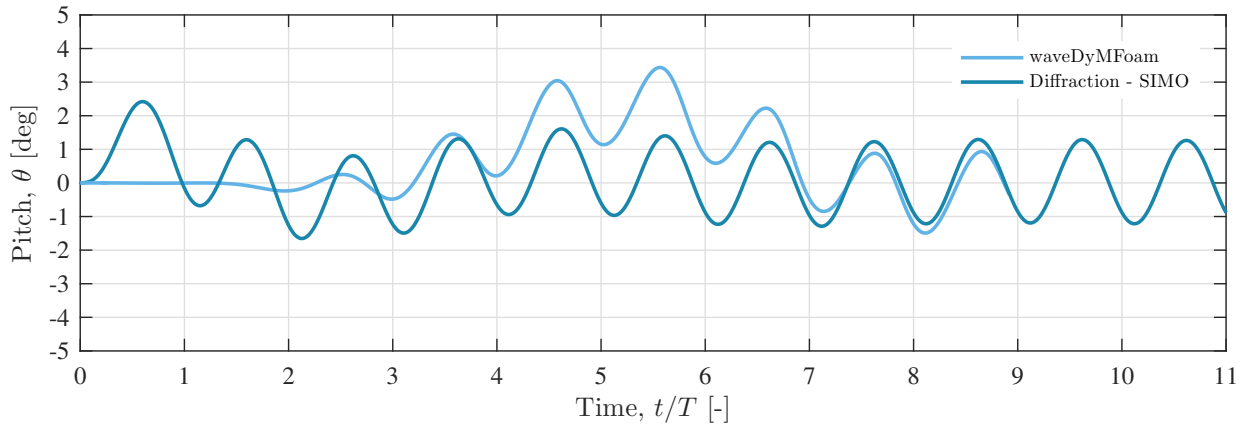

(b) Heave response.

(c) Pitch response.

Figure B.10: Free surface elevation (a), heave (b) and pitch (c) response of the moored floating platform.

B.7.4. VELOCITY COMPONENTS OF THE STEEPEST WAVES (H/HMAX = 0.60 AND H/HMAX = 0.73)
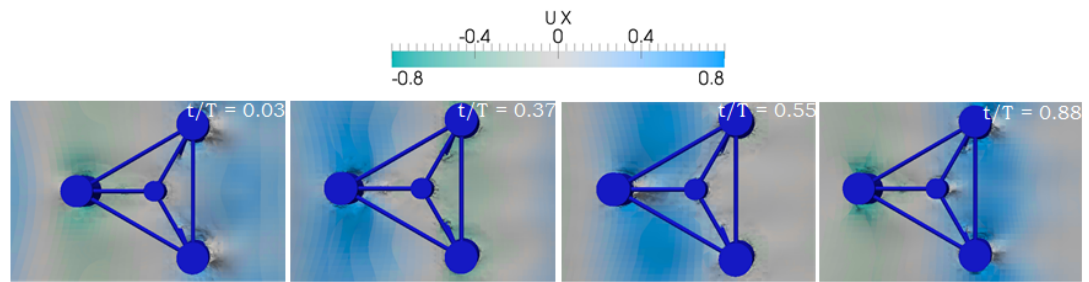
(a) x-component of the wave celerity.
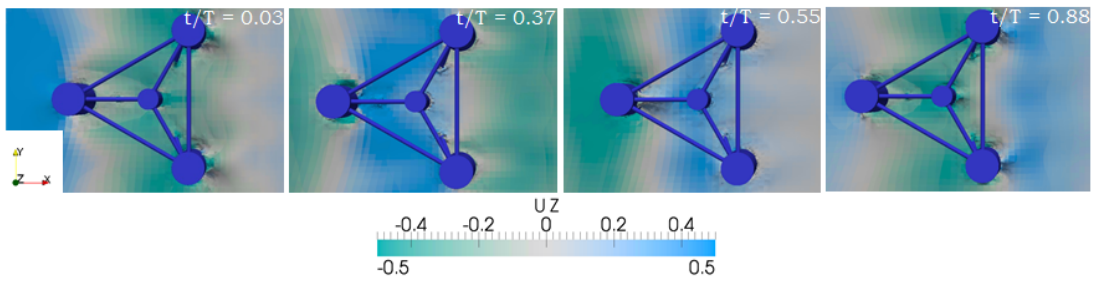
(b) z-component of the wave celerity.

Figure B.11: Snapshots of the velocity components for $H/H_{max} = 0.60$.
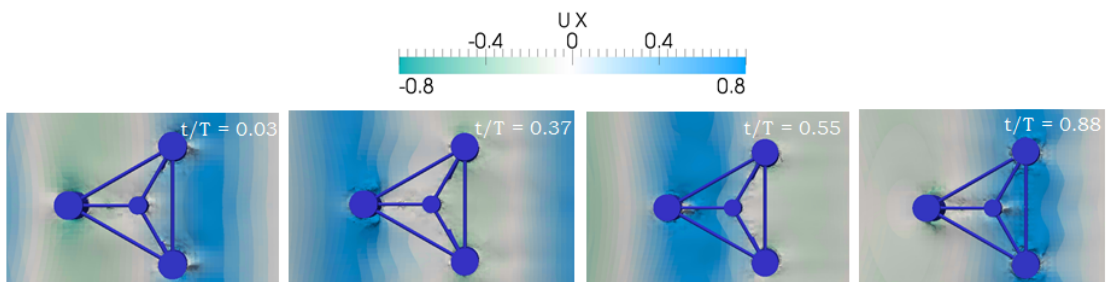
(a) x-component of the wave celerity.
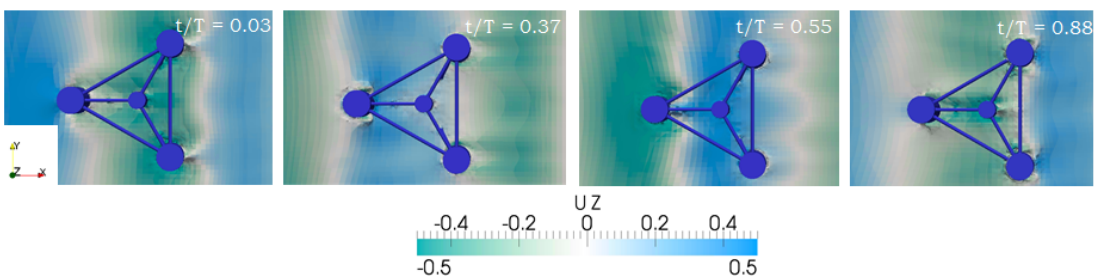
(b) z-component of the wave celerity.

Figure B.12: Snapshots of the velocity components for $H/H_{max} = 0.73$.

C

OPENFOAM® CODES

C.1. WAVEFOAM

```
/*--------------------------------------------------------------------------*\
  =========                 |
  \\      /  F ield         | OpenFOAM: The Open Source CFD Toolbox
   \\    /   O peration     |
    \\  /    A nd           | Copyright (C) 2011-2016 OpenFOAM Foundation
     \\/     M anipulation  |
--------------------------------------------------------------------------
License
    This file is part of OpenFOAM.

    OpenFOAM is free software: you can redistribute it and/or modify it
    under the terms of the GNU General Public License as published by
    the Free Software Foundation, either version 3 of the License, or
    (at your option) any later version.

    OpenFOAM is distributed in the hope that it will be useful, but WITHOUT
    ANY WARRANTY; without even the implied warranty of MERCHANTABILITY or
    FITNESS FOR A PARTICULAR PURPOSE.  See the GNU General Public License
    for more details.

    You should have received a copy of the GNU General Public License
    along with OpenFOAM.  If not, see <http://www.gnu.org/licenses/>.

Application
    interFoam

Description
    Solver for 2 incompressible, isothermal immiscible fluids using a VOF
    (volume of fluid) phase-fraction based interface capturing approach.

    The momentum and other fluid properties are of the "mixture" and a single
    momentum equation is solved.

    Turbulence modelling is generic, i.e. laminar, RAS or LES may be selected.

    For a two-fluid approach see twoPhaseEulerFoam.
```

```cpp
/*---------------------------------------------------------------------------*/

#include "fvCFD.H"
#include "CMULES.H"
#include "EulerDdtScheme.H"
#include "localEulerDdtScheme.H"
#include "CrankNicolsonDdtScheme.H"
#include "subCycle.H"
#include "immiscibleIncompressibleTwoPhaseMixture.H"
#include "turbulentTransportModel.H"
#include "pimpleControl.H"
#include "fvOptions.H"
#include "CorrectPhi.H"
#include "localEulerDdtScheme.H"
#include "fvcSmooth.H"

#include "relaxationZone.H"
#include "externalWaveForcing.H"

// * * * * * * * * * * * * * * * * * * * * * * * * * * * * * * * * * * * //

int main(int argc, char *argv[])
{
    #include "postProcess.H"

    #include "setRootCase.H"
    #include "createTime.H"
    #include "createMesh.H"
    #include "createControl.H"
    #include "createTimeControls.H"
    #include "createRDeltaT.H"
    #include "initContinuityErrs.H"

    #include "createFields.H"
    #include "createFvOptions.H"
    #include "correctPhi.H"

    turbulence->validate();

    if (!LTS)
    {
        #include "readTimeControls.H"
        #include "CourantNo.H"
        #include "setInitialDeltaT.H"
    }

    // * * * * * * * * * * * * * * * * * * * * * * * * * * * * * * * * * * * //

    Info<< "\nStarting time loop\n" << endl;

    while (runTime.run())
    {
        #include "readTimeControls.H"
```

```
        if (LTS)
        {
            #include "setRDeltaT.H"
        }
        else
        {
            #include "CourantNo.H"
            #include "alphaCourantNo.H"
            #include "setDeltaT.H"
        }

        runTime++;

        Info<< "Time = " << runTime.timeName() << nl << endl;

        externalWave->step();

        // --- Pressure-velocity PIMPLE corrector loop
        while (pimple.loop())
        {
            #include "alphaControls.H"
            #include "alphaEqnSubCycle.H"

            relaxing.correct();

            mixture.correct();

            #include "UEqn.H"

            // --- Pressure corrector loop
            while (pimple.correct())
            {
                #include "pEqn.H"
            }

            if (pimple.turbCorr())
            {
                turbulence->correct();
            }
        }

        runTime.write();

        Info<< "ExecutionTime = " << runTime.elapsedCpuTime() << " s"
            << "  ClockTime = " << runTime.elapsedClockTime() << " s"
            << nl << endl;
    }

    // Close down the external wave forcing in a nice manner
    externalWave->close();

    Info<< "End\n" << endl;

    return 0;
}
```

// *** //

C.2. WAVEDYMFOAM

```
/*---------------------------------------------------------------------------*\
  =========                 |
  \\      /  F ield         | OpenFOAM: The Open Source CFD Toolbox
   \\    /   O peration     |
    \\  /    A nd           | Copyright (C) 2011-2016 OpenFOAM Foundation
     \\/     M anipulation  |
-------------------------------------------------------------------------------
License
    This file is part of OpenFOAM.

    OpenFOAM is free software: you can redistribute it and/or modify it
    under the terms of the GNU General Public License as published by
    the Free Software Foundation, either version 3 of the License, or
    (at your option) any later version.

    OpenFOAM is distributed in the hope that it will be useful, but WITHOUT
    ANY WARRANTY; without even the implied warranty of MERCHANTABILITY or
    FITNESS FOR A PARTICULAR PURPOSE.  See the GNU General Public License
    for more details.

    You should have received a copy of the GNU General Public License
    along with OpenFOAM.  If not, see <http://www.gnu.org/licenses/>.

Application
    interDyMFoam

Group
    grpMultiphaseSolvers grpMovingMeshSolvers

Description
    Solver for 2 incompressible, isothermal immiscible fluids using a VOF
    (volume of fluid) phase-fraction based interface capturing approach,
    with optional mesh motion and mesh topology changes including adaptive
    re-meshing.

\*---------------------------------------------------------------------------*/

#include "fvCFD.H"
#include "dynamicFvMesh.H"
#include "CMULES.H"
#include "EulerDdtScheme.H"
#include "localEulerDdtScheme.H"
#include "CrankNicolsonDdtScheme.H"
#include "subCycle.H"
#include "immiscibleIncompressibleTwoPhaseMixture.H"
#include "turbulentTransportModel.H"
#include "pimpleControl.H"
#include "fvOptions.H"
#include "CorrectPhi.H"
```

```
#include "localEulerDdtScheme.H"
#include "fvcSmooth.H"
#include "fvcSmooth.H"

#include "relaxationZone.H"
#include "externalWaveForcing.H"
// * * * * * * * * * * * * * * * * * * * * * * * * * * * * * * * * * * * * * //

int main(int argc, char *argv[])
{
    #include "setRootCase.H"
    #include "createTime.H"
    #include "createDynamicFvMesh.H"
    #include "initContinuityErrs.H"

    #include "readGravitationalAcceleration.H"
    #include "readWaveProperties.H"
    #include "createExternalWaveForcing.H"

    pimpleControl pimple(mesh);

    #include "createControls.H"
    #include "createRDeltaT.H"
    #include "createFields.H"
    #include "createMRF.H"
    #include "createFvOptions.H"

    volScalarField rAU
    (
        IOobject
        (
            "rAU",
            runTime.timeName(),
            mesh,
            IOobject::READ_IF_PRESENT,
            IOobject::AUTO_WRITE
        ),
        mesh,
        dimensionedScalar("rAUf", dimTime/rho.dimensions(), 1.0)
    );

    #include "correctPhi.H"
    #include "createUf.H"

    turbulence->validate();

    if (!LTS)
    {
        #include "CourantNo.H"
        #include "setInitialDeltaT.H"
    }

    // * * * * * * * * * * * * * * * * * * * * * * * * * * * * * * * * * * * * * //
    Info<< "\nStarting time loop\n" << endl;
```

```
while (runTime.run())
{
    #include "readControls.H"

    if (LTS)
    {
        #include "setRDeltaT.H"
    }
    else
    {
        #include "CourantNo.H"
        #include "alphaCourantNo.H"
        #include "setDeltaT.H"
    }

    runTime++;

    Info<< "Time = " << runTime.timeName() << nl << endl;

    // --- Pressure-velocity PIMPLE corrector loop
    while (pimple.loop())
    {
        if (pimple.firstIter() || moveMeshOuterCorrectors)
        {
            scalar timeBeforeMeshUpdate = runTime.elapsedCpuTime();

            mesh.update();

            if (mesh.changing())
            {
                Info<< "Execution time for mesh.update() = "
                    << runTime.elapsedCpuTime() - timeBeforeMeshUpdate
                    << " s" << endl;

                gh = (g & mesh.C()) - ghRef;
                ghf = (g & mesh.Cf()) - ghRef;
            }

            if (mesh.changing() && correctPhi)
            {
                // Calculate absolute flux from the mapped surface velocity
                phi = mesh.Sf() & Uf;

                #include "correctPhi.H"

                // Make the flux relative to the mesh motion
                fvc::makeRelative(phi, U);

                mixture.correct();
            }

            if (mesh.changing() && checkMeshCourantNo)
            {
                #include "meshCourantNo.H"
            }
```

```
        }

        #include "alphaControls.H"
        #include "alphaEqnSubCycle.H"

        relaxing.correct();

        mixture.correct();

        #include "UEqn.H"

        // --- Pressure corrector loop
        while (pimple.correct())
        {
            #include "pEqn.H"
        }

        if (pimple.turbCorr())
        {
            turbulence->correct();
        }
    }

    runTime.write();

    Info<< "ExecutionTime = " << runTime.elapsedCpuTime() << " s"
        << "  ClockTime = " << runTime.elapsedClockTime() << " s"
        << nl << endl;
    }

    Info<< "End\n" << endl;

    return 0;
}


// ************************************************************************* //
```